Constraints on mantle melting from major and trace element systematics in residual abyssal peridotites

Dissertation
zur Erlangung des Grades
"Doktor der Naturwissenschaften"
am Fachbereich Geowissenschaften
der Johannes Gutenberg-Universität in Mainz

Eric Hellebrand

Tag der mündlichen Prüfung: 08.05.2001

Zusammenfassung für Fachfremde

Die Bildung von mittelozeanischen Rückenbasalten ist einer der wichtigsten Stoffflüsse der Erde. Jährlich wird entlang der 75.000 Kilometer langen mittelozeanischen Rücken mehr als 20 km^3 neue magmatische Kruste gebildet, das entspricht etwa 90 Prozent der globalen Magmenproduktion. Obwohl ozeanische Rücken und mittelozeanische Rückenbasalte zu den am meisten untersuchten geologischen Themenbereichen gehören, existieren weiterhin einige Streitfragen. Zu den wichtigsten zählen der absolute Aufschmelzgrad des Mantels und die Faktoren, die diesen bestimmen. Man kann die Schmelzbildung unter mittelozeanischen Rücken am besten mit einem Schwamm vergleichen, aus dem beim langsamen Aufsteigen das Wasser herausgepresst wird analog zu dem am Ozeanboden ausfließenden Basalt. Unter der 6 bis 7 Kilometer dicken basaltischen Kruste bleibt der trockene Schwamm in Form von Harzburgit (ein magnesium-reiches Gestein, zum ersten mal im 19. Jahrhundert in Bad Harzburg beschrieben) im obersten Erdmantel zurück. Bei der Aufschmelzung werden Hauptbestandteile wie etwa Aluminium, und inkompatible Spurenelemente (das heisst, sie werden bevorzugt von der Schmelze aufgenommen) aus dem Harzburgit entfernt. An bestimmten Stellen in der ozeanischen Kruste konnten in den letzten Jahrzehnten diese Mantelgesteinen untersucht und damit zusätzliche Information zur Bildung von mittelozeanischen Rückenbasalten gewonnen werden. Bisher zeigten Vergleichsstudien, dass der Aufschmelzgrad (Trockenheit des ausgepressten Schwammes) nicht überall gleich ist, sondern in Abhängigkeit von der Manteltemperatur, der Geschwindigkeit, mit der sich die tektonischen Platten auseinander bewegen, und weiteren Faktoren variiert. Die Elektronenstrahlmikrosonde liefert die Hauptelementzusammensetzung der vorhandenen Mantelrelikte, vor allem das meerwasserresistente Mineral Spinell, dessen Verhältnis von Chrom (Cr) zu Aluminium (Al), Cr/(Cr+Al), die so genannte Cr-Zahl im Allgemeinen als guter qualitativer Indikator für den Aufschmelzgrad betrachtet wird. Die Konzentrationen bestimmter Spurenelemente werden mit der weniger verbreiteten Ionensonde – einem zeitaufwendigen Verfahren – bestimmt. Die entscheidende Hürde zum quantitativen Verständnis von Aufschmelzprozessen unter mittelozeanischen Rücken war aber bisher, dass die zwei vorhandenen Methoden zur Bestimmung des Aufschmelzungsgrades nicht mit einander im Einklang zu bringen waren, ein Grund, weshalb diese Gesteine bisher relativ selten untersucht wurden.

Im Rahmen dieser Doktorarbeit wurden Tiefseeperidotite des Indischen Ozeans untersucht und es wurde festgestellt, dass die fehlende Korrelation zwischen Haupt- und Spurenelementen in residuellen Tiefseeperidotiten zum Teil auf einem Irrtum beruht. Die untersuchten Proben und aus der Literatur bekannten Daten anderer Peridotite zeigen, dass bestimmte Spurenelemente, wie die schweren Seltenerdelemente, sehr gut mit der Cr-Zahl der koexistierenden Spinelle korrelieren. Spurenelemente wie die leichten Seltenerdelemente hingegen korrelieren überhaupt nicht mit der Spinellzusammensetzung und sind also tatsächlich vom Hauptelementverhalten entkoppelt. Die Auswertung der guten Korrelation zwischen schweren Seltenerdelementen und Cr-Zahl im Spinell ergibt einen quantitativen Aufschmelzindikator für Residuen, welcher auf dem Spinellchemismus basiert. Damit kann der Schmelzgrad als Funktion der vergleichsweise einfach messbaren Cr-Zahl im Spinell ausgedrückt und die oben erwähnten geodynamischen Fragestellungen aus einer neuen Perspektive betrachtet werden. Zukünftig könnten somit heiße und kalte Flecken im Erdmantel unter den mittelozeanischen Rücken sowie deren zeitlichen Entwicklung auskartiert werden.

Abstract

The generation of mid-ocean ridge basalts (MORB) is one of the most important mass transfer processes on Earth. Each year, more than twenty km^3 of magmatic crust is produced along 75,000 km of ocean ridge, which is over ninety percent of the global magma production. Although ocean ridges and MORB are among the most studied geological features, several interlocking issues concerning melt generation at mid-ocean ridges are still not well understood. The most important of these are the role of geodynamic boundary conditions, such as spreading rate or vicinity to plumes and large transform offsets, as well as the absolute extent of melting or the depth at which melting initiates. This thesis examines these issues on the basis of mineral major and trace element compositions of oceanic mantle rocks.

Geochemical characteristics of MORB suggest that melting begins in the stability field of garnet peridotite, at depths exceeding 80 km. Recent experiments, however, have shown that heavy rare earth elements (REE) are compatible in clinopyroxene (cpx) at the lherzolite solidus. This garnet-like partitioning behavior of cpx implies that garnet is no longer needed and that melting begins at significantly lower pressures. Therefore it is important to know, whether this hypothesis is consistent with compositional variations of abyssal peridotites. These fragments of the oceanic mantle are the residues of MORB melting and are now exposed on the ocean floor. Their mineral chemistry preserved the conditions at which melts were created in the mantle. Major and trace element data obtained by electron and ion microprobe on residual abyssal peridotite samples from the Central Indian Ridge (CIR) are compared to published data. Cpx in the CIR peridotites have very fractionated REE patterns, i.e. low Sm/Yb ratios, but high absolute Yb concentrations. Fractional melting models (which simulate the most extreme fractionation theoretically possible) of a spinel peridotite using commonly accepted partition coefficients cannot reproduce the observed characteristics of the CIR peridotites. Application of the new partition coefficients, in which the heavy REE are compatible in cpx, may explain the measured data better than the models that use standard partition coefficients. Still, the observed fractionations require extremely high degrees of melting, inconsistent with the only moderate degrees of melting estimated from major elements. Small (~3-5%) degrees of melting of a garnet peridotite, followed by subsequent melting under spinel-facies

conditions can account for the observations. Therefore, garnet remains an important phase during partial melting beneath mid-ocean ridges (*Chapter 1*).

A further stumbling block for the quantitative understanding of melting beneath mid-ocean ridges has been the lack of correlation between major and trace elements in residual abyssal peridotites. The Cr/(Cr+Al) ratio (Cr#) of spinel is accepted as a good qualitative indicator for the extent of partial melting. In fact, heavy REE (Dy, Er, and Yb) in cpx are highly correlated (r^2 ~ 0.9) with Cr# of coexisting spinels using the CIR mineral data and published data from other abyssal peridotites. Application of this correlation yields a quantitative melting indicator for melting residues that is based on spinel major element compositions. Now, the absolute degree of melting can be expressed as a function of spinel Cr#: $F = 0.10 \cdot \ln(Cr\#) + 0.24$ (*Hellebrand et al., Nature, in review; Chapter 2*).

Application of this tool to melting residues for which ion probe data are not available enables us to link geochemical and geophysical data on melting beneath mid-ocean ridges. From a geodynamic perspective, Gakkel Ridge in the Arctic Ocean is important for the understanding of partial melting process, because it is the slowest spreading mid-ocean ridge on Earth and it is devoid of large-offset transform faults. Published basalt data imply an extremely low degree of melting, in accordance with global correlations between basalt composition and estimated degree of melting. Pervasively altered mantle peridotites from one location along the virtually unexplored Gakkel Ridge were studied for relict primary minerals. Only one sample contained oxidized spinel pseudomorphs in which traces primary spinel are still preserved. Their composition reflect a higher degree of melting than indicated by the basalt compositions and their Cr# are significantly higher than in peridotites from faster spreading ridges. Crustal thickness at Gakkel Ridge, calculated from this spinel composition, is thicker than the observed crustal thickness estimated from gravity data, or predicted from global correlations between spreading rate and seismically determined crustal thickness. This unexpected result may be due to enhanced compositional heterogeneity at low degrees of melting, or may reflect a higher overall degree of depletion for the Gakkel Ridge than was previously thought (*Hellebrand et al., Chem.Geol., in review; Chapter 3*).

Additional material is provided in *Appendices A-C*, which contain details relevant to the analysis and modeling presented in *Chapters 1-3*.

Zusammenfassung

Die Bildung von mittelozeanischen Rückenbasalten (MORB) ist einer der wichtigsten Stoffflüsse der Erde. Jährlich wird entlang der 75.000 km langen mittelozeanischen Rücken mehr als 20 km^3 neue magmatische Kruste gebildet, das sind etwa 90 Prozent der globalen Magmenproduktion. Obwohl ozeanische Rücken und MORB zu den am meisten untersuchten geologischen Themenbereichen gehören, existieren weiterhin einige Streitfragen. Zu den wichtigsten zählt die Rolle von geodynamischen Rahmenbedingungen, wie etwa Divergenzrate oder die Nähe zu Hotspots oder Transformstörungen, sowie der absolute Aufschmelzgrad, oder die Tiefe, in der die Aufschmelzung unter den Rücken beginnt. Diese Dissertation widmet sich diesen Themen auf der Basis von Haupt- und Spurenelementzusammensetzungen in Mineralen ozeanischer Mantelgesteine.

Geochemische Charakteristika von MORB deuten darauf hin, dass der ozeanische Mantel im Stabilitätsfeld von Granatperidotit zu schmelzen beginnt. Neuere Experimente zeigen jedoch, dass die schweren Seltenerdelemente (SEE) kompatibel im Klinopyroxen (Cpx) sind. Aufgrund dieser granatähnlichen Eigenschaft von Cpx wird Granat nicht mehr zur Erklärung der MORB Daten benötigt, wodurch sich der Beginn der Aufschmelzung zu geringeren Drucken verschiebt. Aus diesem Grund ist es wichtig zu überprüfen, ob diese Hypothese mit Daten von abyssalen Peridotiten in Einklang zu bringen ist. Diese am Ozeanboden aufgeschlossenen Mantelfragmente stellen die Residuen des Aufschmelzprozesses dar, und ihr Mineralchemismus enthält Information über die Bildungsbedingungen der Magmen. Haupt- und Spurenelementzusammensetzungen von Peridotitproben des Zentralindischen Rückens (CIR) wurden mit Mikrosonde und Ionensonde bestimmt, und mit veröffentlichten Daten verglichen. Cpx der CIR Peridotite weisen niedrige Verhältnisse von mittleren zu schweren SEE und hohe absolute Konzentrationen der schweren SEE auf. Aufschmelzmodelle eines Spinellperidotits unter Anwendung von üblichen, inkompatiblen Verteilungskoeffizienten (Kd's) können die gemessenen Fraktionierungen von mittleren zu schweren SEE nicht reproduzieren. Die Anwendung der neuen Kd's, die kompatibles Verhalten der schweren SEE im Cpx vorhersagen, ergibt zwar bessere Resultate, kann jedoch nicht die am stärksten fraktionierten Proben erklären. Darüber hinaus werden sehr hohe Aufschmelzgrade benötigt, was nicht mit Hauptelementdaten in Einklang zu bringen ist. Niedrige (~3-5%) Aufschmelzgrade im Stabilitätsfeld von Granatperidotit, gefolgt von weiterer Aufschmelzung von Spinellperidotit

kann jedoch die Beobachtungen weitgehend erklären. Aus diesem Grund muss Granat weiterhin als wichtige Phase bei der Genese von MORB betrachtet werden (*Kapitel 1*).

Eine weitere Hürde zum quantitativen Verständnis von Aufschmelzprozessen unter mittelozeanischen Rücken ist die fehlende Korrelation zwischen Haupt- und Spurenelementen in residuellen abyssalen Peridotiten. Das Cr/(Cr+Al) Verhältnis (Cr#) in Spinell wird im Allgemeinen als guter qualitativer Indikator für den Aufschmelzgrad betrachtet. Die Mineralchemie der CIR Peridotite und publizierte Daten von anderen abyssalen Peridotiten zeigen, dass die schweren SEE sehr gut (r^2 ~ 0.9) mit Cr# der koexistierenden Spinelle korreliert. Die Auswertung dieser Korrelation ergibt einen quantitativen Aufschmelzindikator für Residuen, welcher auf dem Spinellchemismus basiert. Damit kann der Schmelzgrad als Funktion von Cr# in Spinell ausgedrückt werden: $F = 0.10 \cdot \ln(Cr\#) + 0.24$ (*Hellebrand et al., Nature, in review; Kapitel 2*).

Die Anwendung dieses Indikators auf Mantelproben, für die keine Ionensondendaten verfügbar sind, ermöglicht es, geochemische und geophysikalischen Daten zu verbinden. Aus geodynamischer Perspektive ist der Gakkel Rücken im Arktischen Ozean von großer Bedeutung für das Verständnis von Aufschmelzprozessen, da er weltweit die niedrigste Divergenzrate aufweist und große Transformstörungen fehlen. Publizierte Basaltdaten deuten auf einen extrem niedrigen Aufschmelzgrad hin, was mit globalen Korrelationen im Einklang steht. Stark alterierte Mantelperidotite einer Lokalität entlang des kaum beprobten Gakkel Rückens wurden deshalb auf Primärminerale untersucht. Nur in einer Probe sind oxidierte Spinellpseudomorphosen mit Spuren primärer Spinelle erhalten geblieben. Ihre Cr# ist signifikant höher als die einiger Peridotite von schneller divergierenden Rücken und ihr Schmelzgrad ist damit höher als aufgrund der Basaltzusammensetzungen vermutet. Der unter Anwendung des oben erwähnten Indikators ermittelte Schmelzgrad ermöglicht die Berechnung der Krustenmächtigkeit am Gakkel Rücken. Diese ist wesentlich größer als die aus Schweredaten ermittelte Mächtigkeit, oder die aus der globalen Korrelation zwischen Divergenzrate und mittels Seismik erhaltene Krustendicke. Dieses unerwartete Ergebnis kann möglicherweise auf kompositionelle Heterogenitäten bei niedrigen Schmelzgraden, oder auf eine insgesamt größere Verarmung des Mantels unter dem Gakkel Rücken zurückgeführt werden (*Hellebrand et al., Chem.Geol., in review; Kapitel 3*).

Zusätzliche Informationen zur Modellierung und Analytik sind im *Anhang A-C* aufgeführt.

Chapter 1: Introduction

1.1. Aim

It has been understood for many years that decompression of the upwelling mantle beneath mid-ocean ridges causes the peridotitic material to melt. The melt is segregated from the mantle and accumulates, mixes and fractionates in magma chambers in the lower crust and eventually erupts on the ocean floor as mid-ocean ridge basalt (MORB). Below the crust, which has an average thickness of 6-7 km, the uppermost mantle contains the residues of this melt extraction process. Melting removes major basaltic constituents such as aluminum and calcium from the peridotitic residues. The chemical composition of these residues is thus a measure of depletion with respect to the composition of the source material before the onset of melting and therefore a complementary source of information to study melting processes in the oceanic mantle. The aim of this study is to use mineral compositions of a suite of residual abyssal peridotites from the Central Indian Ridge to assess the systematic behavior of major and trace elements during partial melting from the perspective of the melting residues and use this knowledge to improve the general understanding of melt extraction beneath mid-ocean ridges.

1.2. Melting beneath mid-ocean ridges

An adiabatically ascending parcel of mantle will begin to melt when the adiabat intersects the peridotite solidus, which has a steeper dT/dP slope (Fig. 1) (e.g. SCHILLING, 1973; LANGMUIR ET AL., 1992). The slope of the melting path is steeper than the slope of the solid adiabat, because there is a temperature drop associated with the heat of fusion. The pressure at which melting begins depends on the temperature of the mantle. A hot mantle will intersect its solidus at greater depths than a cool mantle. Therefore, the melting interval and the total extent of melting is larger when a hot mantle ascends underneath a ridge. If extraction is complete, the crustal thickness represents the total amount of melt produced. Using regionally average MORB compositions and crystal fractionation corrections, good global correlations between sodium content and ridge depth were observed (KLEIN and LANGMUIR, 1987). The fractionation-corrected sodium concentration in

MORB is a good indicator for the extent of melting. High sodium concentrations correspond to deep ridge depth and low extents of melting, low sodium values to shallow ridge depth and high extents of melting. Iron shows the opposite behavior and is believed to be sensitive to pressure during melting. High fractionation-corrected iron contents indicate a high mean pressure of formation. This suggests that melts, which preserve such a signature were rapidly transported to the surface without substantial reequilibration at low pressure. This excludes slow porous flow transport along grain boundaries and supports rapid channelized flow (LANGMUIR ET AL., 1992). Excess ^{230}Th preserved in many axial MORB glasses supports this hypothesis and places further constraints on the melting conditions. The fractionation between the highly incompatible trace elements Th and U must occur in the initial stages of melting. This implies that small melt increments are continuously removed and chemically isolated from the residual peridotite, i.e. melting is (near-) fractional. Furthermore, garnet must be present, because it is the only phase in which U is slightly more compatible than Th. And, given that the half life of ^{230}Th is 75 kyr, the melt must be rapidly transported to the surface in melt channels. (BEATTIE, 1993a; BEATTIE, 1993b; BOURDON ET AL., 1996; LUNDSTROM ET AL., 1995).

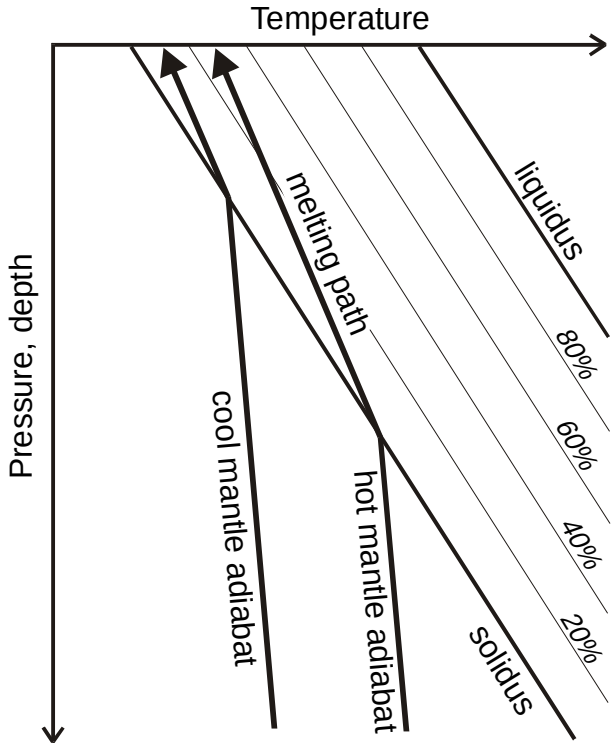

Fig. 1: Schematic pressure vs. temperature diagram showing melting paths for two adiabatically upwelling parcels of mantle material with different mantle temperatures.

Abyssal peridotites represent an additional source of information that is complementary to MORB. The number of scientists that investigate abyssal peridotites at present or have studied in the past is surprisingly small, compared to the large scientific community that has been working on MORB. The obvious reasons one might think of are probably the relative scarcity of abyssal peridotite exposures on the ocean floor with respect to MORB, and the altered appearance of the former mantle rocks, which makes them unsuitable for geochemical studies. I mention this, because I suspect that these reasons are, at least partly, based on misconceptions and prejudice. Abyssal peridotites are not rare, and neither is all primary information lost by the intense alteration. It solely requires careful (and therefore time-consuming) analytical procedures.

Exposures of serpentinized peridotites on the ocean floor are not restricted to large fracture zones, but they do occur in axial regions and non-transform offsets of mid-ocean ridges, predominantly at slow spreading rates (e.g. CANNAT, 1993). There are estimates that up to 20% of the ocean floor along the slow-spreading (~2 cm/yr full rate) Mid-Atlantic Ridge consists of serpentinites (CANNAT ET AL., 1995). Recent gravity data from the extremely slow-spreading (<1 cm/yr) Gakkel Ridge in the Arctic Ocean suggest that even more serpentinized mantle is exposed (COAKLEY and COCHRAN, 1998). The crustal structure in such regions is much more complex than predicted from the canonical four-layer ophiolite pseudostratigraphy defined at the Penrose Conference in the early seventies. At very slow spreading ridges, focussed flow of upwelling mantle material leads to magmatic segmentation that is both temporally and spatially variable. In time, segments can grow in their axial length at the expense of neighbouring segments. Spatially, lithological and structural variations can be large. In the center of such a magmatic cell, the crustal thickness is normal with a basaltic ocean floor at relatively shallow water depths. The boundaries of magmatic cells, on the other hand, are magma-starved domains. Here, exposures of plutonic and mantle lithologies are common on the –generally deeper– ocean floor (CANNAT ET AL., 1995).

Modal compositions of residual abyssal peridotites from all ocean basins have been determined by point-counting of large thin sections. As shown in Fig. 2, partial melting of an orthopyroxene- (opx) and clinopyroxene- (cpx) rich source systematically changes to virtually cpx-free, opx-poor harzburgitic residue (DICK ET AL., 1984). In contrast to fresh basalt glasses, whole rock compositions of abyssal peridotites do not directly reflect their magmatic nature. They are a mixture of the depleted peridotite residue and the chemical

compounds that were introduced by the reaction with seawater –mainly water and alkali elements. Therefore, only relict minerals, which are commonly preserved in the altered matrix of the rock, contain the primary mantle signature. Consequently, the analytical techniques for obtaining the desired information are microbeam tools, such as electron probe microanalysis (EPMA, electron microprobe) for analyses of the major and some minor elements, and secondary ion mass spectrometry (SIMS, ion probe) to obtain concentrations of selected trace elements.

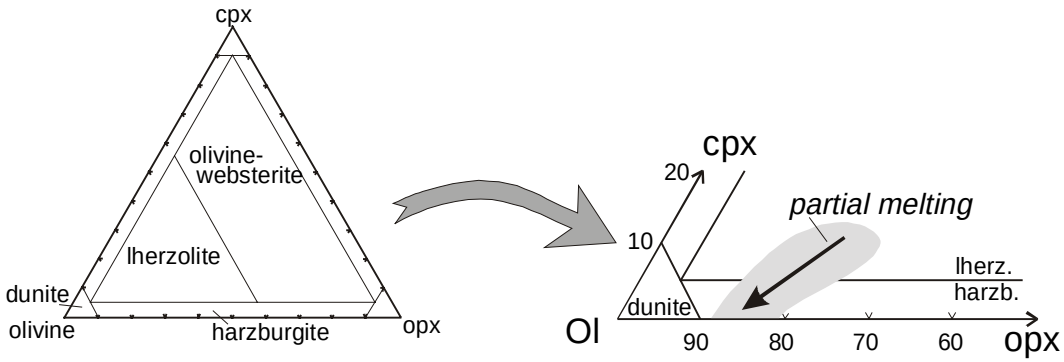

Fig. 2: Modal ternary diagram: clinopyroxene-olivine-orthopyroxene with the composition of abyssal peridotites (grey field) after DICK ET AL. (1984)

Regional and global studies of compositional variations of relict minerals in abyssal peridotites have found following chemical parameters correlate with degree of melting: Cr-number (= molar Cr/(Cr+Al)) in spinel increases, Al in orthopyroxene and clinopyroxene decrease, Mg-number (= molar Mg/(Mg+Fe)) in olivine, orthopyroxene and clinopyroxene increase slightly, and despite large scatter, titanium and sodium concentrations in clinopyroxene decrease with increasing (estimated) degree of melting (DICK and BULLEN, 1984; MICHAEL and BONATTI, 1985; DICK, 1989). This estimated degree of melting correlates with spreading rate, if regional averages are considered (NIU and HEKINIAN, 1997). However, the current knowledge of abyssal peridotite is strongly biased towards slow spreading ridges. Particularly the very slow spreading Southwest Indian Ridge and the northern part of the slow spreading Mid-Atlantic Ridge are relatively well studied. From the fast spreading East Pacific Rise only three occurrences of outcropping mantle rocks are known. Estimates on a spreading rate dependence of the degree of melting therefore hinge on these particular samples (NIU and HEKINIAN, 1997).

Less than a handful of ion probe studies on residual abyssal peridotites exist in the literature. The work of JOHNSON ET AL. (1990) was the first of its kind and the most

important, because the authors have shown that incompatible trace element concentrations in clinopyroxene of these melting residues vary in several orders of magnitude. Assuming that these rocks were derived by melt extraction from a similar source material ('Depleted Mantle Reservoir'), variable degrees of near-fractional melting must have produced these residual compositions, meaning that the generated melt is immediately seperated from its residue. The following regional and local studies confirmed this (JOHNSON and DICK, 1992; DICK and NATLAND, 1996; ROSS and ELTHON, 1997), but practically nothing new was added. This is surprising, because several issues were not addressed sufficiently. This includes the role of garnet during melting, the extent and effects of melt entrapment on the trace element signature in the final stages of melting, the extent, scales and causes of local chemical heterogeneities, and several other interlocking aspects. These are all integrated in this study and summarized below.

1.3. Summary of the chapters

Chapter 1 is by far the longest of the three chapters in this thesis and contains detailed petrographic and mineral compositional information on residual abyssal peridotites from the Central Indian Ridge. The mineral chemistry of these samples is used to discuss whether residual garnet is involved in the melting process beneath mid-ocean ridges. The issue of melting in the presence of garnet is intensely debated at present and this chapter approaches this subject from the perspective of the residues of melting. This discussion is largely based on modeling of several aspects of MORB geochemistry. All of these models incorporate constant partition coefficients between melt and solid peridotite. Recent experiments, however, have shown that these partition coefficients can be highly variable as a function of pressure, temperature and composition of the peridotite, and garnet is no longer needed as a residual phase to explain the MORB compositions (BLUNDY ET AL., 1998). That means that the onset of melting beneath mid-ocean ridges is shifted towards significantly lower pressures. Both the application of 'normal' constant and 'new' variable partition coefficients cannot explain the low middle to heavy earth element ratios measured in clinopyroxenes of the Central Indian Ridge peridotites. Small amounts (1-5%) of melt extraction of a garnet peridotite, prior to ascent, reequilibration and subsequent melting in the stability field of spinel peridotite can explain these features. Roughly half of the peridotite residues from the Central Indian Ridge contain this 'ghost garnet' signature. Furthermore, slight enrichments in the light rare earth elements observed in many clinopyroxenes indicate incomplete melt extraction or refertilization with an infiltrating melt.

This is in accordance with petrographic observations of modally very depleted harzburgites, in which very few clinopyroxenes only occur as small interstitial films on olivine-olivine grain boundaries. However, such a late-stage process may obscure the chemical signature imposed by partial melting in the presence of garnet. This chapter is submitted to the *Journal of Petrology* with the following author list: Eric Hellebrand, Jonathan Snow, and Albrecht Hofmann.

Chapter 2 is very short and condensed. There is a common belief that major and trace elements in melting residues (abyssal peridotites and ophiolite mantle rocks) are 'decoupled'. This means that trace elements do not follow the behavior of qualitative major element indicators of melting, such as Cr/(Cr+Al) ratio (= Cr-number) in spinel, aluminum content of pyroxene, or Mg/(Mg+Fe) ratio in silicates. Here I present that moderately incompatible trace elements (Dy, Er, Yb) in cpx are in fact highly correlated with spinel Cr-number. The actual 'decoupling' is confined to the highly incompatible trace elements, such as La, Ce, Nd, Sr, and Zr. Considering that quantitative melting models can be derived from cpx trace element compositions (as shown in *Chapter 1*) the excellent correlation between the heavy rare earth elements and the spinel Cr-number can be used to express the degree of melting as a function of the spinel Cr-number. This manuscript has been submitted to *Nature* for publication and is currently in review. Co-authors: Jonathan Snow, Henry Dick (Woods Hole Oceanographic Institution, USA) and Albrecht Hofmann.

In *Chapter 3* the spinel composition of one single abyssal peridotite sample is discussed. The important aspect of this sample is that it represents the first and currently only direct information from the mantle beneath the extremely slow-spreading Gakkel Ridge in the Arctic Ocean. Gakkel Ridge is the northernmost continuation of the Mid-Atlantic Ridge, and the study of this ridge is of crucial importance to global geodynamics. Abyssal peridotite major element compositions predict a spreading rate dependence of the degree of melting (NIU and HEKINIAN, 1997). The slowest-spreading ridge on Earth, the Gakkel Ridge, is therefore expected to reflect the lowest overall degrees of melting. Two basaltic samples, the only recovered so far, confirm this global correlation. However, the spinel Cr-number of this particular Arctic abyssal peridotite sample is significantly higher than expected based on the global correlation. This does not agree with geodynamic inferences based on basalt composition. In Chapter 3, the possible causes and geodynamic

implications are discussed. This manuscript is submitted to *Chemical Geology* for publication. Co-authors: Jonathan Snow and Richard Mühe (Universität Kiel).

1.4. Possible future studies

Below I will briefly summarize what potential information can be extracted by further study of abyssal peridotites.

(1) One of the most well-known facts in geochemistry is that the mantle is chemically heterogeneous, that is, *before* the onset of melting. The scales of chemical heterogeneity are unknown and estimates are based on theoretical considerations and observations of 'mafic layers' intercalated in peridotite in orogenic lherzolite bodies on land. So far, there hasn't been any direct physical evidence for the presence of unmolten 'mafic layers' on the ocean floor that might confirm the 'marble cake' mantle hypothesis. Presumably, this material has been completely molten during the first few percents of melting. Unmolten mafic relics might be preserved at a mid-ocean ridge with very low degrees of melting. Independent of whether this recycled material is found or not, the mantle rocks that are brought up at such a location probably give the best approximation of the hypothetical Depleted Mantle (DM) reservoir. At Gakkel Ridge in the Arctic Ocean, the exposure of large amounts of very fertile mantle rocks is very likely, because it is the slowest spreading ridge on Earth. A petrological sampling cruise that is scheduled for summer 2001 may help resolve this issue.

(2) Directly related to the previous point are the scales and extents of geochemical heterogeneity *as a result* of partial melting and melt migration beneath mid-ocean ridges. Geochemical, petrological and structural studies in the mantle sections of several ophiolites have revealed small-scale (~cm-m) modal and compositional heterogeneities. A melt that is generated at depth will not be in equilibrium with the surrounding mantle at the base of the crust, provided that its ascent was rapid and chemically isolated. Melt focussing and accumulation from a broad region at depth to the narrow neovolcanic zone inevitably leads to reactive melt percolation (KELEMEN ET AL., 1997; SUHR, 1999). Pyroxene dissolution and olivine precipitation lead to the formation of dunitic channels. Such channels are well studied in ophiolites but little is known as to whether these observations can be extrapolated to the oceanic upper mantle. Currently, spatial resolution between individual ocean floor samples is poor.

Sampling occurs either on km-scale between individual dredge hauls, or, on cm-scale within a single sample. Chemical and modal heterogeneities on 'dredge scale' occur, but vary a lot. Mantle holes drilled during the Ocean Drilling Program show striking homogeneity across several hundreds of meters. Important progress can only be made if an area with high modal and chemical variation, as known from dredging, is sampled by drilling.

(3) Chemical exchange between the peridotitic part of the crust and the overlying seawater column. Considering that the fraction of serpentinized peridotite in the oceanic crust at slow spreading ridges may range up to 20% (or maybe even more), it is important to know how peridotites and serpentinites behave during alteration. SNOW and DICK (1995) have shown that pervasive peridotite weathering on the seafloor at cold seawater temperatures lead to loss of magnesium and nickel on the order of twenty percent. It would be important to assess the alteration behavior of these elements and other mantle compatible elements more precisely in order to estimate the contribution of the peridotitic part of the crust to the overlying seawater column.

1.5. References

Beattie P. (1993a) The generation of uranium series disequilibria by partial melting of spinel peridotite; constraints from partitioning studies. *Earth Planet. Sci. Lett.* **117**, 379-391.

Beattie P. (1993b) Uranium-thorium disequilibria and partitioning on melting of garnet peridotite. *Nature* **363**, 63-65.

Blundy J., Robinson J. A. C., and Wood B. (1998) Heavy REE are compatible in clinopyroxene on the spinel lherzolite solidus. *Earth Planet. Sci. Lett.* **160**, 493-504.

Bourdon B., Langmuir C. H., Elliot T., and Zindler A. (1996) Constraints on mantle melting at mid-ocean ridges from global ^{238}U-^{230}Th disequilibrium data. *Nature* **384**, 231-235.

Cannat M. (1993) Emplacement of mantle rocks in the seafloor at mid-ocean ridges. *J. Geophys. Res.* **98**, 4163-4172.

Cannat M., Mevel C., Maia M., Deplus C., Durand C., Gente P., Agrinier P., Belarouchi A., Dubuisson G., Humler E., and Reynolds J. (1995) Thin crust, ultramafic exposures, and rugged faulting patterns at the Mid-Atlantic Ridge (22 degrees -24 degrees N). *Geology* **23**(1), 49-52.

Coakley B. J. and Cochran J. R. (1998) Gravity evidence of very thin crust at the Gakkel Ridge (Arctic Ocean). *Earth Planet. Sci. Lett.* **162**, 81-95.

Dick H. J. B. (1989) Abyssal peridotites, very slow spreading ridges and ocean ridge magmatism. *Geol. Soc. Spec. Publ.* **42**, 71-105.

Dick H. J. B. and Bullen T. (1984) Chromian spinel as a petrogenetic indicator in abyssal and alpine-type peridotites and spatially associated lavas. *Contrib. Mineral. Petrol.* **86**, 54-76.

Dick H. J. B., Fisher R. L., and Bryan W. B. (1984) Mineralogic variability of the uppermost mantle along mid-ocean ridges. *Earth Planet . Sci. Letters* **69**, 88-106.

Dick H. J. B. and Natland J. H. (1996) Late-stage melt evolution and transport in the shallow mantle beneath the East Pacific Rise. *Proc. ODP, Sci. Res.* **147**, 103-134.

Johnson K. T. M. and Dick H. J. B. (1992) Open system melting and temporal and spatial variation of peridotite and basalt at the Atlantis II fracture zone. *J. Geophys. Res.* **97**, 9219-9241.

Johnson K. T. M., Dick H. J. B., and Shimizu N. (1990) Melting in the oceanic upper mantle; an ion microprobe study of diopsides in abyssal peridotites. *J. Geophys. Res.* **95**, 2661-2678.

Kelemen P. B., Hirth G., Shimizu N., Spiegelman M., and Dick H. J. B. (1997) A review of melt migration processes in the adiabatically upwelling mantle beneath oceanic spreading ridges. *Phil. Trans. R. Soc. London* **355**, 283-318.

Klein E. M. and Langmuir C. H. (1987) Global correlations of ocean ridge basalts with axial depth and crustal thickness. *J. Geophys. Res.* **92**, 8089-8115.

Langmuir C. H., Klein E. M., and Plank T. (1992) Petrologic systematics of mid-ocean ridge basalts: constraints on melt generation beneath ocean ridges. In *Mantle flow and melt generation at mid-ocean ridges*, Vol. 71 (ed. J. Phipps-Morgan, D. K. Blackman, and J. M. Sinton), pp. 183-280. AGU Monograph.

Lundstrom C. C., Gill J., Williams Q., and M. P. (1995) Mantle melting and basalt extraction by equilibrium porous flow. *Science* **270**, 1958-1961.

Michael P. J. and Bonatti E. (1985) Peridotite composition from the North Atlantic; regional and tectonic variations and implications for partial melting. *Earth Planet. Sci. Lett.* **73**, 91-104.

Niu Y. and Hekinian R. (1997) Spreading-rate dependence of the extent of mantle melting beneath ocean ridges. *Nature* **385**, 326-329.

Ross K. and Elthon D. (1997) Extreme incompatible trace-element depletion of diopside in residual mantle from south of the Kane F.Z. *Proc. ODP, Sci. Res.* **153**, 277-284.

Schilling J.-G. (1973) Iceland mantle plume: geochemical stuy of Reykjanes Ridge. *Nature* **242**, 565-571.

Snow J. E. and Dick H. J. B. (1995) Pervasive magnesium loss by marine weathering of peridotite. *Geochim. Cosmochi. Acta* **59**, 4219-4235.

Suhr G. (1999) Melt migration under oceanic ridges: inferences from reactive transport modelling of upper mantle hosted dunites. *J. Petrol.* **40**, 575-599.

Chapter 2: Garnet-field melting and late-stage refertilization in 'residual' abyssal peridotites from the Central Indian Ridge

Eric Hellebrand, Jonathan E. Snow and Albrecht W. Hofmann

Submitted to *Journal of Petrology*

Chapter 2: Garnet-field melting and late-stage refertilization in 'residual' abyssal peridotites from the Central Indian Ridge

Abstract – The role of residual garnet during melting beneath mid-ocean ridges has been the subject of many recent investigations. In order to address this issue from the perspective of the melting residues, we obtained major and trace element mineral chemistry of a suite of residual abyssal peridotites from the intermediate spreading Central Indian Ridge. Many clinopyroxenes have ratios of middle to heavy REE that are too low to be explained by melt extraction in the stability field of spinel peridotite alone. Several percent of melting must have occurred at higher pressures in the garnet peridotite stability field if pure fractional melting models are used. This value increases if the buffering effect of a residual melt porosity, or minor amounts of melt entrapment are considered. Application of new trace element partitioning models, which predict that heavy REE are compatible in high-pressure clinopyroxene, cannot fully explain the fractionation from of the middle from the heavy REE. Further, many samples show textural and chemical evidence for refertilization, such as relative enrichments of highly incompatible trace elements with respect to moderately incompatible trace elements. Therefore, highly incompatible elements, which are decoupled from major and moderately incompatible trace elements, are useful to assess late-stage processes, such as melt entrapment, melt-rock reaction and veining. Moderately incompatible trace elements are less affected by such late-stage processes and thus useful to infer the melting history of abyssal peridotites.

2.1. Introduction

Mid-ocean ridge basalts (MORB) are the products of partial melting of the upwelling mantle, and form the upper part of the oceanic crust (BOTTINGA and ALLÈGRE, 1978; GREEN and RINGWOOD, 1967; MCKENZIE, 1984). Petrological, geochemical and experimental evidence, as well as thermodynamic considerations suggest that this adiabatic decompression melting is a polybaric process (KLEIN and LANGMUIR, 1987; MCKENZIE and BICKLE, 1988; O'HARA, 1985). The depth at which melting initiates, however, is intensely debated (KLEIN and LANGMUIR, 1987; LANGMUIR ET AL., 1992; MCKENZIE and BICKLE, 1988; SHEN and FORSYTH, 1995), as this has direct implications for the temperature of the upwelling mantle and the thickness of the generated crust. Several geochemical characteristics of MORB are attributed to melting in the presence of residual garnet, suggesting that the onset of melting exceeds 80 km (GREEN and RINGWOOD, 1970; O'HARA ET AL., 1971; TAKAHASHI, 1986): (1) High middle to heavy rare earth element (REE) ratios in melt inclusions in magnesian olivines from Mid-Atlantic Ridge basalts (SOBOLEV, 1996). (2) Examination of combined Lu-Hf and Sm-Nd systematics revealed subchondritic Lu/Hf values in MORB, but a long-term Lu/Hf value that is higher than chondritic (SALTERS and HART, 1989; SALTERS, 1996). These authors explain this so-called Hf-paradox by a recent Lu-Hf fractionation of during MORB genesis in the presence of garnet . (3) The generation of excess ^{230}Th in axial MORB glasses from several locations along the mid-ocean ridge system requires garnet in the source (BEATTIE, 1993a; BEATTIE, 1993b; BOURDON ET AL., 1996; LUNDSTROM ET AL., 1995). Furthermore, melt extraction must be almost purely fractional to produce the observed U-series disequilibria, meaning that small melt increments are immediately separated from the residue. However, the melt formed cannot be perfectly extracted from the residue, a very small fraction will most likely be retained on grain boundaries or in interstices between minerals. This residual melt porosity has been estimated to be in the range of 0.1 – 1% (LANGMUIR ET AL., 1992; LUNDSTROM ET AL., 2000; SPIEGELMAN and ELLIOT, 1993).

Evidence for melting in the presence of garnet can also be derived from geochemical modeling of the mantle melting process. The inferences drawn from such melting models depend strongly on the trace element partition coefficients (Kd's) between the silicate melt and the coexisting mantle phases clinopyroxene (cpx) and garnet, which accommodate the bulk of the incompatible lithophile trace elements. For the REEs, cpx and garnet have

highly different partition coefficients. The partition coefficients between garnet and melt increase steadily from highly incompatible for the light REE (LREE) to moderately compatible for the heavy REE (HREE) (e.g. JOHNSON, 1998). In cpx, LREE are also highly incompatible, whereas middle (M) and HREE are moderately incompatible (HART and DUNN, 1993; JOHNSON, 1998). It is also well-known that trace element partition coefficients are not constant throughout the entire melting column, but vary with pressure, temperature and mineral composition (GAETANI and GROVE, 1995; WOOD and BLUNDY, 1997; BLUNDY ET AL., 1998; JOHNSON, 1998). Recent experiments and theoretical considerations revealed that HREE are moderately compatible in Na- and Al-rich cpx on the spinel lherzolite solidus (BLUNDY ET AL., 1998). According to this study, high-pressure cpx has partitioning characteristics that are more garnet-like than previously assumed. This would imply that involvement of garnet in MORB generation is no longer required. Documenting a garnet signature in MORB lavas conclusively is hindered by processes such as magmatic mixing, and polybaric melting.

Studying the residues of partial melting allows us to address this issue from a different, complementary perspective. Residual mantle peridotites are depleted in basaltic components, as a result of melt extraction (DICK ET AL., 1984; MICHAEL and BONATTI, 1985; DICK, 1989). Normally, the residual rocks from the uppermost mantle are inaccessible because of the overlying 6-7 km thick magmatic crust. At many locations along mid-ocean ridges, however, such mantle melting residues are tectonically exposed on the ocean floor (AUMENTO and LOUBAT, 1971; DICK ET AL., 1984; CANNAT, 1993). These so-called abyssal peridotites are commonly highly altered, but contain mineral relicts that preserve primary information about melting and melt extraction. At present, several melting models are used to explain the available abyssal peridotite data. Strong LREE depletions in residual cpx confirm that melt extraction beneath mid-ocean ridges is nearly fractional (JOHNSON ET AL., 1990; JOHNSON and DICK, 1992). Apparently, this disagrees with results from major element modeling using MELTS, which suggests that batch (high porosity) melting is required to explain the major element composition of abyssal peridotites (ASIMOW, 1999). However, batch melting has only a minor effect on the fractionation of incompatible trace elements in the residue, i.e. trace element ratios hardly vary as a function of melt fraction produced, in contrast to fractional melting. As an apparent compromise, recent considerations have shown that cpx REE patterns in abyssal peridotites are also consistent with near-fractional melting followed by batch melting or vice versa (KELEMEN ET AL., 1997; ASIMOW, 1999).

The abyssal peridotite database on which these interpretations are based is small, and restricted mainly to fracture zone peridotites from the very slow spreading Southwest Indian and American Antarctic Ridges (JOHNSON ET AL., 1990; JOHNSON and DICK, 1992) and two localities in the North Atlantic (ROSS and ELTHON, 1997) and Pacific oceans (DICK and NATLAND, 1996). To expand this database towards faster spreading ridges, we obtained major and trace element data by electron and ion microprobe analysis on fresh cpx grains of vein-free and plagioclase-free peridotites from the intermediate-spreading Central Indian Ridge (CIR).

2.2. Geological setting

The N-S trending Central Indian Ridge (CIR) is an intermediate-spreading mid-ocean ridge. Spreading rates, predicted by NUVEL 1 plate velocity model (DEMETS ET AL., 1990), vary from 30 mm/yr (full rate) near the equator to 49 mm/yr at the Rodrigues Triple Junction (RTJ). In contrast to the highly oblique-spreading Southwest Indian Ridge (SWIR), the CIR is characterized by a moderate but variable ridge obliquity (Fig. 1). Between the RTJ at 25°S and Argo Fracture Zone (FZ) at 13°S, spreading is nearly orthogonal (DYMENT, 1998). Very few large-offset fracture zones occur in this part of the CIR. The most prominent transform fault is the Marie Celeste FZ (MCFZ) at 17°S, offsetting the CIR by almost 300 km. North of Argo FZ, the CIR trends NNE and spreading is highly oblique (Fig. 1). Here, the CIR is dominated by smaller ridge segments, separated by numerous NE-SW trending small-offset transform faults. North of 5°S the CIR gradually returns to NNW-trending orthogonal spreading. The NW-trending Carlsberg Ridge is the northern continuation of the CIR and is devoid of fracture zones.

In contrast to most other mid-ocean ridges, few active hotspots have interacted with the ridge in recent times. Solely the Réunion hotspot, now located 1100 km west of the ridge axis, interacted with the CIR. Around magnetic anomaly 21 (47 Ma), the hotspot crossed the CIR from the Indian to the African plate (DYMENT, 1998). The track of the Réunion hotspot can be traced back to the Chagos-Lagadive Ridge on the Indian plate, and finally to India, where it initially produced the Deccan traps around 66 Ma ago (MAHONEY, 1988). Despite the large distance to the current Réunion hotspot, several indications suggest a cryptic ridge-hotspot interaction along the CIR near 18 – 20°S.

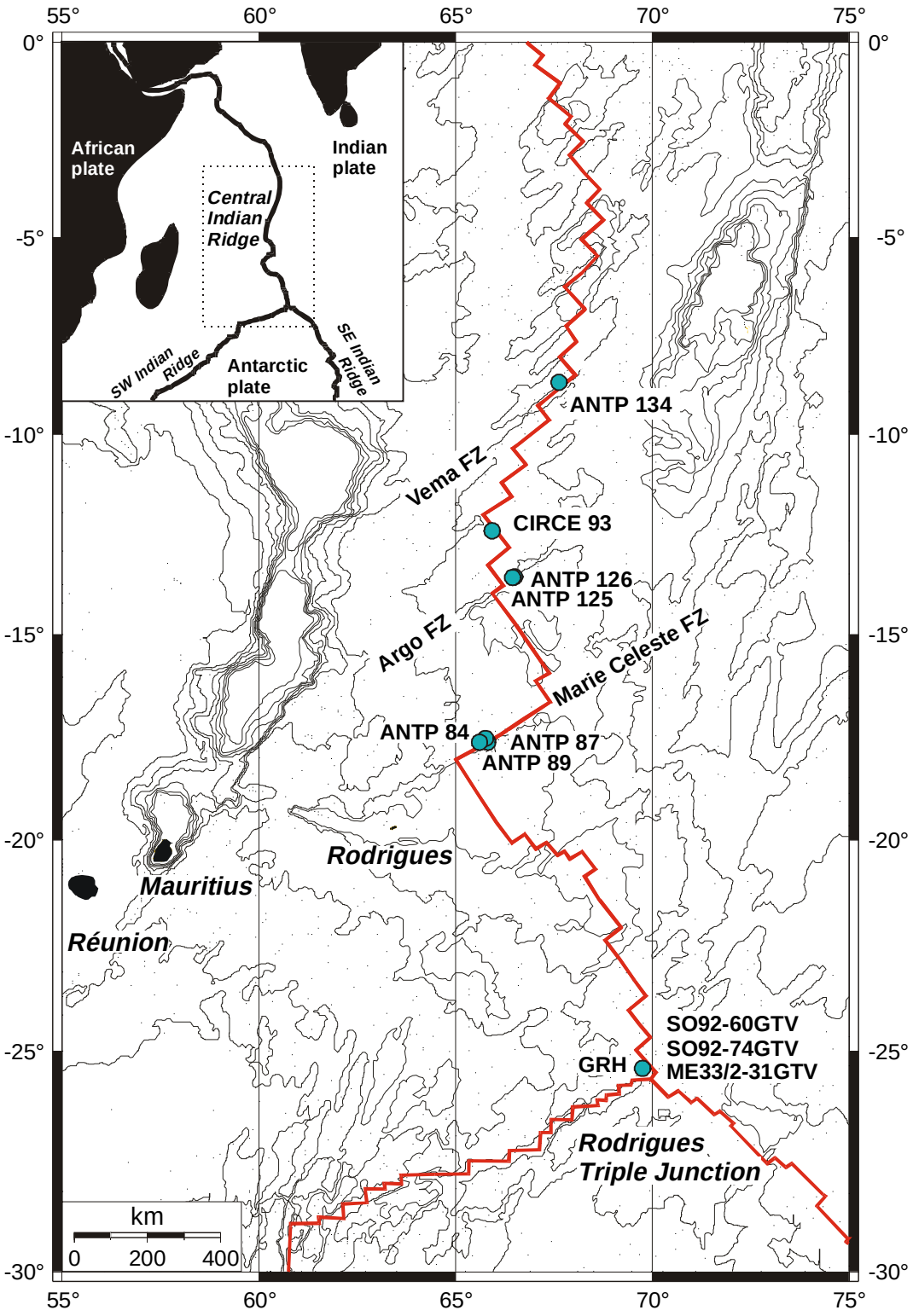

Fig. 1: Bathymetric map of the northwestern part of the Indian Ocean showing the Central Indian Ridge (CIR) and its major transform faults. Numbers refer to sampling locations listed in Table 1. GRH denotes Green Rock Hill.

A broad bathymetric anomaly is observed at the CIR, centered on 19°S, 66°E (BRIAIS, 1995) and the long-wavelength bathymetry varies towards the RTJ. The axial depth of the CIR increases gradually from an average of 3200 m at 20°S to 4000 m at the triple junction (BRIAIS, 1995). Further, a narrow E-W trending linear structure between Mauritius and the CIR, named Rodrigues Ridge, approaches the axis to 50 km. Volcanics from Rodrigues Island, the only subaerial expression of this obscure volcanic ridge, are compositionally very similar to Réunion and Mauritius Island (BAXTER ET AL., 1985) and have an age of 1.58-1.30 Ma (MCDOUGALL and CHAMALAUN, 1969). This excludes an origin at the ridge, but supports the hypothesis of MORGAN (1978), who suggested channelized asthenospheric flow from the Réunion hotspot towards the CIR to explain the Rodrigues volcanism. Apparently, the melting region beneath the MCFZ and the neighbouring CIR segments is tapping the same source, as reflected by the enriched MORB geochemistry (MAHONEY ET AL., 1989). A low velocity signature beneath the Reunion-Mauritius islands and the CIR could reflect a real connection between actual hotspot material and the CIR (DEBAYLE and LEVEQUE, 1997).

Isotopic and trace element data from basalts confirm a presently active ridge-hotspot interaction at the CIR, although the sampling density is poor compared to better-studied mid-ocean ridges such as the East Pacific Rise and the Mid-Atlantic Ridge. It is well known, however, that Indian Ocean MORBs differ in Sr-Nd-Pb isotopic composition from those of the Atlantic and Pacific Ocean (DUPRÉ and ALLÈGRE, 1983; REHKÄMPER and HOFMANN, 1997). Higher $^{208}Pb/^{204}Pb$ and $^{207}Pb/^{204}Pb$ values at a given $^{206}Pb/^{204}Pb$ value than beneath the Atlantic and Pacific have led to the concept that the sub-Indian Ocean mantle has been enriched by recycled sediments (REHKÄMPER and HOFMANN, 1997), or delaminated subcontinental lithosphere (SCHIANO ET AL., 1997). On a regional scale, the MCFZ and the adjacent ridge segment to the south are geochemically anomalous, which agrees with the anomalies seen in the bathymetry. MORB glasses with high $^{87}Sr/^{86}Sr$ values of 0.7030 – 0.7036 and $^{206}Pb/^{204}Pb$ values of 18.3 – 18.9 suggest that the MORB source region in this part of the CIR is influenced by an enriched component, despite the distance to the current or past locations of the Réunion hotspot (MAHONEY ET AL., 1989). $Na_{8.0}$, $Fe_{8.0}$ and incompatible trace element concentrations in MORB show large scatter for relatively primitive (Mg/(Mg+Fe) >0.55) Mg# (NATLAND, 1991, pers. comm.) suggesting significant heterogeneities in the mantle source beneath the ridge and the MCFZ. In other portions of the CIR, large local variations are absent. The southern part of the CIR appears to be chemically unaffected by the hotspot, and the $Na_{8.0}$ of the basalt also gradually

increase from 2.3 at 19°S to 3.0 at the RTJ. This is in accordance with the global correlation between ridge depth and basalt composition (KLEIN and LANGMUIR, 1987).

2.2.1. Samples and petrography

Forty abyssal peridotites from eleven stations along the Central Indian Ridge were studied by electron and ion microprobe. The sampling locations are shown in Figure 1. Most samples were collected during the Scripps Institution of Oceanography expeditions CIRCE and ANTIPODES at Argo, Marie Celeste, and Vema fracture zones and along the CIR axis at 12°S (ENGEL and FISHER, 1975). Recently, outcropping serpentinized peridotites were sampled by TV-grab at Green Rock Hill (GRH), located off-axis on the western flank of the southernmost CIR segment during cruises SO92 with RV Sonne in 1994 and ME33/2 with RV Meteor in 1995, yielding three well-positioned peridotite sample sets from one large peridotite exposure (Snow et al., in prep).

Residual peridotites were selected for analysis using the same criteria as JOHNSON ET AL. (1990), in order to allow direct comparison between the two data sets. From a total of 40 peridotite samples, 25 are texturallly residual. Fifteen non-residual samples were discarded for this study, because seven peridotites contained minor amounts of plagioclase, and eight were cut by thin (< 1 mm) magmatic veins. These non-residual peridotites will be discussed elsewhere. Modal compositions of all residual peridotite samples except the ones from GRH were determined by DICK ET AL. (1984) and DICK (unpubl. res.). They are spinel peridotites (62.6-90.4% olivine, 9.3-35.1% orthopyroxene (opx), 0-7% clinopyroxene (cpx), 0.04-0.9% spinel) (Table 1). With the exception of two lherzolitic samples from Argo FZ (ANTP126-2 and ANTP126-5) and one axial dunite from 12°S (CIRCE93-2), all studied peridotites are harzburgites. The local modal variability is large, especially for the sample set from the Marie Celeste Fracture Zone (MCFZ). Here, virtually cpx-free harzburgites were collected together with modally more fertile samples.

TABLE 1. Sampling locations and modal analyses of Central Indian Ridge peridotites

Sample	Position		Modes (vol.%)			
	Latitude	Longitude	ol	opx	cpx	sp
Vema FZ						
ANTP134-3	8°41.5'S	67°38.0'E	69.6	25.3	4.5	0.6
ANTP134-4			78.8	16.2	4.2	0.6
ANTP134-5			-	-	-	-
ANTP134-7			62.6	35.1	1.3	0.9
ANTP134-8			-	-	-	-
CIR axis 12°S						
Circe93-2	12°25.0'S	65°56.0'E	90.4	9.3	0.1	0.2
Circe93-3			78.5	21.2	0.0	0.3
Circe93-4			75.5	21.7	2.2	0.7
Circe93-5			77.6	22.1	0.0	0.3
Circe93-7			83.1	16.7	0.1	0.1
Argo FZ						
ANTP126-2	13°33.7'S	66°30.1'E	70.1	23.4	6.1	0.4
ANTP126-5			71.3	20.9	7.0	0.8
ANTP125-D5			74.6	20.8	3.7	0.9
Marie Celeste FZ						
ANTP84-11	17°39.2'S	65°36.6'E	76.7	19.5	3.7	0.1
ANTP87-5	17°35.8'S	65°45.2'E	80.8	17.9	1.0	0.3
ANTP87-9			82.7	17.1	0.04	0.14
ANTP89-1	17°38.1'S	65°49.0'E	71.3	27.8	0.4	0.4
ANTP89-2			76.1	21.2	2.2	0.3
ANTP89-5			73.1	21.5	4.9	0.5
ANTP89-8			75.8	19.9	3.8	0.3
ANTP89-15			85.1	14.4	0.5	0.04
ANTP89-17			81.0	16.9	1.9	0.1
Green Rock Hill						
ME33/2-31GTV	25°23.7'S	69°45.6'E	70.0	28.0	1.4	0.6
SO92-60GTV			74.0	22.8	2.6	0.6
SO92-74GTV			74.0	23.5	1.9	0.6

Texturally, the residual CIR peridotites vary between coarse equigranular and porphyroclastic, which is typical for most mantle rocks (e.g. MERCIER and NICOLAS, 1975). Overall, the CIR peridotites are not strongly deformed, as indicated by aspect ratios of opx porphyroclasts that rarely exceed 3:1, and the coarse grain size of olivine. Many samples contain evidence for reactive porous flow. Textures of all peridotite samples from 12°S suggest extensive reaction with percolating melts. Opx-olivine grain boundaries are lobate but highly irregular. Coarse matrix olivine can be clearly distinguished from relatively fine-grained olivines at opx grain boundaries, where abundant interstitial (~<30 µm) spinel

stringers are precipitated. Further, the average opx porphyroclast size in dunitic sample CIRCE93-2 is smaller than in the harzburgitic samples from this dredge haul. All Vema FZ peridotites have opx dissolution textures similar to those from 12°S. However, they contain variable amounts of medium-grained (80-300 µm), mainly stress-free interstitial cpx. One harzburgite (sample ANTP134-3) contains a coarse (~500 µm) magmatically twinned cpx. This suggest that melt extraction in these samples was incomplete. Although plagioclase, which is commonly a direct indicator for melt entrapment, is absent in all the selected CIR samples, some of these 'residues' contain textural evidence for incomplete melt extraction. In two harzburgites from 12°S, rare cpx occurs as small (~20-50 µm wide, 0.1-0.5 mm long), irregular interstitial stringers in the olivine matrix, or at olivine-opx grain boundaries. These textures suggest that melt entrapment led to cpx precipitation on grain boundaries. This may indicate that local melt extraction at Vema FZ was not as efficient as below the CIR axis at 12°S. Similarly, at Green Rock Hill (GRH), which is also away from large transform offsets, cpx occurs mainly as porphyroclasts or in coarse recrystallized aggregates of cpx and subordinate opx. In these harzburgites fine-grained (<50 µm) interstitial cpx occur as well but are very rare. Argo FZ peridotites have similar textures as the GRH harzburgites, but with higher modal cpx. As indicated by the relatively large modal variation, the MCFZ harzburgites show variable textures. Porphyroclastic cpx dominates in the modally more fertile samples. In the modally depleted samples cpx is interstitial, mainly occurring at opx grain boundaries.

2.3. Analytical methods

Anhydrous silicates and spinels were analyzed for major elements on a five-spectrometer JEOL JXA 8900RL electron probe microanalyzer at the University of Mainz using an acceleration potential of 20 kV, a beam current of 20 nA and a spot size of 2 µm. Cpx grains were analyzed for trace elements (selected REE and Ti, V, Cr, Sr, Y, Zr) by secondary ion mass spectrometry (SIMS) on a recently upgraded Cameca IMS-3f in Mainz. Spots were selected for ion probe analysis after detailed petrographic and electron microprobe study. Only optically clear domains that show no signs of alteration or opx exsolution were analyzed. Negative oxygen ions were used as a primary source, using an accelating potential of 12.5 kV and 20 nA beam current, and a high-energy offset of -80 eV for most analyses. The spot size for these conditions was 15-20 µm. For very small grains,

the beam current was reduced to 10 nA, resulting in a smaller spot size (around 10 µm). Each measurement consisted of six cycles, where in each cycle the following masses ^{16}O, ^{30}Si, ^{47}Ti, ^{51}V, ^{52}Cr, ^{88}Sr, ^{89}Y, ^{90}Zr, ^{139}La, ^{140}Ce, ^{146}Nd, ^{147}Sm, ^{153}Eu, ^{157}Gd, ^{163}Dy, ^{167}Er, and ^{174}Yb were analyzed in this order. ^{30}Si (3.1 % isotopic abundance) was used as a reference mass, which is known from electron microprobe analysis. For each cycle, time-corrected mass to ^{30}Si ratios were formed after dead time and background corrections. The average of these ratios was used to calculate the element concentration. Although the applied energy filtering technique (SHIMIZU ET AL., 1978) eliminates the effect of most molecular interferences, interfering molecules were observed and had to be corrected. Especially oxides of the MREE interfere with the HREE. The oxide/metal ratios, necessary for applying the correction, were determined in advance by standard measurements on all masses between 133 and 180, applying an iterative data reduction procedure similar to that presented by (ZINNER and CROZAZ, 1986). The well-studied glass GOR132 (JOCHUM ET AL., 2000) was used as an external standard. The overall accuracy is better than 20% for all REE and better than 12% for all other elements (95% confidence level).

To distinguish ‚real' counts from background noise at extremely low counting rates, separate background measurements with long counting times between 10 and 30 minutes were carried out. All reported analyses are corrected for the background, which lies around 10^{-3} counts per second (cps) on average. For the REE this corresponds to values that range from 0.6 ng/g (La) to 4 ng/g (Sm) (Table 4). This low background is confirmed by a virtually La-free sample ANTP84-11, where only two counts were registered on mass 139 in twelve cycles of 30 seconds each ($5.5 \cdot 10^{-3}$ cps).

Some analyses were duplicated at the Cameca IMS-3f ion microprobe at Woods Hole Oceanographic Institution, as noted in Table 5. The analytical conditions for these measurements are reported in JOHNSON ET AL. (1990).

2.4. Results

2.4.1. Mineral compositions

The mineral major element compositions of all the residual CIR peridotites (Tables 2-5) lie within the range of typical oceanic upper mantle melting residues (DICK, 1989; DICK and

BULLEN, 1984; DICK ET AL., 1984; MICHAEL and BONATTI, 1985). Significant within-sample variations, such as lower Al and Cr content and slightly higher Mg# (= molar Mg/(Mg+Fe) ratio) in fine-grained stress-free pyroxenes with respect to porphyroclast cores, are also typical features of abyssal peridotites, attributed to subsolidus recrystallization (HAMLYN and BONATTI, 1980; SINTON, 1978; TARTAROTTI ET AL., 1995). However, global melting trends show that with increasing degree of melting, the Al content of pyroxene decreases and silicate Mg# increases. Therefore, textural relationships are important, because cooling trends cannot easily be distinguished from melting trends. Hence, porphyroclast core compositions were used for comparison, whenever possible. Unfortunately, in some samples porphyroclasts were either absent or too intensely altered.

Based on whether major element compositional variation is observed within one single dredge haul, two groups can be defined. *Group 1* has a narrow range in the mineral chemistry, *Group 2* shows larger chemical variations.

2.4.1.1. Spinel

Spinel Cr# (= molar Cr/(Cr+Al)) is generally accepted as a sensitive indicator for the extent of melting (DICK and BULLEN, 1984), and melt-peridotite reaction (KELEMEN ET AL., 1992). This value increases with increasing degrees of melting. Spinel Cr# of CIR peridotites range from 0.17 for a harzburgite from Marie Celeste FZ, to 0.57 for the axial dunite from 12°S. This corresponds to 3 to 17 percent of partial melting (HELLEBRAND ET AL., submitted). Since the strong serpentinization in most samples may obscure presence of plagioclase, titanium content of spinel is used as an additional monitor for this phase. Commonly, the titanium content in spinels of plagioclase-bearing abyssal peridotites is higher than in plagioclase-free melting residues (DICK, 1989). In the selected CIR peridotites, all titanium contents are below 0.2 wt.% TiO_2. In Fig. 2 the average spinel Cr# of each sample is plotted versus its titanium content. Because of the low absolute variation in Ti, the error bar (1 sigma) reflects the analytical uncertainty rather than within-sample inhomogeneity. Error bars on Cr# are only seen in some *Group 2* samples, indicating that in these samples heterogeneity also exists on thin section scale.

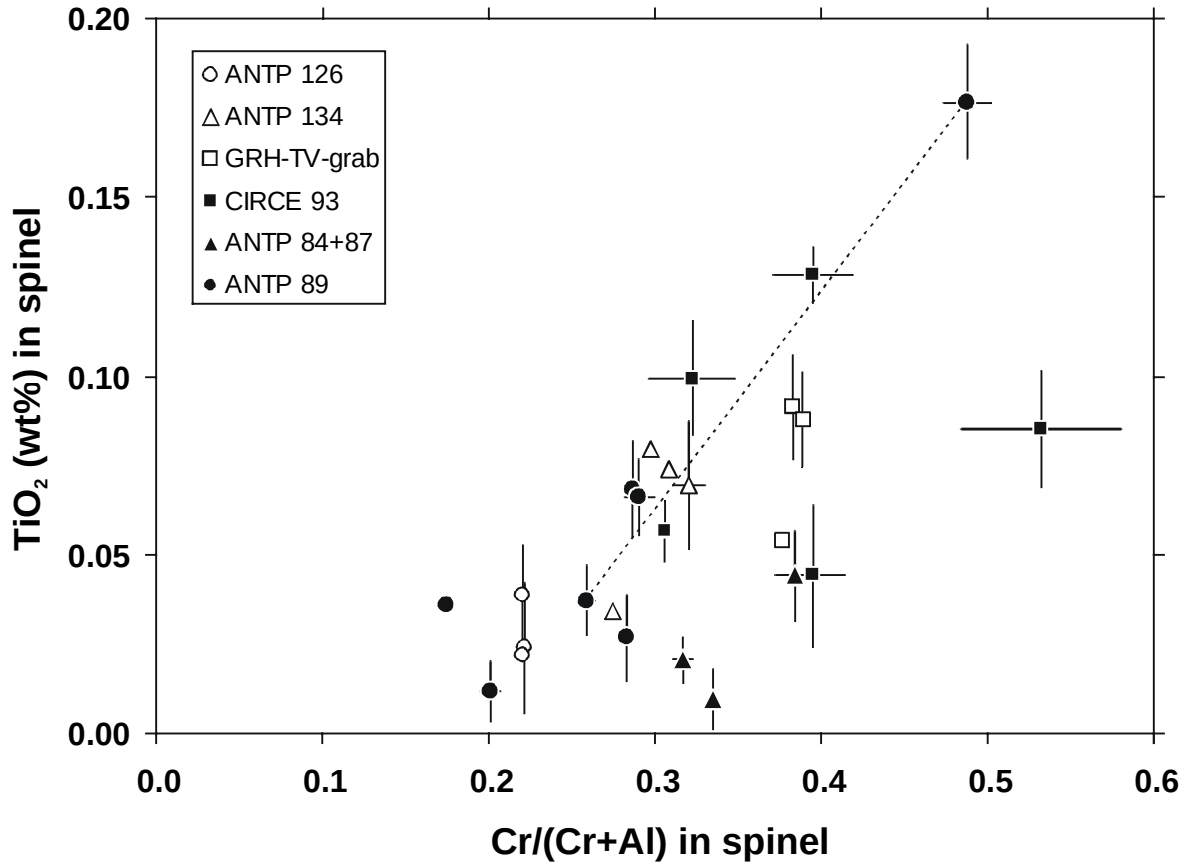

Fig. 2: Spinel TiO_2 content (wt.%) vs. spinel molar Cr/(Cr+Al) value of CIR residual peridotites. Open symbols *Group 1*, closed symbols *Group 2* samples. Error bar is one standard deviation to illustrate the within-sample variation of *Group 2* peridotites. Dashed line connects two chemically distinct spinels in sample ANTP89-2.

Group 1 consists of peridotites from Argo FZ (ANTP126-2, ANTP126-5, ANTP126-D5), Green Rock Hill (60GTV, 74GTV, 31GTV) and Vema FZ (ANTP134-3, ANTP134-5, ANTP134-7, ANTP134-8). Spinels from the first two localities have constant Cr# of 0.22 and 0.38, respectively. Limited scatter is observed in the spinels of the four Vema FZ harzburgites, with Cr# between 0.27 and 0.33. Two vein-bearing peridotites from this dredge haul reach Cr# of 0.27 far away from the magmatic vein, and 0.39, close to the crosscutting vein. This shows that the crosscutting magmatic veins have produced a small reaction zone in which the spinel compositions were modified. More than 2 cm away from this vein, spinel compositions show normal constant values (HELLEBRAND ET AL., 1999).

Group 2 consists of the axial peridotites from 12°S (CIRCE93 samples) and the samples from Marie Celeste FZ (dredges ANTP84, 87, and 89). The Cr# of the modally depleted 12°S peridotites ranges from 0.29 for ‘cpx-rich’ harzburgite CIRCE93-4 to 0.57 for the cpx-free dunite CIRCE93-5. Further, all samples are heterogeneous as indicated by the error

bars in Fig. 2. In CIRCE93-2 the Cr# ranges from 0.30 to 0.36 and CIRCE93-5 has two distinct grains of Cr# 0.49 and 0.57, respectively. These samples show no indications for the presence of plagioclase or magmatic dikelets, and neither is there any sign of Al-bearing alteration phases, such as chlorite.

TABLE 2. Average major element compositions (in wt.%) of spinels of CIR peridotites analysed by electron microprobe

Location	Sample	gr [a]	n [b]	TiO2	Al2O3	Cr2O3	FeO*	MgO	MnO	NiO	Total	Mg#[c]	Cr#[d]
Vema FZ	**ANTP134-3**	1	1	0.03	43.52	24.58	14.28	17.89	0.13	0.21	100.64	0.734	0.275
	ANTP134-5	1	2	0.07	41.43	27.53	12.97	18.45	0.14	0.21	100.79	0.759	0.308
	ANTP134-7	1	3	0.07	40.84	28.69	12.34	18.45	0.13	0.24	100.77	0.762	0.320
	ANTP134-8	1	2	0.08	42.38	26.83	12.40	18.40	0.16	0.23	100.46	0.758	0.298
CIR 12 °S	**Circe93-2**	4	10	0.10	40.71	28.87	12.84	18.07	0.16	0.18	100.92	0.747	0.323
	Circe93-3	3	5	0.13	35.37	34.47	13.85	16.97	0.19	0.15	101.13	0.719	0.395
	Circe93-4	1	3	0.06	41.68	27.34	12.66	18.51	0.15	0.21	100.61	0.763	0.306
	Circe93-5	2	4	0.09	25.88	43.86	15.98	15.38	0.23	0.09	101.50	0.680	0.533
	Circe93-7	3	6	0.04	35.29	34.32	13.93	17.03	0.20	0.15	100.95	0.724	0.395
Argo FZ	**ANTP126-2**	3	6	0.02	48.33	20.45	11.12	19.96	0.13	0.27	100.28	0.800	0.221
	ANTP126-5	1	2	0.02	48.50	20.44	10.98	19.89	0.12	0.27	100.21	0.797	0.220
	ANTP126-D5	3	6	0.04	48.55	20.53	11.03	19.85	0.11	0.27	100.38	0.795	0.221
Marie Celeste FZ	**ANTP84-11**	1	3	0.01	39.17	29.40	14.52	18.08	0.17	0.20	101.55	0.749	0.335
	ANTP87-5	1	3	0.02	39.93	27.61	15.85	17.82	0.19	0.22	101.64	0.737	0.317
	ANTP87-9	3	6	0.04	34.55	32.16	17.50	17.07	0.18	0.21	101.72	0.721	0.384
	ANTP89-1	2	6	0.07	43.30	26.01	12.65	19.09	0.15	0.24	101.51	0.775	0.287
	ANTP89-2 (1)	2	4	0.04	45.20	23.57	14.10	18.43	0.15	0.23	101.72	0.745	0.259
	ANTP89-2 (2)	1	3	0.18	28.39	40.36	18.17	14.92	0.26	0.09	102.36	0.650	0.488
	ANTP89-5	1	2	0.04	51.60	16.29	13.32	19.66	0.15	0.31	101.36	0.775	0.175
	ANTP89-8	2	4	0.01	50.03	18.83	12.55	19.83	0.15	0.29	101.70	0.783	0.202
	ANTP89-15	3	9	0.07	43.12	26.36	12.90	19.25	0.15	0.24	102.09	0.778	0.291
	ANTP89-17	2	5	0.03	43.67	25.64	13.71	18.17	0.17	0.18	101.57	0.740	0.283
Green Rock Hill	**60GTV**	1	3	0.09	35.95	33.21	14.59	17.10	0.17	0.20	101.31	0.722	0.383
	31GTV	1	2	0.05	35.58	32.07	15.25	16.47	0.19	0.17	99.78	0.708	0.377
	74GTV	2	4	0.09	35.09	33.13	15.04	16.01	0.16	0.20	99.72	0.708	0.387

[a] number of spinel grains analyzed
[b] total number analyses
[c] molar ($Mg/(Mg+Fe^{2+})$)
[d] molar Cr/(Cr+Al)

Dredge ANTP89 from Marie Celeste FZ consists of six texturally residual peridotites, of which the two most cpx-rich (ANTP89-5, ANTP89-8) have Cr# of 0.17 and 0.20, respectively. Three samples (ANTP89-1, ANTP89-15, ANTP89-17) have constant Cr# of 0.28-0.30. The highest Ti concentration of all CIR samples was measured in sample ANTP89-2, which is compositionally very heterogeneous. Two spinel grains have Cr# of 0.26 and TiO_2 concentrations of 0.04 wt.%, and one interstitial grain, 2 cm away from the other two grains reaches high Cr# of 0.49 and TiO_2 of 0.18 wt.%. In Fig. 2, a dashed line connects these points. Although this sample matched all selection criteria of a residual sample, it appears not to be truly residual and will be discussed below in more detail.

Residual peridotites from dredge ANTP84 and 87 consist of 1 and 2 samples, respectively, and therefore their within-dredge variations cannot be discussed. Harzburgite ANTP84-11

has intermediate Cr# (0.33) and very low titanium concentration (< 0.02 wt.% TiO_2). Sample ANTP87-5 has Cr# of 0.31 and TiO_2 of 0.02. Virtually cpx-free harzburgite ANTP87-9 has variable Cr# (0.37 – 0.40) and slightly higher Ti contents (0.03 – 0.07 wt.%).

2.4.1.2. Clinopyroxene

The grouping into dredge hauls with constant and variable compositions cannot be strictly applied to pyroxenes, because these show within-sample variability depending on grain size. This may partly be the result of previously mentioned subsolidus cooling effects.

Still, in *Group 1* all clinopyroxenes from one dredge show similar limited compositional scatter. The three Argo FZ peridotites (ANTP126-2, ANTP126-5, ANTP126-D5) have identical average cpx compositions: low Mg# (0.912 to 0.915), high Al_2O_3 concentrations (5.23 – 5.77 wt.%), low TiO_2 and intermediate Na_2O contents (0.05 – 0.09 and 0.27 – 0.28 wt.%, respectively). This agrees well with their relatively fertile modal compositions.

Clinopyroxene porphyroclasts in all Green Rock Hill harzburgites (60GTV, 74GTV, 31GTV) are characterized by low TiO_2 concentrations (0.08 – 0.10 wt.%) at fairly low Mg# (0.914 – 0.918) and intermediate Al_2O_3 content (4.33 – 4.63 wt.%). With exception of the ultra-depleted Hess Deep harzburgites (DICK and NATLAND, 1996), which were generated in a fast spreading environment, the GRH clinopyroxenes have the lowest sodium concentrations ever reported along a mid-ocean ridge (0.03 – 0.04 wt.% Na_2O).

The residual Vema FZ peridotites (ANTP134-3, ANTP134-5, ANTP134-7, ANTP134-8) have variable cpx compositions, as already suggested by their variable spinel Cr#. Sodium concentrations range from 0.50 to 0.64 wt.% Na_2O and TiO_2 from 0.11 to 0.15 wt.%. Variations are also seen in Mg# (0.918 – 0.931) and Al_2O_3 (4.32 – 5.37 wt.%), but compositions of the individual harzburgites largely overlap. Clinopyroxene grains measured at 40 mm distance from the magmatic vein in sample ANTP134-4 have an identical major element composition as ANTP134-8 cpx. Sample ANTP134-3, in which a coarse magmatic cpx twin is preserved, is similar in Mg# and Al_2O_3 concentrations, but has the lowest sodium abundance of the Vema FZ peridotites. The composition of the twinned cpx with its opx exsolution lamellae does not deviate from other cpx grains in this sample.

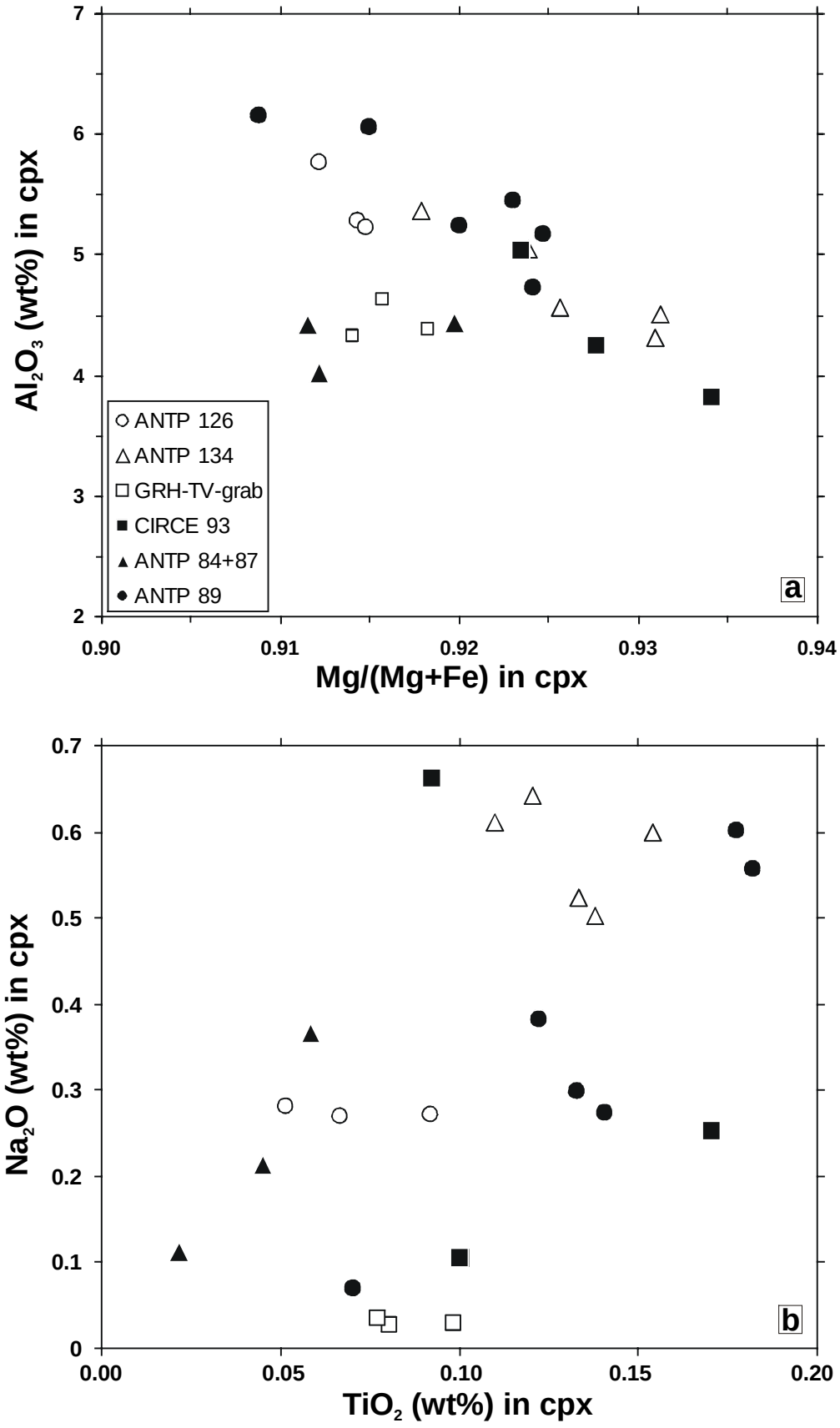

Fig. 3: Clinopyroxene (**a**) Al_2O_3 (wt.%) vs. Mg/(Mg+Fe) and (**b**) Na_2O (wt.%) vs. TiO_2 (wt.%). Open symbols *Group 1*, closed symbols *Group 2* samples.

In *Group 2*, the variation in cpx chemistry is much larger than in *Group 1*. Although only three out of five peridotites (CIRCE93-2, CIRCE93-4, CIRCE93-7) from the CIR axis at 12°S contain cpx, each one has an entirely different composition. The cpx porphyroclasts in CIRCE93-4 are characterized by high Mg# (0.923) and low TiO_2 and Na_2O concentrations (both 0.10 wt.%), but intermediate aluminum contents (5.0 wt.% Al_2O_3). The interstitial cpx grains of the modally depleted samples CIRCE93-2 and 93-7 appear more depleted than the porphyroclasts of CIRCE93-4 as suggested by their high Mg# (0.928 and 0.934, respectively), Al_2O_3 contents (4.25 and 3.81 wt.%, respectively) and low TiO_2 contents (0.17 and 0.09 wt.%, respectively). Their sodium contents, however, are higher than expected. In sample CIRCE93-2, sodium is slightly elevated (0.25 wt.% Na_2O), whereas the otherwise depleted signature of CIRCE93-7 accompanied by strong sodium enrichments (Na_2O: 0.66 wt.%).

TABLE 3. Average major element compositions (in wt.%) of clinopyroxenes of CIR peridotites analysed by electron microprobe

Location	Sample	n[a]	SiO2	TiO2	Al2O3	Cr2O3	FeO	MgO	MnO	CaO	NiO	Na2O	K2O	Total	Mg#
Vema FZ	**ANTP134-3**	15	51.47	0.14	4.57	1.37	2.35	16.42	0.09	22.19	0.04	0.50	0.01	99.14	0.926
	ANTP134-4*	7	51.28	0.12	5.05	1.44	2.45	16.65	0.09	21.61	0.04	0.64	0.01	99.38	0.924
	ANTP134-5	4	51.68	0.13	4.32	1.36	2.19	16.53	0.09	22.35	0.04	0.52	0.01	99.21	0.931
	ANTP134-7	13	51.64	0.15	4.51	1.33	2.17	16.49	0.08	22.23	0.04	0.60	0.01	99.26	0.931
	ANTP134-8	3	51.11	0.11	5.37	1.54	2.66	16.65	0.08	20.88	0.04	0.61	0.00	99.04	0.918
CIR 12 °S	**Circe93-2**	14	51.60	0.17	4.25	1.20	2.44	17.52	0.09	21.89	0.05	0.25	0.00	99.44	0.928
	Circe93-4	4	50.28	0.10	5.03	1.43	2.51	17.00	0.08	22.24	0.05	0.10	0.01	98.82	0.923
	Circe93-7	13	52.59	0.09	3.81	1.54	2.19	17.43	0.10	21.76	0.05	0.66	0.01	100.23	0.934
Argo FZ	**ANTP126-2**	11	50.79	0.07	5.28	1.14	2.95	17.63	0.09	20.62	0.05	0.27	0.01	98.89	0.914
	ANTP126-5	3	51.03	0.05	5.77	1.25	3.04	17.70	0.11	19.83	0.06	0.28	0.01	99.13	0.912
	ANTP125-D5	8	51.21	0.09	5.23	1.06	2.95	17.79	0.10	20.42	0.05	0.27	0.02	99.19	0.915
Marie Celeste FZ	**ANTP84-11**	7	50.78	0.02	4.44	1.38	2.72	17.49	0.09	22.76	0.05	0.11	0.01	99.85	0.920
	ANTP87-5	7	51.73	0.05	4.42	1.21	3.12	17.99	0.09	21.45	0.06	0.21	0.00	100.33	0.912
	ANTP87-9	7	52.05	0.06	4.02	1.28	3.09	17.98	0.09	21.26	0.05	0.37	0.00	100.25	0.912
	ANTP89-1	4	50.97	0.18	5.45	1.55	2.47	16.58	0.09	22.01	0.05	0.60	0.01	99.94	0.923
	ANTP89-2	10	51.07	0.12	5.24	1.38	2.58	16.66	0.10	22.73	0.04	0.38	0.01	100.31	0.920
	ANTP89-5	4	50.53	0.14	6.16	1.23	3.01	16.79	0.12	22.03	0.05	0.27	0.00	100.32	0.909
	ANTP89-8	6	50.59	0.13	6.06	1.34	2.74	16.53	0.11	22.50	0.04	0.30	0.00	100.34	0.915
	ANTP89-15	8	51.18	0.18	5.17	1.50	2.45	16.83	0.09	22.35	0.05	0.56	0.00	100.35	0.925
	ANTP89-17	8	51.14	0.07	4.73	1.34	2.52	17.24	0.10	22.94	0.06	0.07	0.00	100.20	0.924
Green Rock Hill	**31GTV**	4	51.87	0.08	4.63	1.35	2.85	17.34	0.08	20.54	0.05	0.03	0.01	98.82	0.916
	60GTV	18	51.17	0.10	4.38	1.36	2.85	17.94	0.09	21.30	0.05	0.03	0.01	99.27	0.918
	74GTV	21	52.12	0.08	4.33	1.32	3.03	18.03	0.09	21.16	0.04	0.04	0.01	100.25	0.914

[a] number of analyses
* Analyses taken ~40mm away from crosscutting magmatic veinlet

Clinopyroxene compositions from dredge ANTP89 harzburgites cover a broad spectrum. The two ‘cpx-rich’ harzburgites (ANTP89-5 and ANTP89-8) that have lowest spinel Cr# have similarly fertile cpx compositions. Their intermediate sodium (0.27 and 0.30 wt.% Na_2O, respectively) and titanium (0.14 and 0.13 wt.% TiO_2, respectively) concentrations, however, are lower than those of modally very depleted samples ANTP89-1 and ANTP89-15. These have average Na_2O concentrations of 0.60 and 0.56 wt.%, respectively, and

both identical TiO_2 concentrations of 0.18 wt.%. Sample ANTP89-17 is strongly depleted in TiO_2 and Na_2O (both 0.07 wt.%) and has low Al_2O_3 content and high Mg#.

Clinopyroxene porphyroclasts in ANTP84-11 have intermediate Mg# (0.917 – 0.922), low Al_2O_3 (4.26 – 4.63 wt.%) and low Na_2O (0.1 wt.%). They have the lowest titanium concentrations of all studied samples (0.03 wt.% TiO_2), very similar to the depleted cpx from the Bouvet FZ on the Southwest Indian Ridge, close to the Bouvet hotspot (JOHNSON ET AL., 1990). ANTP87-5 and ANTP87-9 both have equally low Mg# (0.912) and titanium contents (0.05 and 0.06 wt.%, respectively). Their Na_2O contents are much higher (0.21 and 0.37 wt.%, respectively).

Clinopyroxene rare earth element (REE) patterns of *Group 1* and *Group 2* peridotites are shown in Fig. 4 and listed in Table 4. In the REE-diagrams, the abyssal peridotite field after JOHNSON ET AL. (1990), which includes only cpx data from the very slow spreading Southwest Indian and American Antarctic Ridges, is shown for comparison.

TABLE 4. Trace element concentrations in µg/g of CIR peridotite clinopyroxenes

Sample	n	Lab [a]	Ti	Sr	Y	Zr	La	Ce	Nd	Sm	Eu	Gd	Dy	Er	Yb
ANTP134-3	2	MPI	705	0.63	6.2	0.62	0.001	0.014	0.24	0.34	0.14	0.66	1.22	0.84	0.86
	2	WHOI	668	1.35	6.0	1.0		0.016	0.25	0.25	0.12		0.86	0.62	0.56
ANTP134-4*	3	MPI	600	0.88	5.7	0.54	0.002	0.036	0.26	0.27	0.13	0.68	1.09	0.73	0.83
	3	WHOI	628	1.07	5.8	1.0		0.035	0.31	0.30	0.12		0.78	0.55	0.57
ANTP134-7	4	WHOI	858	1.30	6.5	1.6		0.025	0.28	0.25	0.12		0.85	0.59	0.56
ANTP134-8	1	MPI	544	0.65	4.7	0.47	0.002	0.024	0.19	0.19	0.08	0.65	0.93	0.54	0.58
	3	WHOI	641	0.98	6.1	1.2		0.033	0.29	0.26	0.14		0.87	0.56	0.62
CIRCE 93-2	2	MPI	881	1.19	5.4	0.40	0.014	0.028	0.06	0.12	0.06	0.42	0.75	0.64	0.72
	2	WHOI	825	1.60	4.8	0.76			0.12	0.14	0.07		0.64	0.51	0.49
CIRCE 93-4	2	MPI	503	0.44	5.0	0.19	0.003	0.013	0.11	0.11	0.05	0.37	0.89	0.63	0.74
	2	WHOI	451	1.18	5.1	0.53		0.016	0.13	0.14	0.06		0.85	0.60	0.58
CIRCE 93-7	2	MPI	549	3.24	4.2	3.5	0.015	0.095	0.50	0.46	0.21	0.84	0.84	0.44	0.53
ANTP126-2	2	MPI	357	0.54	4.5	0.21	0.009	0.049	0.04	0.07	0.04	0.25	0.73	0.61	0.66
ANTP126-5	2	MPI	354	0.47	4.6	0.17	0.010	0.045	0.06	0.07	0.04	0.34	0.74	0.62	0.75
	2	WHOI						0.041	0.09	0.09	0.05		0.61	0.47	0.57
ANTP125-D5	2	MPI	471	0.58	5.2	0.17	0.005	0.020	0.05	0.13	0.06	0.39	0.94	0.71	0.84
	2	WHOI						0.020	0.08	0.12	0.08		0.76	0.54	0.62
ANTP84-11	2	MPI	118	0.19	2.0	0.07	b.d.	0.002	0.005	0.009	0.003	0.06	0.29	0.29	0.40
ANTP87-5	2	MPI	236	0.25	2.8	0.08	0.002	0.002	b.d.	0.03	0.02	0.13	0.42	0.46	0.49
ANTP87-9	2	MPI	315	0.48	3.8	0.11	0.005	0.007	0.021	0.04	0.04	0.22	0.56	0.47	0.59
ANTP89-1	2	MPI	834	0.72	6.8	0.78	0.002	0.013	0.21	0.30	0.13	0.76	1.33	0.84	0.95
ANTP89-2	2	MPI	700	0.40	6.7	0.28	0.002	0.006	0.06	0.16	0.10	0.55	1.22	0.84	0.91
ANTP89-5	3	MPI	722	0.27	7.5	0.21	0.001	0.005	0.13	0.23	0.13	0.73	1.38	0.95	1.08
ANTP89-8	2	MPI	746	0.29	7.1	0.26	0.003	0.006	0.12	0.21	0.13	0.75	1.33	0.97	0.99
ANTP89-15	4	MPI	971	0.63	7.2	0.95	0.001	0.008	0.17	0.21	0.13	0.71	1.26	0.93	0.92
ANTP89-17	4	MPI	393	0.33	4.2	0.13	0.014	0.013	0.012	0.06	0.04	0.24	0.64	0.57	0.72
31GTV	2	MPI	457	0.39	3.4	0.16	0.002	0.004	0.04	0.06	0.03	0.23	0.61	0.43	0.58
60GTV	1	MPI	478	0.42	3.5	0.13	0.005	0.017	0.03	0.09	0.04	0.27	0.60	0.43	0.58
74GTV	3	MPI	420	0.29	3.2	0.12	0.001	0.003	0.02	0.04	0.02	0.18	0.39	0.33	0.33
REE detect. lim. [b]		MPI					0.0006	0.0007	0.003	0.004	0.001	0.004	0.002	0.003	0.001

[a] MPI = Max-Planck-Institut für Chemie; WHOI = Woods Hole Oceanographic Institution

[b] REE detection limit = 6 x background

* Analyses taken ~40mm away from crosscutting magmatic veinlet

Variation-based grouping of the CIR peridotites is also reflected by their cpx trace element signatures, although the spread in *Group 2* is limited. *Group 1* samples from Argo FZ, GRH and Vema FZ, which all have identical within-dredge major element compositions, also have trace element compositions that are identical within error (Fig. 4a-c). All samples plot in the most depleted part of the abyssal peridotite field and have very low HREE concentrations. Vema FZ peridotites appear to be the most fertile and have the highest M- to HREE concentrations of *Group 1* (Fig. 4c). Their flat chondrite-normalized M- to HREE patterns are accompanied by steeply plunging LREE. The Argo FZ samples on the other hand (Fig. 4a), have more gradually decreasing patterns from H- to LREE, and their La and Ce abundances are higher than in the clinopyroxenes of the Vema FZ. Despite the absence of any nearby hotspot in the vicinity of the Rodrigues Triple Junction, the Green Rock Hill peridotites (Fig. 4b) are as depleted in REE as the most depleted harzburgite from the hotspot-influenced Bouvet FZ, which is in good agreement with their extremely low sodium concentrations. The minor La inflections in samples 60GTV and 74GTV were measured in four out of five analyses, indicating that they are not analytical artifacts or local effects.

The most remarkable feature of *Group 2* (CIR axis 12°S, and Marie Celeste FZ) is the ultra-depleted clinopyroxene composition of sample ANTP84-11 (Fig. 4e). The clinopyroxenes of this sample have four- to sixfold lower L- to MREE concentrations than those from hotspot-near Bouvet FZ (JOHNSON ET AL., 1990). Further, sample ANTP84-11 has the lowest Sr, Zr, and Ti concentrations reported for cpx in abyssal peridotites (0.19, 0.07 and 118 µg/g, respectively). The titanium concentrations measured by ion probe agree well with those of the electron microprobe. The two cpx-poor harzburgites from dredge ANTP87 have similarly depleted patterns compared to the Bouvet FZ cpx, but both have slight LREE inflections (Fig. 4e). Their La concentrations are significantly higher (5- to 10-fold) than those of ANTP84-11.

With the exception of sample ANTP89-17, clinopyroxenes in ANTP89 peridotites show very similar REE patterns (Fig. 4f). Of the entire CIR sample set, they have the highest HREE concentrations (Yb_N ~5). Their average REE pattern is very similar to that of the Vema FZ peridotites, but with significantly lower Ce concentrations. Harzburgite ANTP89-17 has a deviating REE pattern that is almost identical to the most depleted cpx from Bouvet FZ (JOHNSON ET AL., 1990), but is characterized by a strong LREE inflection.

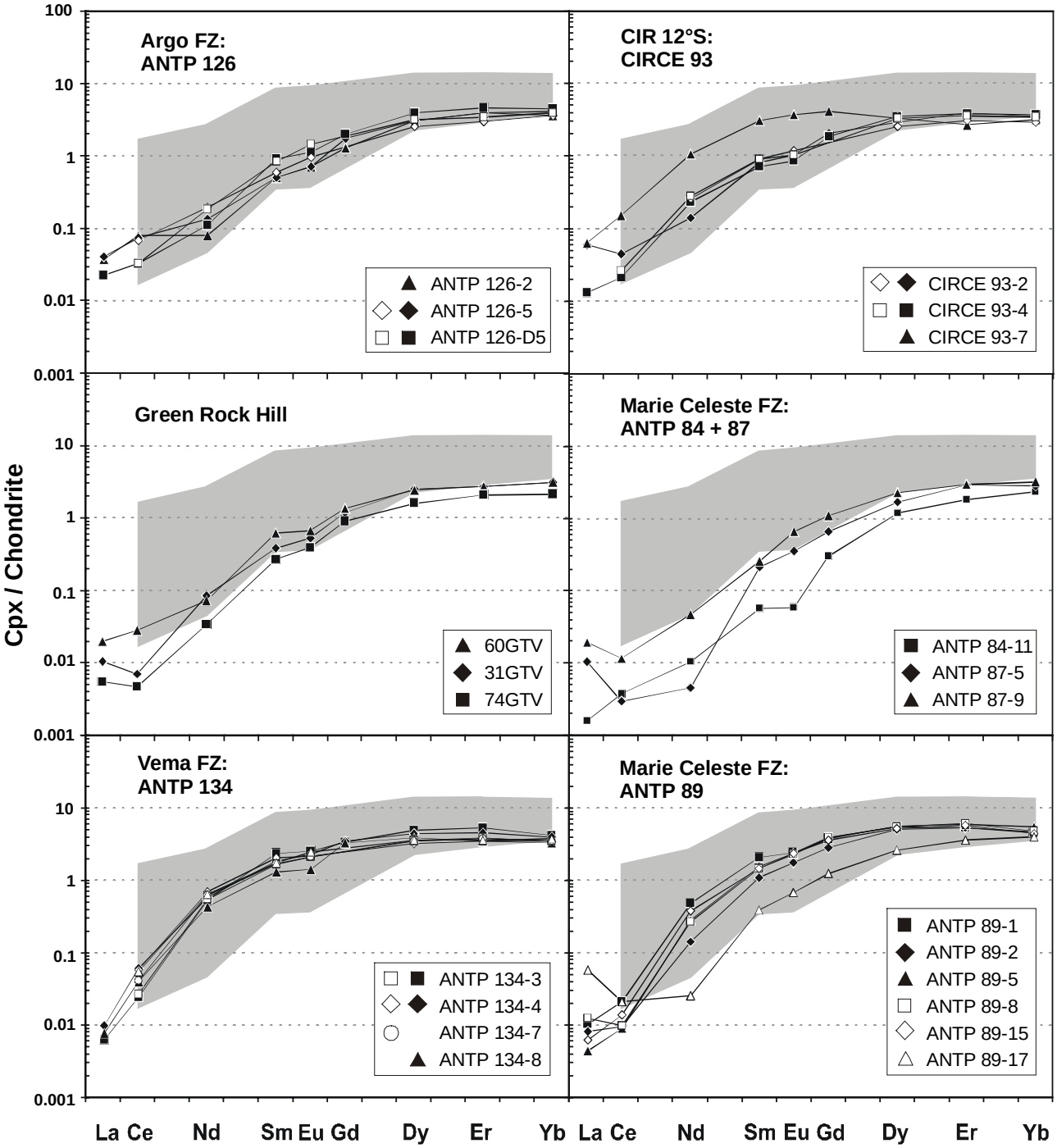

Fig. 4: Chondrite-normalized clinopyroxene REE patterns. Grey field represents the range for abyssal peridotite after JOHNSON ET AL. (1990). The left panel (**a-c**) shows cpx REE patterns for *Group 1* with hardly any compositional variation. *Group 2* samples in the right panel (**d-f**) have larger within-dredge variation. Closed symbols: MPI analyses, open symbols: WHOI analyses except MCFZ samples MPI. See discussion in the text. Chondrite normalization values taken from ANDERS and GREVESSE (1989).

Two out of three cpx-bearing CIR 12°S peridotites (samples CIRCE93-2 and CIRCE93-4) have identical trace element compositions (Fig. 4d), except for the La and Ce enrichment in CIRCE93-2. Most uncommon is the hump-shaped pattern of CIRCE93-7, with the

highest L- to MREE and among the lowest Yb concentrations of the CIR samples. The pattern resembles the hump-shaped REE patterns of clinopyroxenes in peridotite samples Vulc5:41-13 and Vulc5:41-15 from the Bullard FZ (JOHNSON ET AL., 1990).

2.4.1.3. Orthopyroxene

Opx shows similar compositional variation as cpx in terms of Mg#, Al_2O_3 and Cr_2O_3. However, additional geochemical information can be obtained from peridotites in which cpx is absent, or only occurs as fine-grained interstitial grains. In Table 5 only compositions of opx porphyroclast cores are listed. Recrystallized neoblast have systematically lower Al and Cr content, while the Mg# are indistinguishable from porphyroclast compositions. Opx in cpx-free sample CIRCE93-5 has lowest Al content (1.76 wt.% Al_2O_3) ever reported for mid-ocean ridge melting residues. Further, all opx porphyroclasts in 12°S samples have very high Mg# from 0.914 to 0.925.

TABLE 5. Average major element compositions (in wt.%) of orthopyroxenes of CIR peridotites analysed by electron microprobe

Location	Sample	n[a]	SiO2	TiO2	Al2O3	Cr2O3	FeO	MgO	MnO	CaO	NiO	Na2O	Total	Mg#[b]
Vema FZ	**ANTP134-3**	6	54.38	0.05	3.97	0.87	5.67	33.13	0.13	1.27	0.09	0.03	99.59	0.912
	ANTP134-4[b]	4	54.32	0.05	4.14	0.91	5.54	32.89	0.12	1.75	0.10	0.04	99.85	0.914
	ANTP134-5	2	54.35	0.04	4.05	0.91	5.49	33.18	0.09	1.39	0.11	0.01	99.63	0.915
	ANTP134-8	2	54.05	0.05	4.26	0.98	5.39	32.44	0.13	2.10	0.09	0.03	99.51	0.915
CIR 12 °S	**Circe93-2**	4	54.50	0.06	3.84	0.93	5.38	32.94	0.13	2.06	0.10	0.00	99.94	0.916
	Circe93-3	2	55.13	0.09	3.17	0.93	5.08	33.46	0.12	1.62	0.10	0.06	99.73	0.922
	Circe93-4	2	53.58	0.06	4.10	1.02	5.48	32.59	0.17	2.45	0.11	0.03	99.58	0.914
	Circe93-5	2	56.13	0.04	1.76	0.81	4.99	34.48	0.14	1.47	0.09	0.05	99.97	0.925
	Circe93-7	6	55.83	0.02	2.87	0.83	5.14	33.99	0.12	1.82	0.10	0.06	100.79	0.922
Argo FZ	**ANTP126-2**	4	54.04	0.04	4.10	0.73	5.63	32.69	0.12	1.94	0.10	0.04	99.41	0.912
	ANTP126-5	2	54.28	0.01	4.70	0.91	5.67	32.59	0.12	1.56	0.11	0.02	99.96	0.911
	ANTP125-D5	4	53.97	0.03	4.57	0.78	5.71	32.52	0.15	1.94	0.10	0.01	99.78	0.910
Marie Celeste FZ	**ANTP84-11**	3	54.58	0.01	3.31	0.75	6.15	33.84	0.15	1.66	0.09	0.00	100.55	0.907
	ANTP87-5	2	54.96	0.01	3.54	0.75	5.75	33.38	0.13	1.94	0.09	0.01	100.53	0.912
	ANTP87-9	4	55.13	0.05	2.89	0.91	5.54	33.85	0.13	2.13	0.09	0.08	100.79	0.916
	ANTP89-1	1	53.81	0.06	4.48	1.06	5.21	31.39	0.11	3.59	0.08	0.06	99.87	0.915
	ANTP89-2	9	54.37	0.04	4.36	0.95	5.68	33.15	0.14	2.43	0.10	0.05	101.27	0.912
	ANTP89-5	3	53.62	0.03	5.19	0.87	6.34	32.62	0.13	1.47	0.10	0.04	100.42	0.902
	ANTP89-8	1	53.90	0.03	4.81	0.85	5.87	33.08	0.15	1.97	0.12	0.02	100.80	0.909
	ANTP89-15	3	54.39	0.04	4.18	0.97	5.85	34.13	0.13	1.23	0.10	0.02	101.05	0.912
	ANTP89-17	3	54.37	0.02	3.95	0.94	6.03	33.07	0.14	2.16	0.10	0.00	100.79	0.907

[a] number of analyses
[b] molar (Mg/(Mg+Fe)
* Analyses taken ~40mm away from crosscutting magmatic veinlet

2.4.1.4. Olivine

Because of the strong alteration of the mantle rocks, olivine compositions could only be obtained on few samples (Table 6). Systematic variations of forsterite (from 0.909 to

0.921) or Ni contents (from 0.37-0.40 wt.% NiO) with modal or pyroxene composition is not observed. However, the modally depleted harzburgite and dunite from 12°S have the highest forsterite content of all CIR samples.

TABLE 6. Average major element compositions (in wt.%) of olivines of CIR peridotites analysed by electron microprobe

Location	Analysis	n[a]	SiO2	TiO2	Al2O3	Cr2O3	FeO	MgO	MnO	CaO	NiO	Total	Mg#[b]
Vema FZ	ANTP134-3	5	40.15	0.00	0.00	0.01	8.56	50.70	0.13	0.02	0.39	99.98	0.913
	ANTP134-4*	6	40.48	0.01	0.01	0.01	8.52	51.06	0.12	0.02	0.38	100.62	0.914
	ANTP134-5	2	40.00	0.00	0.00	0.02	8.44	51.46	0.11	0.05	0.39	100.47	0.916
	ANTP134-8	2	40.26	0.01	0.01	0.02	8.47	50.51	0.12	0.05	0.38	99.86	0.914
CIR 12 °S	Circe93-2	6	40.27	0.01	0.00	0.02	8.62	51.10	0.11	0.05	0.37	100.55	0.914
	Circe93-3	10	40.50	0.01	0.00	0.01	7.95	51.28	0.12	0.03	0.39	100.30	0.920
	Circe93-4	3	40.09	0.00	0.00	0.00	8.66	50.76	0.13	0.06	0.38	100.10	0.913
	Circe93-5	4	40.61	0.01	0.00	0.01	7.87	51.42	0.11	0.05	0.37	100.47	0.921
	Circe93-7	4	40.81	0.01	0.01	0.08	7.87	51.73	0.12	0.03	0.40	101.08	0.921
Argo FZ	ANTP126-2	3	39.86	0.01	0.01	0.03	9.04	50.47	0.13	0.10	0.38	100.04	0.909
	ANTP126-5	3	40.20	0.00	0.01	0.02	9.01	50.40	0.14	0.05	0.38	100.22	0.909
	ANTP126-D5	2	40.30	0.02	0.03	0.00	8.97	50.33	0.12	0.10	0.38	100.26	0.909

[a] number of analyses
[b] molar (Mg/(Mg+Fe)
* Analyses taken ~40mm away from crosscutting magmatic veinlet

2.5. Discussion

In the following the generation of cpx trace element patterns by fractional melting will be discussed, either by melting in the stability field of spinel peridotite alone, or, by a combination of melting in the garnet peridotite stability field and subsequent further melting under spinel-facies conditions. Finally, processes that disturb simple melting relationships are modeled.

2.5.1. Melting (spinel and garnet stability field)

First, all measured cpx patterns were attempted to be matched by pure fractional melting in the spinel stability field, thereby focussing on the middle- to heavy REE. Theoretically, every infinitesimal melt increment is immediately removed from the residue, leading to extreme LREE depletions in the residue. Even after few percent of melt extraction, the La concentration in residual cpx would drop below the detection limit of the ion probe technique. More realistic melting models such as critical melting include finite residual melt porosities (SOBOLEV and SHIMIZU, 1992). Because minor amounts of melt (~0.1 – 1 %) are always held back in the residue, the LREE are buffered by this small melt fraction, and their decrease is less drastic. For the M- to HREE, however, the difference between pure fractional and critical melting is only significant at high melt fractions (F>~15%).

Starting composition and melt modes were identical to those used by JOHNSON (1998). Several sets of partition coefficients were used. Unless stated otherwise, our mineral-liquid partition coefficients are taken from the compilation of SUHR ET AL. (1998), which are very similar to other such estimates (HART and DUNN, 1993; JOHNSON, 1998). The melting equations used for this modeling are presented in Appendix A and the starting conditions and partition coefficients used for the modeling are listed in Table 7. The results are shown in Fig. 5 and 6.

2.5.1.1. Spinel peridotite melting with 'normal' Kd's

Many samples can be modeled with by fractional melting of a spinel peridotite starting composition. *Group 1* samples in particular have uniform, apparently simple cpx REE patterns. Vema FZ peridotite can be matched perfectly by 10-12% melt extraction in the spinel peridotite stability field using the critical melting equations of SOBOLEV and SHIMIZU (1992) with residual melt porosities between 0% (= perfect fractional melting) and 1% (Fig. 5a). The calculated melting curve better reproduces the measured REE pattern at a high (~1 %) residual melt porosity, especially for the LREE. Green Rock Hill peridotites can be modeled by 15-17% spinel peridotite melting with similar residual melt porosities (Fig. 5b), although the model cpx do not match all elements. In particular, the observed La and Ce concentrations are too high and require an additional process. Argo FZ samples have an apparently unfractionated REE pattern, but the spinel peridotite melting models shown in Fig. 5c do not match these data. The models always predict far higher MREE concentrations than measured in the sample at the observed HREE concentration (F ~11%), or too low HREE concentrations at matching MREE (F ~15%). A combination of fractional melting followed by batch melting, or vice-versa, does not produce matching results either (not shown). Batch melting after fractional melting shifts the cpx REE pattern towards lower absolute concentrations, subparallel to the initial concentration (at the end of fractional melting).

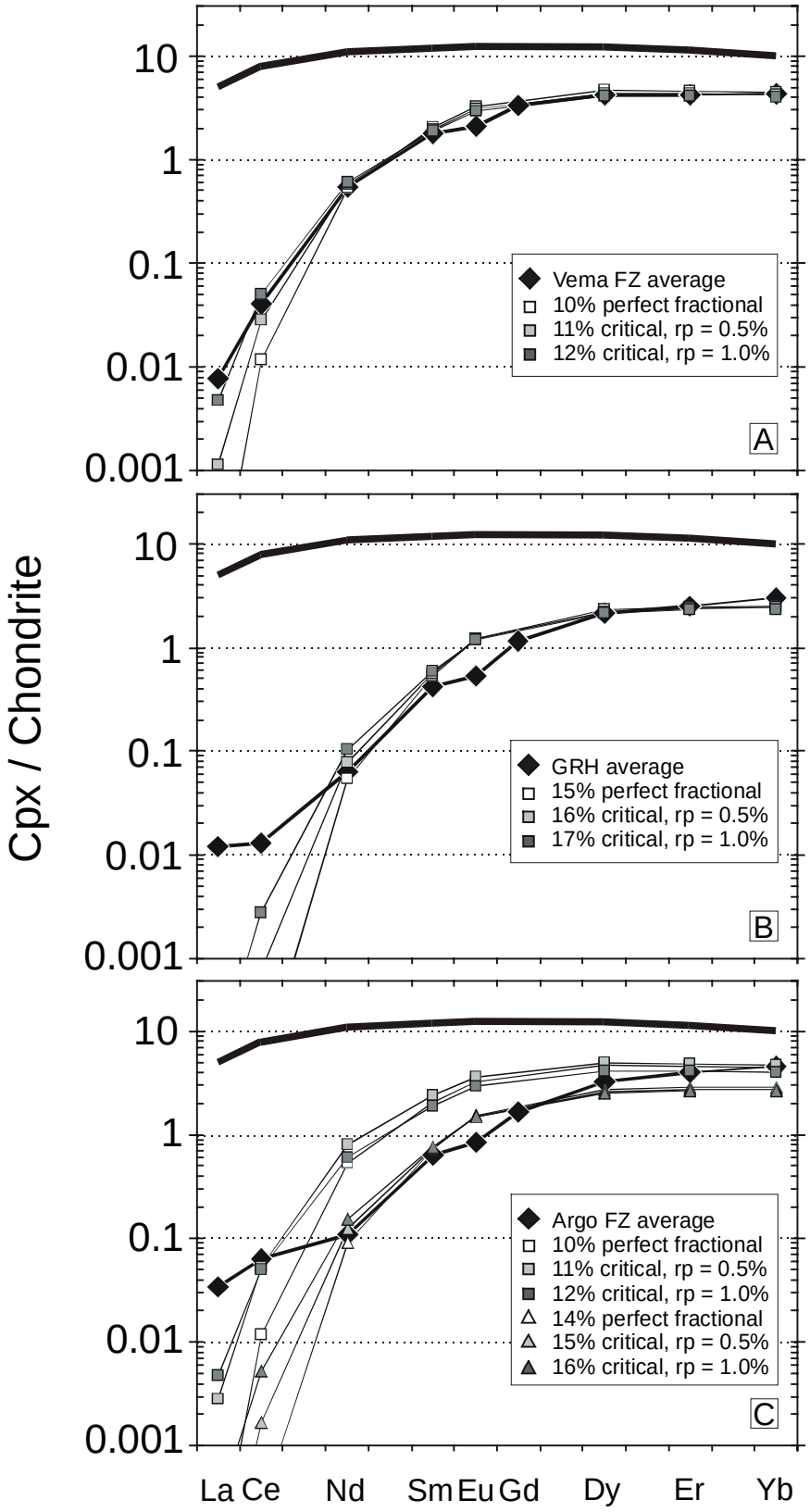

Fig. 5: Result of melting models in the spinel stability field: (**a**) Vema FZ (**b**) Green Rock Hill, and (**c**) Argo FZ. Please note that MREE of the latter are too low at fitting HREE concentrations to be explained by spinel stability field melting. Thick black line represents cpx in equilibrium with Depleted Mantle starting material, 'rp' denotes residual melt porosity used in the critical melting models.

TABLE 7. Melting model: input parameters

	Distribution coefficients [a]						Source
	ol/l	**opx/l**	**cpx/l (1)**	**cpx/l (2)**	**gt/l**	**sp/l**	**composition [b]**
La	0.000007	0.0025	0.06	0.09	0.0035	0.0006	0.91
Ce	0.00001	0.005	0.10	0.16	0.008	0.0006	1.4
Nd	0.00007	0.010	0.20	0.36	0.05	0.0006	1.97
Zr	0.004	0.024	0.12	0.27	0.40	0.070	2.18
Sm	0.001	0.020	0.30	0.67	0.22	0.001	2.23
Eu	0.001	0.030	0.37	0.80	0.45	0.001	2.34
Ti	0.015	0.100	0.35	0.71	0.16	0.150	2.46
Dy	0.004	0.050	0.44	1.10	2.0	0.002	2.44
Er	0.009	0.070	0.43	1.44	3.5	0.003	2.46
Yb	0.014	0.090	0.41	1.43	5.0	0.005	2.5

	Source modes [c]		Melt modes [d]	
	Gt-per	Sp-per	Gt-per	Sp-per
olivine	0.57	0.53	0.04	-0.06
opx	0.21	0.27	-0.19	0.28
cpx	0.13	0.17	1.05	0.67
garnet	0.09	0.00	0.11	0.00
spinel	0.00	0.03	0.00	0.11

[a] From Suhr et al. (1998), except cpx/l (2) from Blundy et al. (1998)
[b] From Johnson et al. (1990), concentrations normalized to CI chondrite (Anders and Grevesse, 1989)
[c] Spinel peridotite modes from Johnson (1998); garnet peridotite modes calculated from sp-peridotite modes using reaction from Johnson et al. (1990)
[d] Garnet peridotite melt modes from Walter (1997); spinel peridotite melt modes from Kinzler (1997)

2.5.1.2. Compatible HREE in cpx or garnet field melting?

- Compatible HREE in cpx

Recent experimental data and theoretical considerations suggest that heavy REE are compatible in Na-rich, Al-rich clinopyroxene on the spinel lherzolite solidus at high pressures (BLUNDY ET AL., 1998). According to the authors, this drastically reduces the required involvement of garnet in the MORB melting region. Because of these far-reaching geodynamic implications, we tested their hypothesis from the perspective of the melting residues, and focussed on the fractionation between middle and heavy REE. Four models simulating melting in the stability field of spinel peridotite were calculated using identical starting conditions but different cpx-liquid partition coefficients. The resulting initial bulk partition coefficient for these models are shown in Fig. 6a. Two melting models use constant partition coefficients: (1) a 'normal' set of $Kd^{cpx/l}$, adapted from SUHR ET AL.

(1998), and (2) the BLUNDY ET AL. (1998) cpx-liquid partition coefficients in which the HREE are moderately compatible in cpx. The two other melting models start with the latter partition coefficients and gradually change to incompatible values with increasing degree of melting. The gradual change from compatible to incompatible HREE in cpx is adapted from BLUNDY ET AL. (1998) and shown for Yb in Fig. 6b. The only difference between these two 'variable Kd'-models is that one simulates perfect fractional melting and the other critical melting with 0.5% residual melt porosity. The results are shown in Fig. 7a, where the chondrite-normalized Sm/Yb ratio is plotted versus the Yb content of cpx. There is a broad range in measured cpx compositions, but a general trend that with increasing degree of melting, both Yb and Sm/Yb decrease. However, at very low Yb concentrations, relatively high Sm/Yb values occur, mainly in the Hess Deep harzburgites. Our main aim is to explain the lowest Sm/Yb at a given (high) Yb concentration, because these provide direct constraints on the melting conditions, rather than on late- or post-melting refertilization (see section '*Coupling and decoupling*'). The first fractional melting model that applies the constant incompatible $Kd^{cpx/l}$ from (SUHR ET AL., 1998) shows a rapid decrease in Sm/Yb with decreasing Yb content. At 20% melting, it has reached a very fractionated $(Sm/Yb)_N$ of 0.06, but the associated Yb concentration is too low to explain the measured cpx data. The second fractional melting model that uses constant compatible HREE $Kd^{cpx/l}$ from BLUNDY ET AL. (1998) yields residual cpx with nearly constant Yb as melting progresses. However, $(Sm/Yb)_N$ of the model cpx decreases slowly, especially at very low melt fractions. At 20% melt extraction, both Sm/Yb and Yb are far too high to match the observations. Both models that use variable $Kd^{cpx/l}$ show a more curved melting trajectory. In the first melting increments the residual cpx is similar to the 'constant compatible' case of the second model. After roughly three percent melt extraction, the melting trajectory is subparallel to the first model. The difference between perfect fractional melting and critical melting with a residual melt porosity of 0.5% is small and becomes only noticable at very high degrees of melting. Compared to perfect fractional melting, the cpx from the critical melting model has a composition that is shifted towards slightly higher $(Sm/Yb)_N$ values and Yb concentrations, because the porosity has a buffering effect on the cpx composition. Overall, these 'variable $Kd^{cpx/l}$ models give a better approach to the abyssal peridotite cpx data than the two 'constant $Kd^{cpx/l}$' models. Still, many clinopyroxenes have too low $(Sm/Yb)_N$ at relatively high Yb concentrations to be explained by melting in the stability field of spinel peridotite. This means that a more effective means of depleting MREE with respect to HREE is required in order to match the observations.

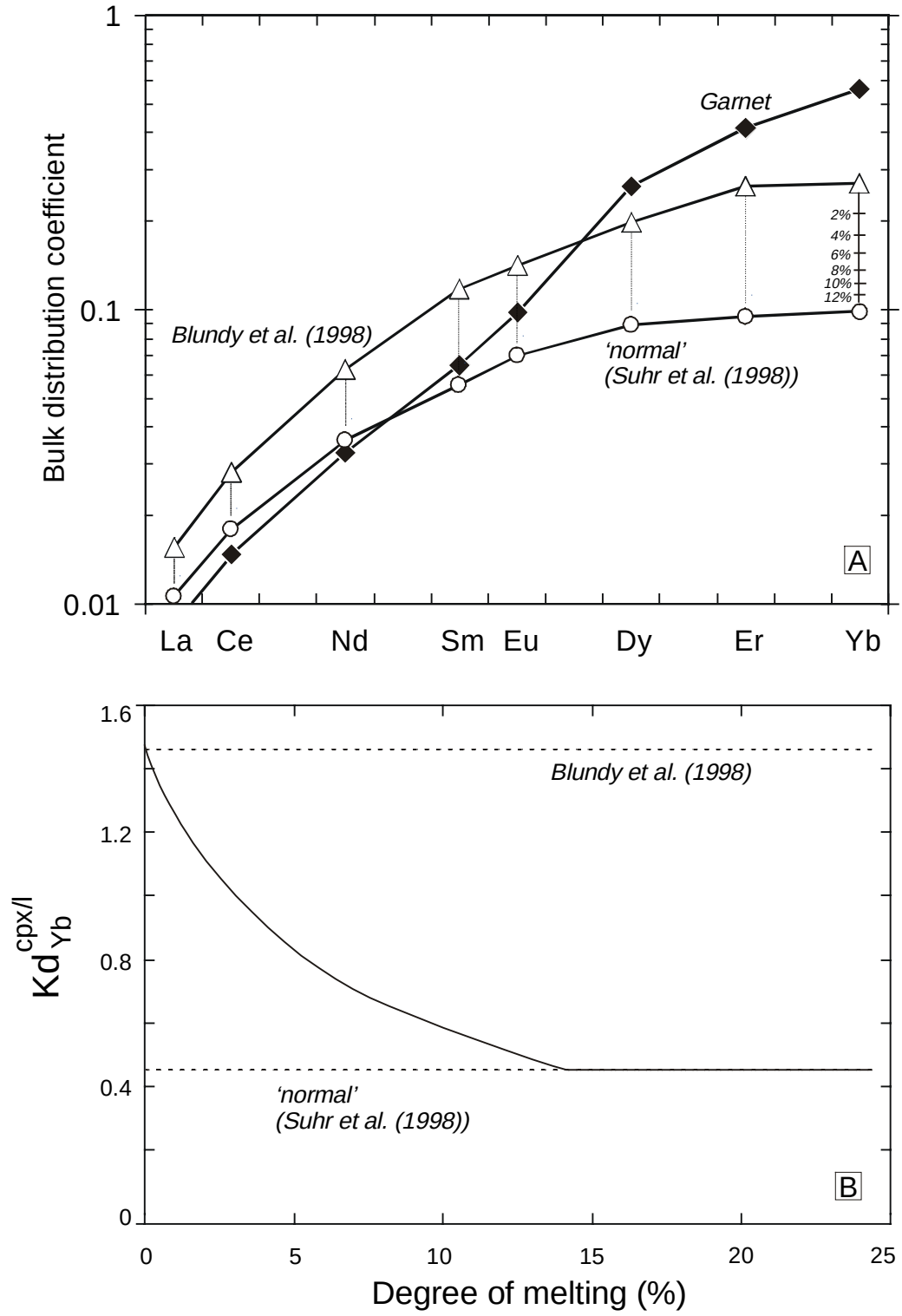

Fig. 6: (**a**) Initial bulk partition coefficients for the REE used for the spinel peridotite and garnet peridotite melting models. All mineral-liquid partition coefficients were kept constant except $Kd^{cpx/l}$. Open circles: 'normal' incompatible $Kd^{cpx/l}$ (SUHR ET AL., 1998), open triangles: compatible $Kd_{HREE}{}^{cpx/l}$ (BLUNDY ET AL., 1998), and closed diamonds: garnet peridotite using $Kd^{cpx/l}$ from SUHR ET AL. (1998). (**b**) Gradual change of $Kd^{cpx/l}$ for Yb from compatible to incompatible as a function of the degree of melting. Adapted from BLUNDY ET AL. (1998). Also shown in Fig. 6a by tick marks for Yb.

- Garnet field melting

HREE are compatible in garnet, and moderately incompatible in clinopyroxene (HART and DUNN, 1993; HAURI and HART, 1995; JOHNSON, 1998). Variable partition coefficients for garnet can be calculated using strain lattice models similar to the ones used for clinopyroxene (VAN WESTRENEN ET AL., 1999; pers. com.). For the HREE these do not vary nearly as much as the $Kd^{cpx/l}$. Spinel cannot accommodate REE in its lattice and therefore does not contribute significantly to the bulk distribution coefficient. Melting in the garnet peridotite field will therefore produce a residue with higher HREE concentrations than melting in the spinel field. This is recorded by the whole rock MREE/HREE value, which will be much lower after melting in the garnet stability field than in the spinel stability field at the same degree of melt extraction.

Previous authors have asserted that cpx REE patterns of residual abyssal peridotites bear evidence for garnet melting because of 'higher' MREE/HREE ratios in certain samples (JOHNSON ET AL., 1990). According to the authors residual clinopyroxene develops humps at the MREE to HREE after small amounts of melting of a garnet lherzolite protolith. This is correct, as long as the cpx is in equilibrium with residual garnet, because garnet hosts most HREE. After ascent into the stability field of spinel peridotite, the garnet-bearing assemblage will react to a garnet-free spinel peridotite. At this garnet breakdown reaction, the REE will be redistributed between the phases of a spinel peridotite assemblage. This will yield an equilibrium cpx with $(Sm/Yb)_N$ <1, rather than a hump-shaped REE pattern. Hump-shaped REE patterns thus cannot be produced by garnet-field melting. Low rather than high MREE to HREE ratios at relatively high HREE concentrations are the only realistic evidence that abyssal peridotites preserve information about melting in the presence of residual garnet.

Because cpx REE patterns in a garnet-bearing assemblage can be misleading, we plot cpx REE compositions that are projected from garnet- to spinel peridotite assemblage. This projection simulates ceasing of melting in the garnet stability field, followed by an instantaneous breakdown reaction from a garnet to a spinel peridotite assemblage and it presents the equilibrium cpx composition after ascent into the spinel stability field. This breakdown reaction consumes olivine and garnet and produces two pyroxenes and spinel (JOHNSON ET AL., 1990):

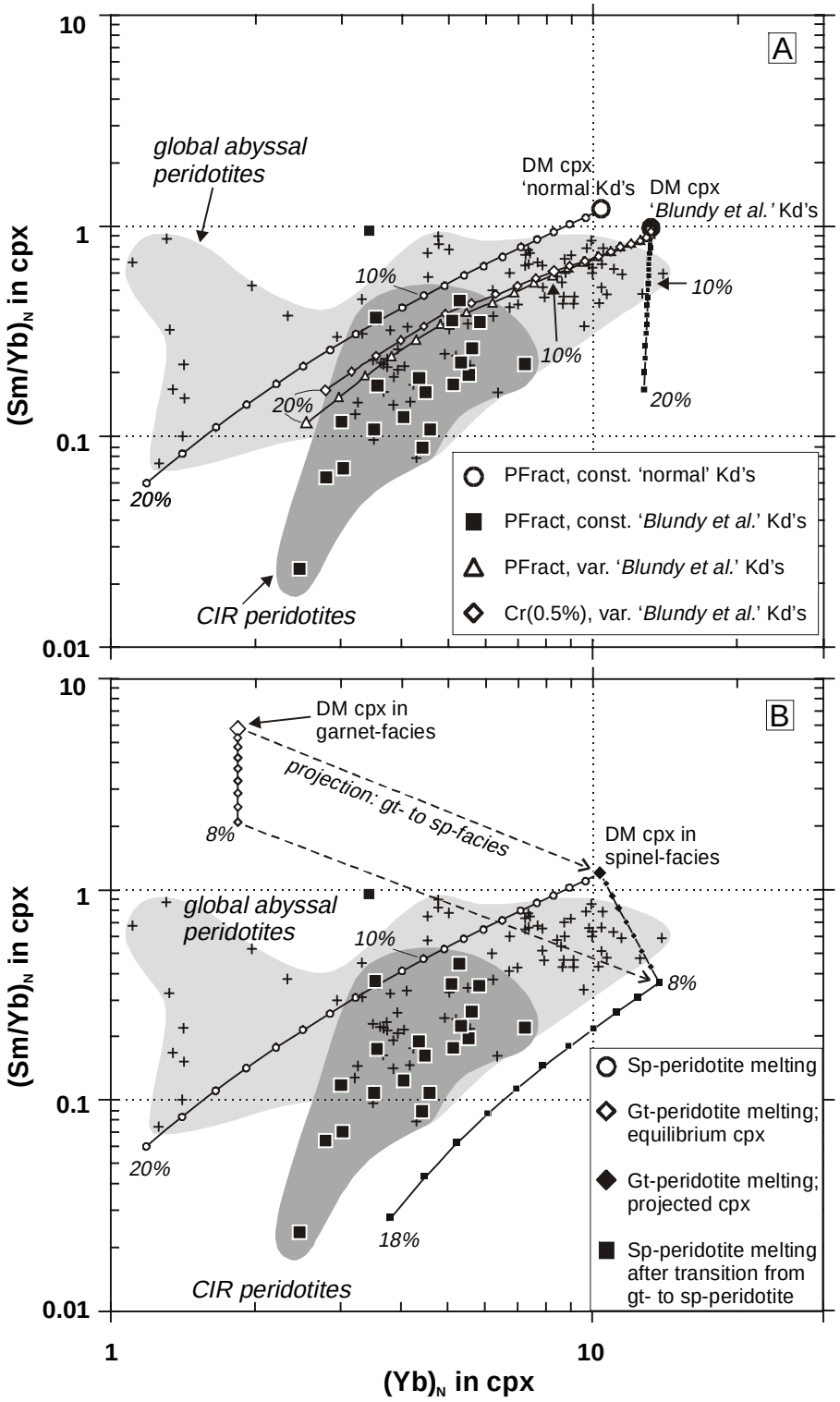

Fig. 7: (a) Yb_N vs. $(Sm/Yb)_N$ in CIR cpx (closed squares) and other abyssal peridotites (AP) (crosses). Curves represent perfect fractional (PFract) and critical (Cr) melting models of a sp-peridotite source. Only difference between these models is $Kd^{cpx/l}$, as shown in Fig 6. None of the sp-peridotite melting models can explain the low $(Sm/Yb)_N$ ratios at high Yb concentrations in many cpx. AP data from JOHNSON ET AL. (1990), JOHNSON and DICK (1992), DICK and NATLAND (1996), ROSS and ELTHON (1997). **(b)** Results of initial gt-peridotite melting followed by melting in the stability field of sp-peridotite. The strong fractionation of the MREE from the HREE observed in many AP cpx can only be explained by few percent of initial melting in the gt-stability field prior to melting in the sp-field. More discussion in the text.

Mg_2SiO_4 (Ol) + $Ca_{0.75}Mg_{2.25}Al_2Si_3O_{12}$ (Gt) =

$2.5MgSiO_3$ (Opx) + $MgAl_2O_4$ (Sp) + $0.75CaMgSi_2O_6$ (Cpx)

The projection method reveals that the initial modal compositions for the garnet and spinel peridotite stability field as given by (JOHNSON ET AL., 1990) do not yield an identical starting composition. This is of particular importance, because the initial modal cpx is the most influential and hence crucial parameter of any peridotite melting calculation. Therefore, for modeling melting in the garnet peridotite field we used the initial spinel peridotite modes JOHNSON ET AL. (1990), which were then recalculated for a spinel-free, garnet-bearing assemblage. All initial modeling parameters are given in Table 7.

In Fig. 7b four fractional melting trajectories are shown. The thin line is the result of spinel-facies melting using 'normal' incompatible partition coefficients discussed in the previous section. The garnet peridotite melting trajectory is shown twice: once for actual cpx compositions in equilibrium with garnet and once for spinel-peridotite projected cpx compositions. This means that cpx in the DMM source has an entirely different REE composition depending on whether it coexists with garnet or spinel. In the stability field of garnet peridotite, cpx will have a low Yb concentration and a high Sm/Yb value, because Yb is compatible in the coexisting garnet. Melt extraction will lead to constant Yb concentrations and rapidly decreasing $(Sm/Yb)_N$ in the residual cpx. The garnet stability field melting trajectory that is projected to a garnet-free spinel peridotite assemblage is shifted towards slightly higher Yb concentrations and decreasing Sm/Yb value. A thin dashed line connects a DMM source cpx of real garnet field and projected garnet-free compositions. The latter is identical to a DMM cpx in a spinel peridotite starting material (Fig. 7a). Clearly, $(Sm/Yb)_N$ in cpx decreases more rapidly by garnet field melting than by spinel field melting. Initial garnet field melting followed by spinel field melting is also shown in this diagram, placing an upper boundary on the extent of garnet melting necessary to explain the data. This two-step melting curve can account for any of the observed low $(Sm/Yb)_N$ and the relatively high Yb concentrations for the CIR samples. In contrast to spinel field melting using the partition coefficients from BLUNDY ET AL. (1998), highly fractionated samples can be explained by reasonable degrees of melting. Major element compositions of some of the very fractionated samples also support moderate degrees of melting.

For the cpx REE patterns that could not be reproduced by melting in the spinel field alone, a combination of initial melting in the garnet stability field followed additional melting in the spinel stability field. The Argo FZ samples (ANTP126) can be matched by such a model. It allows several proportions of melting in the garnet field and subsequent melting in the spinel field. However, a minimum of 3% garnet field fractional melting is required to produce the necessary fractionation between MREE and HREE. After this another 9-11% melting in the spinel field is needed to match the measured Argo FZ cpx data. The measured La and Ce concentrations, however, are still too high to be explained by melting and require an additional process.

All *Group 2* samples (CIR axis 12°S, MCFZ) require some melt extraction in the garnet peridotite stability field. Five samples (ANTP89-1, ANTP89-2, ANTP89-5, ANTP89-8 and ANTP89-15) from MCFZ have nearly identical convex-upward LREE-depleted patterns, but cannot be explained by fractional melting in the spinel field alone. Small degrees of melting (3-4%) in the presence of residual garnet, prior to another 6-8% melting in the spinel field would perfectly match the measurements. The Sm/Yb value of sample ANTP84-11 can only be approached after very high degrees of melting (~6%) in the garnet peridotite stability field and another ~12% melting after the ascent in the spinel peridotite stability field. Considering that pure fractional melting is an unrealistic endmember model that calculates the lowest possible cpx $(Sm/Yb)_N$ for a given degree of melting, the total amount of melting for this ultra-depleted sample is probably much higher. It is very difficult to match this result with the relatively low spinel Cr# of 0.34 for this sample (Table 2), which suggests only a moderate extent of partial melting. Samples ANTP87-5, ANTP87-9, and ANTP89-17 are also extremely depleted, with $(Sm/Yb)_N$ <0.1. These values also require high (~6%) of melting in the garnet peridotite stability field followed by ~10% of melting in the spinel stability field. The hump-shaped REE pattern of CIRCE93-7 (Fig. 4d) cannot at all be explained by melting. Samples CIRCE93-2 and CIRCE93-4 could be the product of 13% critical melting of spinel peridotite with residual porosities of 0.5%. The model predicts slightly too high MREE concentrations, suggesting that minimal amounts of garnet melting could have occurred prior to ascent into the spinel peridotite stability field.

In summary, roughly half of the CIR samples cannot be explained by partial melting in the stability field of spinel peridotite but require residual garnet in the source. Up to eight percent of melting in the stability field of garnet prior to melting under spinel peridotite-facies conditions are necessary to reach the strong MREE from HREE fractionation

observed in samples from Argo FZ (ANTP126), Marie Celeste FZ (ANTP84, ANTP87, ANTP89), and possibly CIR 12°S (CIRCE93).

2.5.2. Coupling and decoupling

Until recently, the decoupling between major and trace elements in residual peridotites was considered a major stumbling block for the understanding of melting and melt migration in the oceanic mantle (KELEMEN ET AL., 1997). However, major element indicators of melting, such as Cr# in spinel and Al_2O_3 content in cpx correlate well with HREE concentrations in cpx of all global abyssal peridotites (HELLEBRAND ET AL., submitted). The actual decoupling is confined to the highly incompatible trace elements, which are very poorly or not at all correlated with spinel Cr#. Because of this decoupling, highly incompatible trace elements, such as the LREE, strontium and zirconium cannot be used for estimating the extent of melting. With restrictions, however, they serve as a powerful tool to identify possible late-stage, or, post-melting processes, such as advective melt percolation, melt entrapment, or veining.

2.5.2.1. Subsolidus veining

Subsolidus veining is probably the least cryptic modification of a residual peridotite. Thin magmatic veinlets that crosscut residual peridotites are widespread and have a dramatic influence on the chemical composition of the phases in a (small) reaction zone surrounding the vein (CANNAT ET AL., 1997; NIIDA, 1997; HELLEBRAND ET AL., 1999). Crosscutting gabbroic dikelets are very common in the exposed MARK area mantle that was drilled during ODP Leg 153. One meter of core contains on average four magmatic veinlets that are mainly less than 1 cm thick (CANNAT ET AL., 1997). The width of the reaction zone depends on the thickness of the vein. Thick veins produce a chemical gradient that can be easily recognized in the host peridotite. Despite lack of petrographic evidence for subsolidus melt injection in the selected residual CIR samples, a contact zone is probably present in sample ANTP89-2. Here, one spinel grain with an anomalously high Cr# of 0.49 is present at the edge of the sample. Two other spinels less than 4 mm away from this anomalous spinel have Cr# of 0.26. We assume that the sample edge must have been the plane of a very thin crosscutting magmatic veinlet, which produced a reaction zone that is smaller than 4 mm. Because of the intense alteration in this sample, direct

evidence for this hypothesis is not available. Observations on other vein-bearing peridotites from the CIR, however, show that the spinel Cr# strongly increases in a small reaction zone. For five vein-bearing peridotite samples from different locations we obtained detailed major and trace element profiles across the vein phases, the reaction zone and the non-modified host peridotite. The results of this study, and a quantitative model for the interpretation of conditions under which vein injection took place, will be presented elsewhere (Hellebrand et al, in prep.).

2.5.2.2. Melt entrapment

A second post-melting modification can be produced by melt entrapment. ELTHON (1992) noted that cpx of many abyssal peridotites have sodium concentrations that are too high to be residues of fractional melting. He suggested that as melting ceases, residual peridotites are refertilized by a melt that crystallizes and equilibrates with the host peridotite. According to his modeling, the addition of up to 10% depleted basaltic liquid is needed to refertilize a peridotite that previously experienced melt extraction.

In the following, we try to assess the influence of melt entrapment on the cpx REE composition, irrespective of what the textural implications of such large amounts of trapped melt are. The hump-shaped REE pattern of sample CIRCE93-7 will serve as an extreme case in which the REE concentrations are dominated by small amounts of trapped melt. As shown in the previous section, the hump-shaped REE pattern of this sample cannot be generated by partial melting, since melt extraction will lead to a strong LREE depletion relative to the HREE. In particular, fractional melting in the stability field of garnet peridotite will produce a residue with very low LREE/HREE and low MREE/HREE values and therefore partial melting in the presence of garnet not suited to explain hump-shaped REE patterns in residual clinopyroxenes, as suggested by JOHNSON ET AL. (1990). The textures of sample CIRCE93-7 suggest that melt extraction was incomplete and led to precipitation of irregular cpx films on olivine-olivine and olivine-opx grain boundaries. Coarse clinopyroxenes were not observed in this sample.

Quantitative refertilization models require information about the composition of the refertilizing melt, the proportions of the phases that crystallize from it, and the modal and chemical composition of the peridotite before refertilization. The procedure of these calculations is presented in Appendix B.

TABLE 8. Melt entrapment model: input parameters

	Initial cpx [a]	Melt [b]		Initial modes	
				Depleted	Fertile
La	2.2E-04	0.010			
Ce	9.2E-03	0.19	**ol**	0.85	0.65
Nd	0.235	1.7	**opx**	0.139	0.25
Zr	0.118	1.4	**cpx**	0.001	0.09
Sm	1.01	4.3	**sp**	0.01	0.01
Eu	1.80	5.9			
Ti	2.3	7.4			
Dy	2.8	7.3			
Er	2.8	7.5			
Yb	2.8	7.5			

[a] Calculated residual cpx of 13% critical melting with 0.5% residual melt porosity
[b] Calculated instantaneous melt composition of
12% critical melting with 0.5% residual melt porosity

Intuitively, we expect that a refractory peridotite with very low modal cpx and a (L)REE-depleted cpx composition will respond more dramatically to refertilization, than a fertile cpx-rich lherzolite. This is illustrated by Fig. 8, where $(Sm/Yb)_N$ and $(Ce/Yb)_N$ in cpx are plotted versus Yb_N in cpx for two different refertilization models. These models use different peridotite starting compositions: a 'depleted' harzburgite with 0.1% modal cpx and a 'fertile' lherzolite with 9% modal cpx. For simplicity, both starting modes have identical initial cpx REE concentrations, calculated by 13% critical melting with 0.5% residual melt porosity in the spinel stability field using normal constant partition coefficients and conditions listed in Table 8. The refertilizing melt for both models is a refractory melt, derived from a slightly less depleted peridotite. Its composition represents an instantaneous melt formed at 12% critical melting with 0.5% residual melt porosity (Table 8). After entrapment this melt crystallizes 70% cpx and 30% olivine (ELTHON, 1992), after which the newly formed phases equilibrate with the host rock.

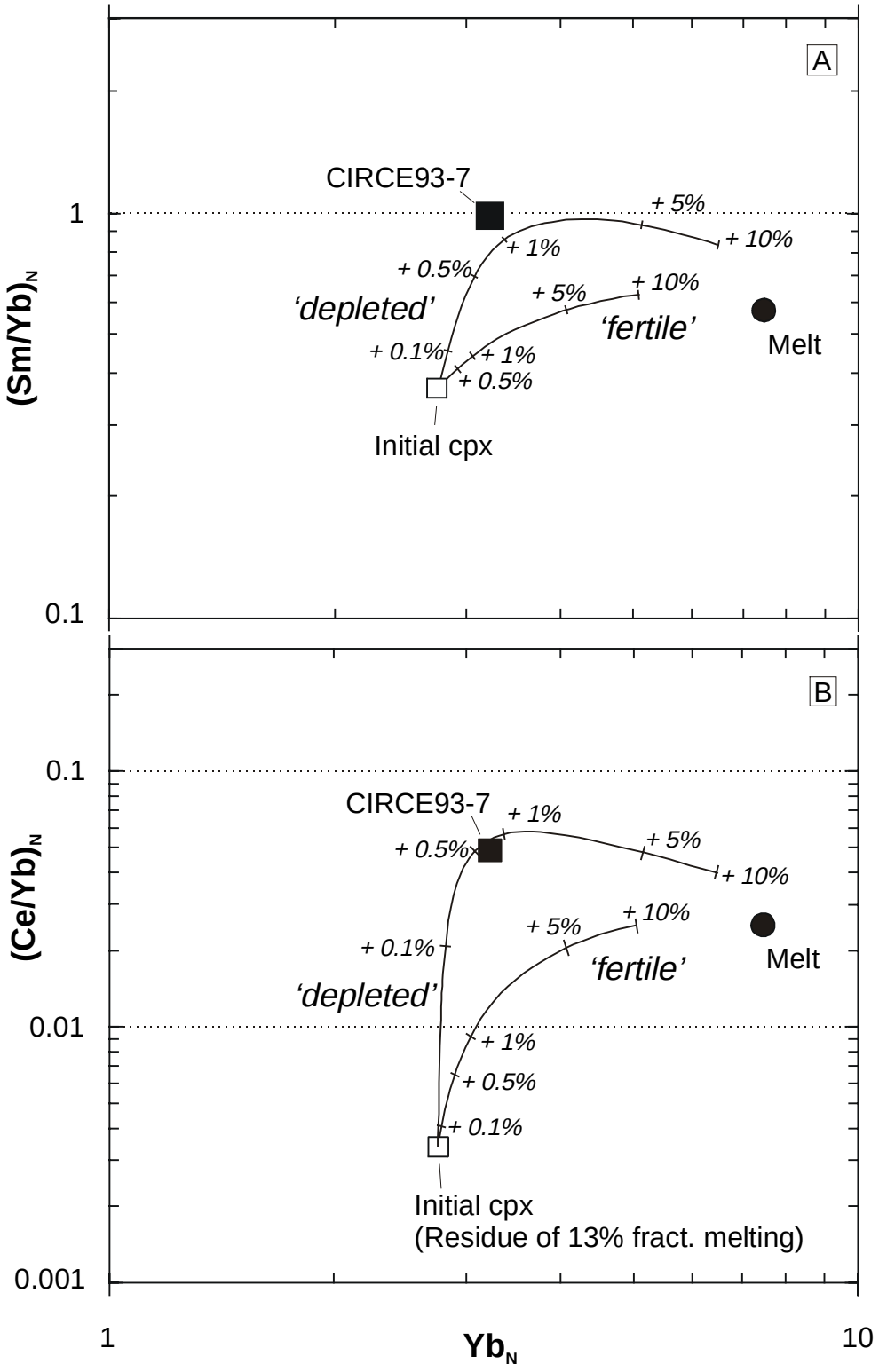

Fig. 8: Results of simple melt entrapment calculations. Mixing and reequilibration of a modally depleted and fertile residual peridotite with a depleted melt. Starting cpx composition for both rocks is identical. (**a**) $(Sm/Yb)_N$ and (**b**) $(Ce/Yb)_N$ versus Yb_N. Refertilization can lead to chondritic $(Sm/Yb)_N$ values in cpx, even if $(Sm/Yb)_N$ in the entrapped melt is subchondritic. More discussion in the text.

Four important results can be seen immediately from this calculation: (1) The modally depleted harzburgite is strongly modified by very small amounts of refertilizing melt, whereas the lherzolite responds less dramatically to small amounts of melt added. This is because the REE budget of the lherzolite is buffered by the high initial cpx mode. (2) The LREE concentration increases much faster than the MREE or even HREE. This is mainly due to the negligable LREE content in the residue before melt entrapment. Large (> 1%) amounts of melt are needed to increase the Yb content significantly for both depleted and fertile starting compositions. (3) Refertilization with a melt that has no hump-shaped REE pattern ($(Sm/Yb)_N<1$) can produce a clinopyroxene that has a significantly higher $(Sm/Yb)_N$ than the entrapped melt, even at very low amounts of liquid added to the residue. The reason for this non-intuitive behavior is the important contribution of residual opx to the bulk distribution coefficient. Because of the very high modal abundance of opx relative to cpx in the modally depleted starting material, the largest absolute fraction of the entrapped HREEs will be hosted by opx. Only after modal cpx has exceeded a few percent the $(Sm/Yb)_N$ in the cpx start to decrease. (4) Minor amounts of melt added to the residue will produce a dramatic increase of the $(Sm/Yb)_N$ ratio, without modifying the Yb concentration. This could easily obscure the types of garnet stability field melting signature discussed in the previous section.

Thus, interstitial melts must be extracted very efficiently, at least from those peridotites that have cpx with $(Sm/Yb)_N$ too low to be explained by spinel peridotite melting. It also means that plagioclase-free peridotites with large amounts of interstitial (melt-derived) cpx are not residues senso stricto, although they may geochemically resemble melting residues. The textures of the 'residual' Vema FZ peridotites, (coarse magmatically twinned cpx in sample ANTP134-3) suggest that they are hybrids of an even more depleted residue and an incompletely extracted or refertilizing melt. Two puzzling aspects have to be discussed in further detail: (1) the composition of this melt and (2) the uniform composition of the Vema FZ samples. If we estimate that the amount of entrapped melt is roughly 0.5%, than it must be strongly LREE-depleted, as the cpx of the Vema FZ samples themselves are LREE-depleted (Fig. 4). In contrast, the relatively high sodium concentrations (Na_2O ~0.6 wt.%) suggest a non-depleted composition, which is either a low-degree partial melt or a pooled melt. A melt that is in equilibrium with this cpx has around 2 wt.% Na_2O. This is clearly contradictory, and it suggests that kinetics may play a significant role in the generation of abyssal peridotite mineral compositions. Recent diffusion experiments (VAN ORMAN ET AL., 1999) have shown that LREE diffusivities are more than one magnitude lower than HREE

diffusivities. Sodium on the other hand is one of the fastest diffusing elements. It may therefore be possible that disequilibrium melt transport can lead to a rapid increase in sodium with (near-) equilibrium values for Na_2O in cpx, without affecting its (L)REE content.

The second issue to address is the uniform composition of the Vema FZ peridotites (ANTP134 samples). This implies that identical amounts of melt were added and equilibrated with a more or less identical melting residue or that the dredged samples are spatially related and outcrop-scale post-melting equilibrium prevailed. The presence of (interconnected) melt may have sped up the equilibration process but without spatial information this issue cannot be resolved at present.

It remains difficult to infer whether very small amounts of melt are trapped in chemically buffered peridotites with more than ~3% modal cpx, especially if these are recrystallized and direct textural information is lost. It is further important to note that melt entrapment does not necessarily lead to plagioclase formation. The chemical 'visibility' of such a melt entrapment strongly depends on the composition of the infiltrating melt and on the modal composition of the residual peridotite.

2.5.2.3. Chromatographic fractionation

As observed in orogenic lherzolite bodies and mantle sections of ophiolites, simple melt entrapment is not the only process that can modify the composition of a previously depleted peridotite that is devoid of magmatic veins that crosscut the peridotite under subsolidus conditions. Reactive porous flow near a melt transport channel can produce dm- to m-scale zonations and large chemical variations in the melt-infiltrated peridotite (BODINIER ET AL., 1990; SUHR, 1999). High LREE to HREE ratios are observed at a relatively large distance to such channels. These enrichments in highly incompatible trace elements are attributed to chromatographic fractionation (NAVON and STOLPER, 1987). Spoon- or S-shaped REE patterns describing moderate LREE enrichment, are also associated with advective melt transport (GODARD ET AL., 2000). Our data suggest that such a process has left its fingerprint in some of the CIR peridotites. Fig. 4 shows that six samples have cpx with spoon-shaped REE patterns. Two cpx-poor samples from MCFZ (ANTP87-5, ANTP89-17) show relative enrichments of La and Ce, the other samples

(31GTV, 74GTV, CIRCE93-4, ANTP89-8) are only slightly enriched in La. Melting or refertilization calculations fail to explain such patterns, suggesting that chromatographic fractionation may have played a role. Unfortunately, spatial information between individual samples is crucial and detailed geochemical traverses are needed to properly address this problem. Dredged abyssal peridotite are far from ideal for such purposes, but valuable to indicate the presence, extent and distribution of reactive melt migration and as a measure of 'ground truth' for the inferences derived from ophiolites and alpine lherzolites.

2.5.3. Small scale variations

One of the most well-known facts of geochemistry is that the Earth's mantle is isotopically heterogeneous (e.g. SCHILLING, 1975; SCHILLING, 1985; HOFMANN, 1997). The scales at which this heterogeneity occurs within the mantle, however, are still a matter of debate. Direct information from oceanic mantle rocks is scarce. Medium-scale (within-dredge) chemical heterogeneity in the 'residual' oceanic mantle has not been given much attention in the literature. Almost all discussions concerned with the origin of abyssal peridotites were restricted to global and regional trends based on local averages, hereby eliminating variations in modal and chemical compositions. Local variations in mineral chemistry occur within a single dredge haul (MICHAEL and BONATTI, 1985), which the authors partly attributed to subsolidus reequilibration. DICK ET AL. (1984) also mentioned local heterogeneities, especially for the modal composition, but did not address local chemical variations and they focused their attention on dredge averages.

In order to address this issue, we divided our sample set into a chemically homogeneous *Group 1* and a *Group 2* with large chemical heterogeneity on a 'dredge scale'. Some of *Group 2* samples are heterogeneous on thin section scale, as shown by strongly varying spinel Cr# (Fig.2). In order to compare local compositional variation of the CIR samples to other peridotite occurrences, we selected all dredge hauls for which major and trace element mineral data on three or more samples are available. This yields two dredge hauls from the American Antarctic Ridge (Bullard FZ and Vulcan FZ) and two from the South-west Indian Ridge (Bouvet FZ and Islas Orcadas FZ) (JOHNSON ET AL., 1990). Further, we selected published Ocean Drilling Program data from Leg 147 at Hess Deep in the Pacific (DICK and NATLAND, 1996) and from Leg 153 in the MARK area (ROSS and ELTHON, 1997), where spatial relationships between individual peridotite samples are known.

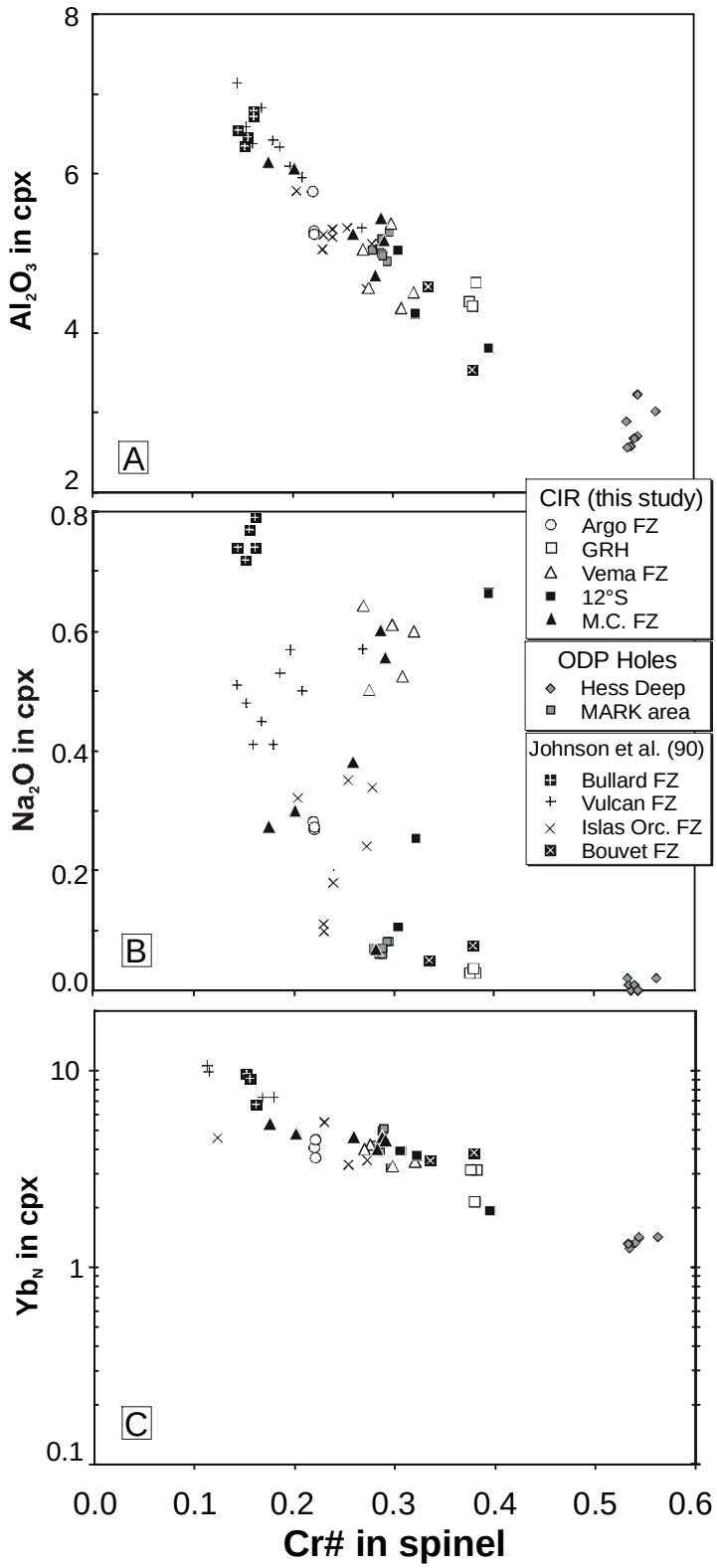

Fig. 9: Local mineral chemical variation in selected global abyssal peridotites. (**a**) Al_2O_3 (wt.%), (**b**) Na_2O (wt.%), and (**c**) Yb_N in cpx vs. Cr# in associated spinel.

Figure 8 shows aluminum, sodium and ytterbium concentrations in cpx versus the Cr# of the associated spinel for all selected samples. Drilled residual peridotites have almost constant major and trace element compositions throughout the boreholes. Four out of nine dredge hauls are compositionally relatively homogeneous, although there is more variation than in the boreholes. Three dredges (Vulcan FZ, Islas Orcadas FZ, Vema FZ) show substantial chemical variation, especially for sodium. The peridotites from CIR 12°S and Marie Celeste FZ are very heterogeneous.

The causes for local heterogeneities remain largely enigmatic. However, our observations may serve as a guide for future studies with respect to some aspects. (1) Inefficient melt extraction, as seen in the Vema FZ harzburgites, does not necessarily lead to heterogeneity. (2) Reactive porous melt flow in and near dunitic channels can produce large chemical gradients and modal heterogeneity on an outcrop scale, as is observed in the mantle sections of ophiolites (KELEMEN ET AL., 1992; SUHR, 1999). The extremely depleted modal and chemical composition of Hess Deep harzburgites can also be attributed to this process (DICK and NATLAND, 1996). In contrast to the very heterogeneous CIR 12°S peridotites, which bear evidence for melt-rock reaction, Hess Deep peridotites are relatively homogeneous. Possibly, the melt supply beneath the fast spreading EPR is more continuous than beneath the intermediate spreading CIR.

2.6. Conclusions

(1) Clinopyroxenes in plagioclase- and vein-free abyssal peridotites from the Central Indian Ridge are generally more depleted in incompatible trace element than those in similar peridotites from the slower spreading Southwest Indian and American Antarctic Ridges. This implies that there is indeed some dependence of degree of melting on spreading rate (NIU and HEKINIAN, 1997).

(2) Although the general features of the cpx REE patterns can be modeled by fractional melting in the spinel stability field, roughly half of the CIR melting residues requires initial melting in the presence of garnet. Garnet in the melting region is necessary to explain the low MREE to HREE ratios. Recent published cpx partition coefficients (BLUNDY ET AL., 1998), which suggest that HREE are compatible in cpx at high pressures, are believed to mimic the garnet-signature of many MORB glasses.

Fractional and critical melting models that apply these new $Kd^{cpx/l}$ fail to explain the low Sm/Yb values in cpx of many CIR and other abyssal peridotites.

(3) Textures of the Central Indian Ridge peridotites indicate that efficiency of melt extraction is variable. At olivine-olivine and olivine-opx grain boundaries of some samples, melt-derived interstitial cpx crystallized. The cpx trace element signature of modally and chemically depleted melting residues is highly susceptible to minor (<1%) amounts of trapped melt. However, 'trapped melt' is not reflected automatically by the mineral chemistry, it largely depends on the modal cpx content that was present before melt entrapment and the chemistry of the refertilizing melt. 'Hump-shaped' REE patterns do not reflect melting in the garnet field as asserted by JOHNSON ET AL. (1990). They can be produced by the refertilization with a depleted melt due to the leverage of opx on the bulk distribution coefficient.

(4) The chemical composition of relict mantle phases in the CIR peridotite varies strongly in some dredge hauls and is constant in others. A comparison with the two available oceanic mantle boreholes reveals that the mantle away from crosscutting dikelets has very limited compositional variation. Apparently, parts of the CIR are more heterogeneous on a small to medium scale. In such areas of large local variations, exact spatial information between individual samples can be provided by other recovery methods, such as drilling. These are required to address the causes, extent and scales of heterogeneities in the oceanic mantle, and whether they are preserved or produced by melting or melt migration.

2.7. References

Anders E. and Grevesse N. (1989) Abundances of the elements: meteoric and solar. *Geochim. Cosmochi. Acta* **53**, 197-214.

Asimow P. D. (1999) A model that reconciles major- and trace-element data from abyssal peridotites. *Earth Planet. Sci. Lett.* **169**, 303-319.

Aumento F. and Loubat H. (1971) The Mid-Atlantic Ridge near 45°N. Serpentinized ultramafic intrusions. *Can. J. Earth Sci.* **8**, 631-663.

Baxter A. N., Upton B., and White W. M. (1985) Petrology and geochemistry of Rodrigues Island, Indian Ocean. *Contrib. Mineral. Petrol.* **89**, 90-101.

Beattie P. (1993a) The generation of uranium series disequilibria by partial melting of spinel peridotite; constraints from partitioning studies. *Earth Planet. Sci. Lett.* **117**, 379-391.

Beattie P. (1993b) Uranium-thorium disequilibria and partitioning on melting of garnet peridotite. *Nature* **363**, 63-65.

Blundy J., Robinson J. A. C., and Wood B. (1998) Heavy REE are compatible in clinopyroxene on the spinel lherzolite solidus. *Earth Planet. Sci. Lett.* **160**, 493-504.

Bodinier J. L., Vasseur G., Vernieres J., Dupuy C., and Fabries J. (1990) Mechanisms of mantle metasomatism: geochemical evidence from the Lherz orogenic peridotite. *J. Petrol.* **31**, 597-628.

Bottinga Y. and Allègre C. J. (1978) Partial melting under spreading ridges. *Philos. Trans. R. Soc. London* **A288**, 501-525.

Bourdon B., Langmuir C. H., Elliot T., and Zindler A. (1996) Constraints on mantle melting at mid-ocean ridges from global ^{238}U-^{230}Th disequilibrium data. *Nature* **384**, 231-235.

Briais A. (1995) Structural analysis of the segmentation of the Central Indian Ridge between 20°30'S and 25°30'S (Rodriguez Triple Junction). *Mar. Geophys. Res.* **17**, 431-467.

Cannat M. (1993) Emplacement of mantle rocks in the seafloor at mid-ocean ridges. *J. Geophys. Res.* **98**, 4163-4172.

Cannat M., Chatin F., Whitechurch H., and Ceuleneer G. (1997) Gabbroic rocks trapped in the upper mantle at the Mid-Atlantic Ridge. *Proc. ODP, Sci. Res.* **153**, 243-264.

Debayle E. and Leveque J. J. (1997) Upper mantle heterogeneities in the Indian Ocean from waveform inversions. *Geophys. Res. Lett.* **24**, 245-248.

DeMets C., Gordon R. G., Argus D. F., and Stein S. (1990) Current plate motions. *Geophys. J. Int.* **101**, 425-478.

Dick H. J. B. (1989) Abyssal peridotites, very slow spreading ridges and ocean ridge magmatism. *Geol. Soc. Spec. Publ.* **42**, 71-105.

Dick H. J. B. and Bullen T. (1984) Chromian spinel as a petrogenetic indicator in abyssal and alpine-type peridotites and spatially associated lavas. *Contrib. Mineral. Petrol.* **86**, 54-76.

Dick H. J. B., Fisher R. L., and Bryan W. B. (1984) Mineralogic variability of the uppermost mantle along mid-ocean ridges. *Earth Planet . Sci. Letters* **69**, 88-106.

Dick H. J. B. and Natland J. H. (1996) Late-stage melt evolution and transport in the shallow mantle beneath the East Pacific Rise. *Proc. ODP, Sci. Res.* **147**, 103-134.

Dupré B. and Allègre C. J. (1983) Pb-Sr isotope variation in Indian Ocean basalts and mixing phenomena. *Nature* **303**, 142-146.

Dyment J. (1998) Evolution of the Carlsberg Ridge between 60 and 45 Ma: Ridge propagation, spreading asymmetry, and the Deccan-Reunion hotspot. *J. Geophys. Res.* **103**, 24067-24084.

Elthon D. (1992) Chemical trends in abyssal peridotites; refertilization of depleted suboceanic mantle. *J. Geophys. Res.* **97**, 9015-9025.

Engel C. G. and Fisher R. L. (1975) Granitic to ultramafic rock complexes of the Indian Ocean ridge system, western Indian Ocean. *Geol. Soc. Am. Bull.* **24**, 1553-1578.

Gaetani G. A. and Grove T. L. (1995) Partitioning of rare earth elements between clinopyroxene and silicate melt: crystal-chemical controls. *Geochim. Cosmochim. Acta* **59**, 1951-1962.

Gast P. W. (1968) Trace element fractionation and the origin of tholeiitic and alkalic magma types. *Geochim. Cosmochi. Acta* **32**, 1057-1086.

Godard M., Jousselin D., and Bodinier J. L. (2000) Relationships between geochemistry and structure beneath a palaeo-spreading centre: a study of the mantle section in the Oman ophiolite. *Earth Planet. Sci. Lett.* **180**, 133-148.

Green D. H. and Ringwood A. E. (1967) The genesis of basaltic magmas. *Contrib. Mineral. Petrol.* **15**, 103-190.

Green D. H. and Ringwood A. E. (1970) Mineralogy of peridotitic compositions under upper mantle conditions. *Phys. Earth Planet. Inter.* **3**, 359-371.

Hamlyn P., R. and Bonatti E. (1980) Petrology of mantle-derived ultramafics from the Owen Fracture Zone, Northwest Indian Ocean: implications for the nature of the oceanic upper mantle. *Earth Planet. Sci. Lett.* **48**, 65-79.

Hart S. R. and Dunn T. (1993) Experimental cpx/melt partitioning of 24 elements. *Contrib. Mineral. Petrol.* **113**, 1-18.

Hauri E. and Hart S. (1995) Corrections to "Constraints on melt migration from mantle plumes; a trace element study of peridotite xenoliths from Savai'i, western Samoa". *J. Geophys. Res.* **100**, 2003.

Hellebrand E., Snow J. E., Dick H. J. B., Devey C. W., and Hofmann A. W. (1999) Reactive crack flow in the oceanic mantle: an ion probe study on cpx from vein-bearing abyssal peridotites. *Ofioliti* **24**, 106-107.

Hellebrand E., Snow J. E., Dick H. J. B., and Hofmann A. W. (submitted) Major and trace element coupling in global mid-ocean ridge melting residues. *Nature*.

Hofmann A. W. (1997) Mantle geochemistry: the message from oceanic volcanism. *Nature* **385**, 219-229.

Jochum K. P., Dingwell D. B., Rocholl A., Stoll B., Hofmann A. W., and others a. (2000) The preparation and preliminary characterisation of eight geological MPI-DING standard reference glasses for in-situ microanalysis. *Geost. Newslett.* **24**, 87-133.

Johnson K. T. M. (1998) Experimental determination of partition coefficients for rare earth and high-field-strength elements between clinopyroxene, garnet, and basaltic melt at high pressures. *Contrib. Mineral. Petrol.* **133**, 60-68.

Johnson K. T. M. and Dick H. J. B. (1992) Open system melting and temporal and spatial variation of peridotite and basalt at the Atlantis II fracture zone. *J. Geophys. Res.* **97**, 9219-9241.

Johnson K. T. M., Dick H. J. B., and Shimizu N. (1990) Melting in the oceanic upper mantle; an ion microprobe study of diopsides in abyssal peridotites. *J. Geophys. Res.* **95**, 2661-2678.

Kelemen P. B., Dick H. J. B., and Quick J. E. (1992) Formation of harzburgite by pervasive melt/rock reaction in the upper mantle. *Nature* **358**, 635-641.

Kelemen P. B., Hirth G., Shimizu N., Spiegelman M., and Dick H. J. B. (1997) A review of melt migration processes in the adiabatically upwelling mantle beneath oceanic spreading ridges. *Phil. Trans. R. Soc. London* **355**, 283-318.

Kinzler R., J. (1997) Melting of mantle peridotite at pressures approaching the spinel to garnet transition: application to mid-ocean ridge basalt petrogenesis. *J. Geophys. Res.* **102**, 953-874.

Klein E. M. and Langmuir C. H. (1987) Global correlations of ocean ridge basalts with axial depth and crustal thickness. *J. Geophys. Res.* **92**, 8089-8115.

Langmuir C. H., Klein E. M., and Plank T. (1992) Petrologic systematics of mid-ocean ridge basalts: constraints on melt generation beneath ocean ridges. In *Mantle flow and melt generation at mid-ocean ridges*, Vol. 71 (ed. J. Phipps-Morgan, D. K. Blackman, and J. M. Sinton), pp. 183-280. AGU Monograph.

Lundstrom C. C., Gill J., and Williams Q. (2000) A geochemically consistent hypothesis for MORB generation. *Chem. Geol.* **162**, 105-126.

Lundstrom C. C., Gill J., Williams Q., and M. P. (1995) Mantle melting and basalt extraction by equilibrium porous flow. *Science* **270**, 1958-1961.

Maaloe S. (1982) Geochemical aspects of permeability controlled partial melting and fractional crystallization. *Geochim. Cosmochi. Acta* **46**, 43-57.

Mahoney J. J. (1988) Deccan traps. In *Continental Flood Basalts* (ed. J. D. MacDougall), pp. 151-194. Kluwer Academic.

Mahoney J. J., Natland J. H., White W. M., Poreda R., Bloomer S. H., Fisher R. L., and Baxter A. N. (1989) Isotopic and geochemical provinces of the Western Indian Ocean spreading centers. *J. Geophys. Res.* **94**, 4033-4052.

McDougall I. and Chamalaun F. G. (1969) Isotopic dating and geomagnetic polarity studies on volcanic rocks from Mauritius, Indian Ocean. *Geol. Soc. Am. Bull.* **80**, 1419-1442.

McKenzie D. (1984) The generation and compaction of partially molten rock. *J. Petrol.* **25**, 713-765.

McKenzie D. and Bickle M. J. (1988) The volume and composition of melt generated by extension of the lithosphere. *J. Petrol.* **29**, 625-679.

Mercier J. C. and Nicolas A. (1975) Textures and fabrics of upper-mantle peridotites as illustrated by xenoliths from basalts. *J. Petrol.* **16**, 454-487.

Michael P. J. and Bonatti E. (1985) Peridotite composition from the North Atlantic; regional and tectonic variations and implications for partial melting. *Earth Planet. Sci. Lett.* **73**, 91-104.

Morgan W. J. (1978) Rodriguez, Darwin, Amsterdam,..., A second type of hotspot island. *J. Geophys. Res.* **83**, 5355-5360.

Natland J. (1991) Indian Ocean crust. In *Oceanic basalts* (ed. P. A. Floyd), pp. 289-310. Blackie and Son.

Navon O. and Stolper E. (1987) Geochemical consequences of melt percolation: the upper mantle as a chromatographic column. *J. Geol.* **95**, 285-307.

Niida K. (1997) Mineralogy of MARK peridotites: replacement through magma channeling examined from Hole 920D, MARK area. *Proc. ODP, Sci. Res.* **153**, 243-264.

Niu Y. and Hekinian R. (1997) Spreading-rate dependence of the extent of mantle melting beneath ocean ridges. *Nature* **385**, 326-329.

O'Hara M. J. (1985) Importance of the shape of the melting regime during partial melting of the mantle. *Nature* **314**, 58-62.

O'Hara M. J., Richardson S. W., and Wilson G. (1971) Garnet-peridotite stability and occurrence in crust and mantle. *Contrib. Mineral. Petrol.* **32**, 48-68.

Rehkämper M. and Hofmann A. W. (1997) Recycled ocean crust and sediment in Indian Ocean MORB. *Earth Planet. Sci. Lett.* **147**, 93-106.

Ross K. and Elthon D. (1997) Extreme incompatible trace-element depletion of diopside in residual mantle from south of the Kane F.Z. *Proc. ODP, Sci. Res.* **153**, 277-284.

Salters V. J. M. (1996) The generation of mid-ocean ridge basalts from the Hf and Nd isotope perspective. *Earth Planet. Sci. Lett.* **141**, 109-123.

Salters V. J. M. and Hart S. R. (1989) The hafnium paradox and the role of garnet in the source of mid-ocean ridge basalts. *Nature* **342**, 420-422.

Schiano P., Birck J. L., and Allègre C. A. (1997) Osmium-strontium-neodymium-lead isotopic covariations in mid-ocean ridge glasses and the heterogeneity of the upper mantle. *Earth Planet. Sci. Lett.* **150**, 363-379.

Schilling J.-G. (1975) Azores mantle blob: rare earth evidence. *Earth Planet. Sci. Lett.* **25**, 103-115.

Schilling J.-G. (1985) Upper mantle heterogeneities and dynamics. *Nature* **314**, 62-67.

Shaw D. M. (1970) Trace element fractionation during anatexis. *Geochim. Cosmochim. Acta* **34**, 237-243.

Shen Y. and Forsyth D. W. (1995) Geochemical constraint on initial and final depths of melting beneath mid-ocean ridges. *J. Geophys. Res.* **100**, 2211-2237.

Shimizu N., Semet M. P., and Allegre J. C. (1978) Geochemical applications of quantitative ion microprobe analysis. *Geochim. Cosmochim. Acta* **42**, 1321-1334.

Sinton J. (1978) Petrology of (alpine-type) peridotites from Site 395, DSDP Leg 45. *Ini. Rpts. DSDP* **45**, 595-601.

Sobolev A. V. (1996) Melt inclusions in minerals as a source of principle petrological information. *Petrology* **4**, 209-220.

Sobolev A. V. and Shimizu N. (1992) Extremely depleted magmas and oceanic mantle permeability. *Dokl. Akad. Nauk.* **326**, 354-360.

Spiegelman M. and Elliot T. (1993) Consequences of melt transport for uranium series disequilibrium. *Earth Planet. Sci. Lett.* **118**, 1-20.

Suhr G. (1999) Melt migration under oceanic ridges: inferences from reactive transport modelling of upper mantle hosted dunites. *J. Petrol.* **40**, 575-599.

Suhr G., Seck H. A., Shimizu N., Günther D., and Jenner G. (1998) Infiltration of refractory melts into the lowermost oceanic crust: evidence from dunite- and gabbro-hosted clinopyroxenes in he Bay of Islands Ophiolite. *Contrib. Mineral. Petrol.* **131**, 136-154.

Takahashi E. (1986) Melting of a dry peridotite KLB-1 up to 14 GPa: implications on the origin of peridotitic upper mantle. *J. Geophys. Res.* **91**, 9367-9382.

Tartarotti P., Cannat M., and Mevel C. (1995) Gabbroic dikelets in serpentinized peridotites from the Mid-Atlantic Ridge at 23°20'N. In *Mantle and lower crust exposed in oceanic ridges and in ophiolites*, Vol. 6 (ed. R. Vissers and A. Nicolas), pp. 214. Kluwer Academic Publishers.

van Orman J. A., Grove T. L., and Shimizu N. (1999) Diffusive fractionation of REE during mantle melting: experiments and models. *Ofioliti* **24**, 183-184.

van Westrenen W., Blundy J., and Wood B. (1999) Crystal-chemical controls on trace element partitioning between garnet and anhydrous silicate melt. *Am. Mineral.* **84**, 838-847.

Walter M., J. (1998) Melting of garnet peridotite and the origin of komatiite and depleted lithosphere. *J. Petrol.* **39**, 29-60.

Wood B. J. and Blundy J. D. (1997) A predictive model for rare earth element partitioning between clinopyroxene and anhydrous silicate melt. *Contrib. Mineral. Petrol.* **129**, 166-181.

Zinner E. and Crozaz C. (1986) A method for the quantitative measurement of rare earth elements in the ion probe. *Int. J. Mass Spectrom. Ion Proc.* **69**, 17-38.

Chapter 3: Coupled major and trace-element melting indicators in mid-ocean ridge peridotites

Eric Hellebrand, Jonathan E. Snow, Henry J.B. Dick and Albrecht W. Hofmann

Submitted to *Nature*, currently in review

Chapter 3: Coupled major and trace-element melting indicators in mid-ocean ridge peridotites

Rocks from the Earth's uppermost suboceanic mantle, known as abyssal peridotites, have lost variable but generally large amounts of basaltic melts, which form the oceanic crust. This process removes major constituents such as aluminum, as well as mantle-incompatible trace elements such as the rare earth elements (REE), from the peridotite residues. A serious obstacle to a quantitative understanding of this major terrestrial differentiation process has been the perceived general lack of correlation between major and trace element depletions in the peridotites. Here we show that the moderately incompatible heavy REE in abyssal clinopyroxenes are in fact highly correlated with Cr/(Cr+Al) ratios of coexisting spinels. This correlation deteriorates only for the more highly incompatible elements because of late metasomatic and other disturbing processes. Using new electron and ion microprobe data from residual peridotites from the Central Indian ridge, and published data from other abyssal peridotites, we develop a quantitative melting indicator for mantle residues. This should prove useful in relating partial melting to geodynamic variables such as spreading rate and distance from fracture zones.

We studied major and trace elements in minerals in 22 spinel peridotite samples, dredged at seven locations along the intermediate spreading Central Indian Ridge (CIR) and its fracture zones. These samples are petrographically residual, meaning that plagioclase and crosscutting magmatic veins are absent. All samples are harzburgites with the exception of one orthopyroxene-bearing dunite and two lherzolites. Clinopyroxenes (cpx) in CIR peridotites have light rare earth element (LREE) depleted convex-upward REE patterns, and all cover the most depleted range of the global abyssal peridotite spectrum. Whereas the heavy REE (HREE) have a limited range in concentration (~2-10 times chondritic), the LREE abundance in abyssal peridotites ranges almost three orders of magnitude. Selected chemical parameters are shown in Table 1 (*Tables 2-4, Chapter 2*). Complete petrography and mineral chemistry is given in EH, JES and AWH (submitted; *Chapter 2*).

To evaluate the relationships between mineral major and trace elements, we selected all published global abyssal peridotites for which both mineral major element and cpx trace element data are available. This yields three locations on the Southwest Indian (SWIR) and two on the American-Antarctic Ridge (AAR) (JOHNSON and DICK, 1992; JOHNSON ET

AL., 1990). Besides these samples and our own results from the CIR, data from Ocean Drilling Program cores at Hess Deep along the East Pacific Rise (DICK and NATLAND, 1996) and at the MARK area along the northern Mid-Atlantic Ridge (ROSS and ELTHON, 1997) are used, giving a reasonable sampling of global abyssal peridotite occurrences for both major and trace elements.

Table 1: REE concentrations in cpx and spinel Cr-number of CIR peridotites. Trace elements were analyzed in Mainz by SIMS (recently upgraded Cameca IMS-3f), applying energy filtering technique of (SHIMIZU ET AL., 1978). Operating conditions of the Mainz ion microprobe were 12.5 kV accelating potential and 20 nA primary beam current. Standard glass GOR132 was used as an external standard (JOCHUM ET AL., 2000). Average internal precision for the data is better than 10% for HREE, and better than 15% for Eu and Gd. The internal precision for LREE and MREE is concentration-dependent and the error increases with decreasing counting rate. For La and Ce the internal precision varies around ~20-30% for concentrations of 10 ng/g and ~50% for concentrations of 2 ng/g. For Nd and Sm the internal precision is better than 20% at concentrations higher than 100 ng/g and ~40% for concentrations around 20 ng/g. Some samples were also measured at the Cameca IMS-3f ion microprobe at Woods Hole Oceanographic Institution as noted.

Sample	Location	n	Lab	La	Ce	Nd	Sm	Eu	Gd	Dy	Er	Yb	spinel Cr#
CIRCE 93-2	**CIR axis 12°S**	2	MPI	0.014	0.028	0.06	0.12	0.06	0.42	0.75	0.64	0.72	0.32
		2	WHOI			0.12	0.14	0.07		0.64	0.51	0.49	
CIRCE 93-4	**CIR axis 12°S**	2	MPI	0.003	0.013	0.11	0.11	0.05	0.37	0.89	0.63	0.74	0.31
		2	WHOI		0.016	0.13	0.14	0.06		0.85	0.60	0.58	
CIRCE 93-7	**CIR axis 12°S**	2	MPI	0.015	0.095	0.50	0.46	0.21	0.84	0.81	0.44	0.53	0.39
ANTP 126-HD2	**Argo FZ (13°S)**	2	MPI	0.009	0.049	0.04	0.07	0.04	0.25	0.73	0.61	0.66	0.22
ANTP 126-HD5	**Argo FZ (13°S)**	2	MPI	0.010	0.045	0.06	0.07	0.04	0.34	0.73	0.61	0.66	0.22
		2	WHOI		0.041	0.09	0.09	0.05		0.61	0.47	0.57	
ANTP 126-D5	**Argo FZ (13°S)**	2	MPI	0.005	0.020	0.05	0.13	0.06	0.39	0.94	0.71	0.84	0.22
		2	WHOI		0.020	0.08	0.12	0.08		0.76	0.54	0.62	
ANTP 134-HD3	**Vema FZ (8°S)**	2	MPI	0.001	0.014	0.24	0.34	0.14	0.66	1.22	0.84	0.86	0.27
		2	WHOI		0.016	0.25	0.25	0.12		0.86	0.62	0.56	
ANTP 134-HD4	**Vema FZ (8°S)**	3	MPI	0.002	0.036	0.26	0.27	0.13	0.68	1.09	0.73	0.83	0.31
		3	WHOI		0.035	0.31	0.30	0.12		0.78	0.55	0.57	
ANTP 134-HD7	**Vema FZ (8°S)**	4	WHOI		0.025	0.28	0.25	0.12		0.85	0.59	0.56	0.32
ANTP 134-HD8	**Vema FZ (8°S)**	1	MPI	0.002	0.024	0.19	0.19	0.08	0.65	0.93	0.54	0.58	0.30
		3	WHOI		0.033	0.29	0.26	0.14		0.87	0.56	0.62	
ME33/2: 31GTV	**Green Rock Hill (25°S)**	2	MPI	0.002	0.004	0.04	0.06	0.03	0.23	0.61	0.43	0.58	0.38
SO92: 60GTV	**Green Rock Hill (25°S)**	1	MPI	0.005	0.017	0.03	0.09	0.04	0.27	0.60	0.43	0.58	0.38
SO92: 74GTV	**Green Rock Hill (25°S)**	3	MPI	0.002	0.003	0.015	0.05	0.03	0.22	0.47	0.39	0.49	0.38
ANTP 84-HD11	**Marie Celeste FZ (17°S)**	2	MPI	b.d.	0.002	0.005	0.009	0.003	0.06	0.29	0.29	0.38	0.33
ANTP 87-HD5	**Marie Celeste FZ (17°S)**	2	MPI	0.002	0.002	b.d.	0.03	0.02	0.13	0.41	0.46	0.45	0.32
ANTP 87-HD9	**Marie Celeste FZ (17°S)**	2	MPI	0.003	0.006	0.015	0.03	0.03	0.15	0.38	0.34	0.45	0.38
ANTP 89-HD1	**Marie Celeste FZ (17°S)**	2	MPI	0.002	0.013	0.21	0.30	0.13	0.76	1.32	0.83	0.74	0.29
ANTP 89-HD2	**Marie Celeste FZ (17°S)**	2	MPI	0.002	0.006	0.06	0.16	0.10	0.55	1.21	0.84	0.75	0.26
ANTP 89-HD5	**Marie Celeste FZ (17°S)**	3	MPI	0.001	0.005	0.13	0.23	0.13	0.73	1.36	0.94	0.87	0.17
ANTP 89-HD8	**Marie Celeste FZ (17°S)**	2	MPI	0.003	0.006	0.12	0.21	0.13	0.75	1.32	0.97	0.78	0.20
ANTP 89-HD15	**Marie Celeste FZ (17°S)**	4	MPI	0.001	0.008	0.17	0.21	0.13	0.71	1.24	0.92	0.72	0.29
ANTP 89-HD17	**Marie Celeste FZ (17°S)**	4	MPI	0.014	0.013	0.012	0.06	0.04	0.24	0.64	0.57	0.65	0.28
REE detect. lim.			MPI	0.0006	0.0007	0.003	0.004	0.001	0.004	0.002	0.003	0.001	

Lab: MPI = Max-Planck-Institut für Chemie; WHOI = Woods Hole Oceanographic Institution
Values in µg/g
n = number of trace element analyses
REE detection limit = 6 x background

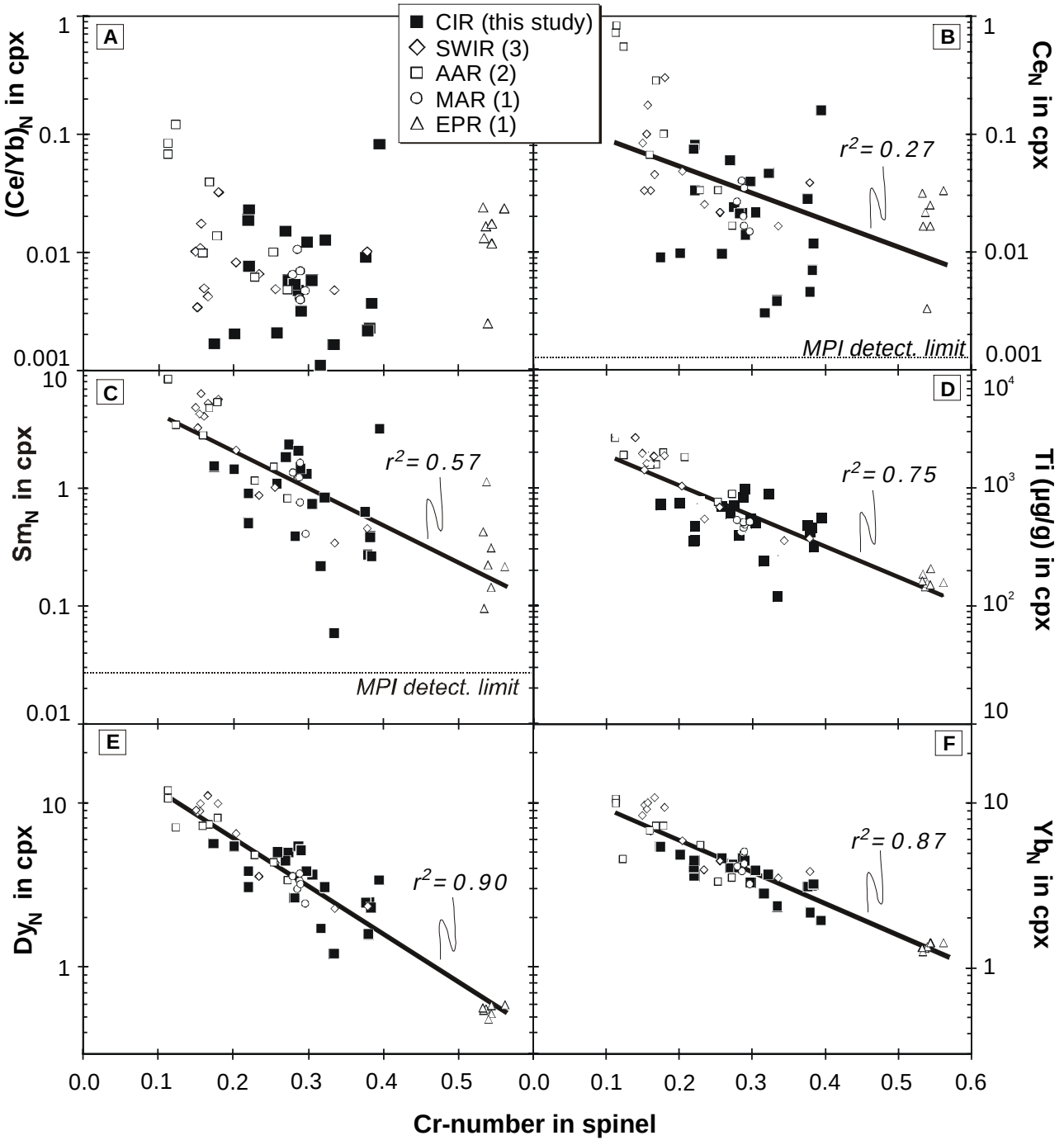

Fig. 1: (**a**) Cr-number in spinel versus cpx $(Ce/Yb)_N$ is predicted to be negatively correlated from theoretical melting models, but is in fact highly decoupled. Cr-number in spinel versus incompatible element concentration in associated clinopyroxene (**b**) Ce_N, (**c**) Sm_N, (**d**) Ti (µg/g), (**e**) Dy_N, and (**f**) Yb_N show progressively tighter correlations expressed by the correlation coefficient (r^2). Numbers in parentheses are number of locations for that portion of mid-ocean ridge. All points are sample averages. Data from (DICK, 1989; DICK and NATLAND, 1996; JOHNSON and DICK, 1992; JOHNSON ET AL., 1990; ROSS and ELTHON, 1997) and from Table 1, chondrite normalizing values from (ANDERS and GREVESSE, 1989).

First we tested which trace elements correlate with major element indicators of partial melting. Commonly, magnesium-number (Mg-number = molar Mg/(Mg+Fe^{2+}) ratio) of silicates, aluminum content of cpx, and chromium-number (Cr-number = molar Cr/(Cr+Al) ratio) in spinel are used for this purpose (DICK ET AL., 1984; MICHAEL and BONATTI, 1985). For illustration, we display spinel Cr-number because of its large compositional range (Fig.1). In the CIR peridotites spinel Cr-number range from 0.17 to 0.57, which is 80% of the global abyssal peridotite spectrum. All spinel titanium contents are below 0.2 wt.% TiO_2, confirming the residual nature of the peridotites (KELEMEN ET AL., 1997; PEARCE ET AL., 2000). Plagioclase-bearing peridotites are non-residual and tend to have higher titanium contents in spinel (DICK, 1989). The presence of plagioclase in highly altered mantle rocks cannot always be documented by petrographic observations alone, and high Ti concentrations in spinel form an additional criterion. Selected major and trace elements in clinopyroxene are plotted versus the Cr-number of the associated spinel (Fig.1). This approach reveals a well-defined correlation between moderately incompatible elements, such as HREE dysprosium, erbium and ytterbium, with spinel Cr-number. All elements were fitted with an exponential line, as the fractional melting equation is an exponential function. Fits were poor for highly incompatible elements and good for less incompatible elements. Only highly incompatible elements, it seems, are highly decoupled from major element mineral chemistry. Cerium is the most incompatible element in this selection and shows the largest variation at a given Cr-number. This is only partly due to lower precision at very low concentrations. Both strong depletion at low Cr-number and large variations towards higher concentrations at higher Cr-number suggest that analytical errors are not the only responsible factor.

Correlation coefficients calculated between trace elements and three major element melting monitors (spinel Cr-number, Al_2O_3 and Mg-number in cpx) confirm the visual impression of Figure 1. This is summarized in Figure 2, where the experimentally determined cpx/melt distribution coefficient ($Kd^{cpx/l}$) of each measured trace element is plotted versus r-squared for the correlation with spinel Cr-number. In each case, r^2 is based on the logarithmic concentration of the trace element. The HREE (Dy, Er, Yb) in residual cpx are correlated with spinel Cr-number (r^2 ~ 0.9) and the aluminum content of cpx (r^2 ~ 0.75, for N=57). Correlation with MREE (Sm, Eu) and Ti are markedly lower but still significant. LREE (La, Ce, and Nd), Sr, and Zr are only weakly or not at all correlated. The Mg-number of residual silicate phases is often regarded as a powerful melting monitor

that increases with increasing degree of melting. However, Figure 2 shows that Mg-number in cpx does not correlate significantly with other melting indicators. This is most likely due to its small absolute range in residual oceanic mantle silicates (between 0.89 and 0.92 for olivine), and is thus largely analytical.

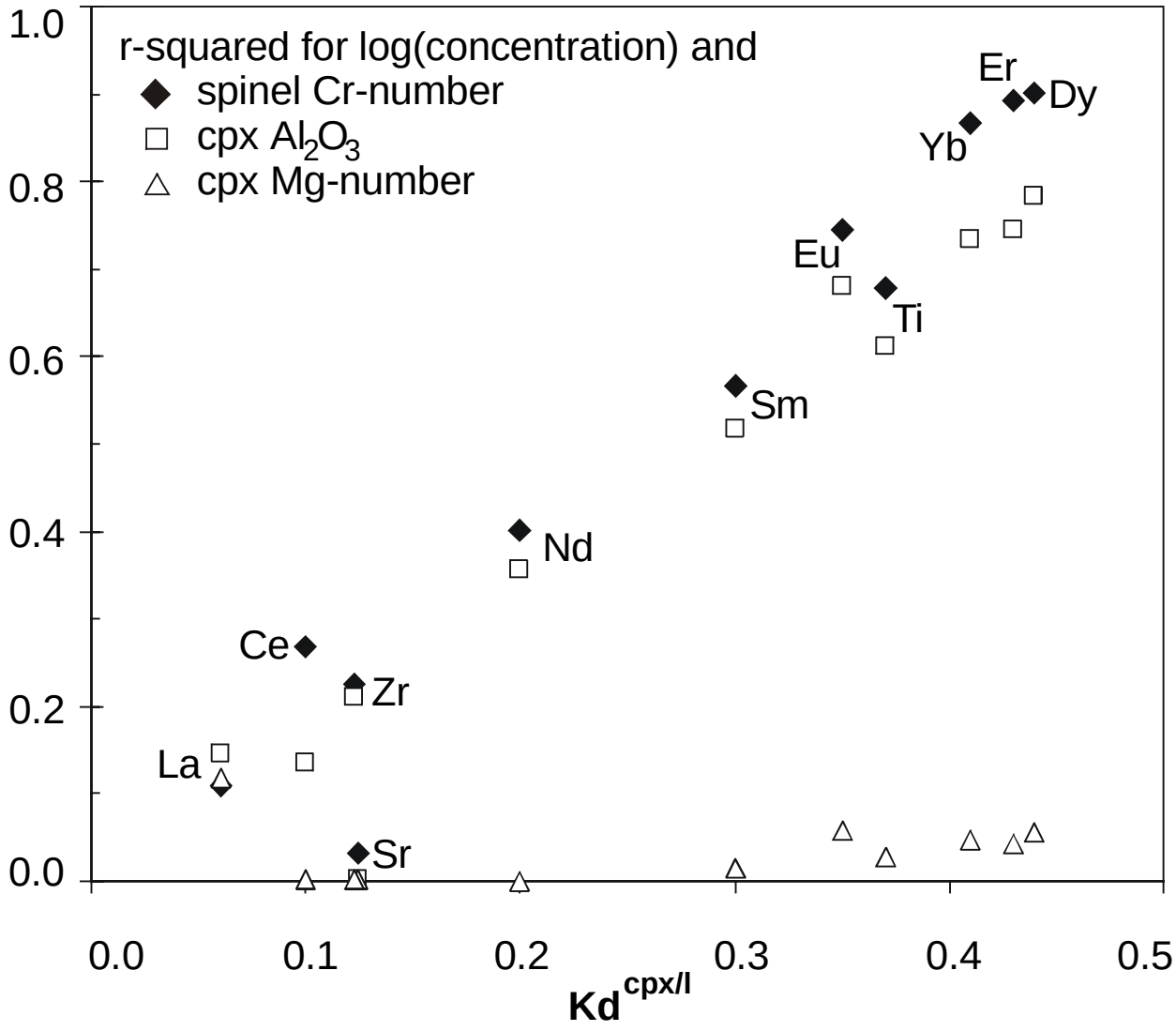

Fig. 2: R-squared between melting indicators (spinel Cr-number, cpx Al_2O_3 content, and cpx Mg-number) and the logarithmic concentration of each trace element versus the cpx/liquid distribution coefficient. All $Kd^{cpx/l}$ by (SUHR ET AL., 1998), except Sr (HART and DUNN, 1993). HREE are well correlated with spinel Cr-number and trace elements become progressively decoupled from spinel Cr-number with increasing incompatibility. There is no significant correlation between cpx Mg-number and any of the trace element concentrations.

The above results show clearly that concentrations of major elements and moderately incompatible trace elements are strongly correlated in abyssal peridotites. The only decoupling is between highly incompatible trace elements and “everything else”. This may be caused by several processes. Entrapment of very small amounts of melt (~1%), or other fluids, and subsequent reequilibration will drastically increase the whole-rock budget of these elements, even if this melt is depleted. Small amounts of melt have only a moderate effect on the more abundant M- to HREE, and correlations will not be severely disturbed. Detailed calculations are presented in EH, JES and AWH (submitted; *Chapter 2*). Another possible cause is reactive porous flow in or near a melt transport channel (KELEMEN ET AL., 1995; SUHR, 1999). This will lead to preferential increase of the most incompatible elements, resulting in a spoon-shaped REE pattern with LREE inflections. At least three cpx REE patterns from the CIR suggest the influence of such a chromatographic fractionation. The implication of this highly incompatible element decoupling is that the LREE in mantle residues are not suitable for quantifying the extent of melting or to estimate the porosity conditions during melting.

In contrast, the good correlation between the major elements and the moderately incompatible trace elements (MREE and HREE) indicates that both are highly useful tracers of partial melting in the mantle. Furthermore, the presence and absence of correlations provides us with a guide on how to interpret abyssal peridotite mineral data. Considering that REE in cpx can be used for quantitative melting modeling (JOHNSON ET AL., 1990), the good correlation of spinel Cr-number with HREE concentration in cpx enables us to develop an empirical equation that describes the extent of melting (F) as a function of spinel Cr-number. As a limiting case, we used pure fractional melting in the spinel stability field to calculate the degree of melting after starting conditions given in (JOHNSON ET AL., 1990), except for a lower initial cpx mode of 0.14. Mineral/melt partition coefficients were taken from (SUHR ET AL., 1998). The measured concentrations of Dy, Er, and Yb each yield a degree of melting, which is plotted versus the Cr-number of the associated spinel (Fig.3). A logarithmic fit on all these calculated points yields a straightforward equation for the degree of melting as a function of the spinel Cr-number: $F = 10 \ln(\text{Cr-number}) + 24$, calibrated for spinel Cr-numbers between 0.10 and 0.60 (thick black line in Figure 3). A similar equation has been derived for mantle rocks in ophiolites (BATANOVA ET AL., 1998).

In order to assess how robust this equation is, we applied different melting models using otherwise identical starting parameters. The average melting curve assuming batch melting (dashed line) and critical melting with 1% residual melt porosity (thin black line) are also shown in Figure 3. The small difference between pure fractional and critical melting with a relatively high melt porosity confirms that the moderately incompatible HREE are not sensitive to changes in melt porosity within the melting column.

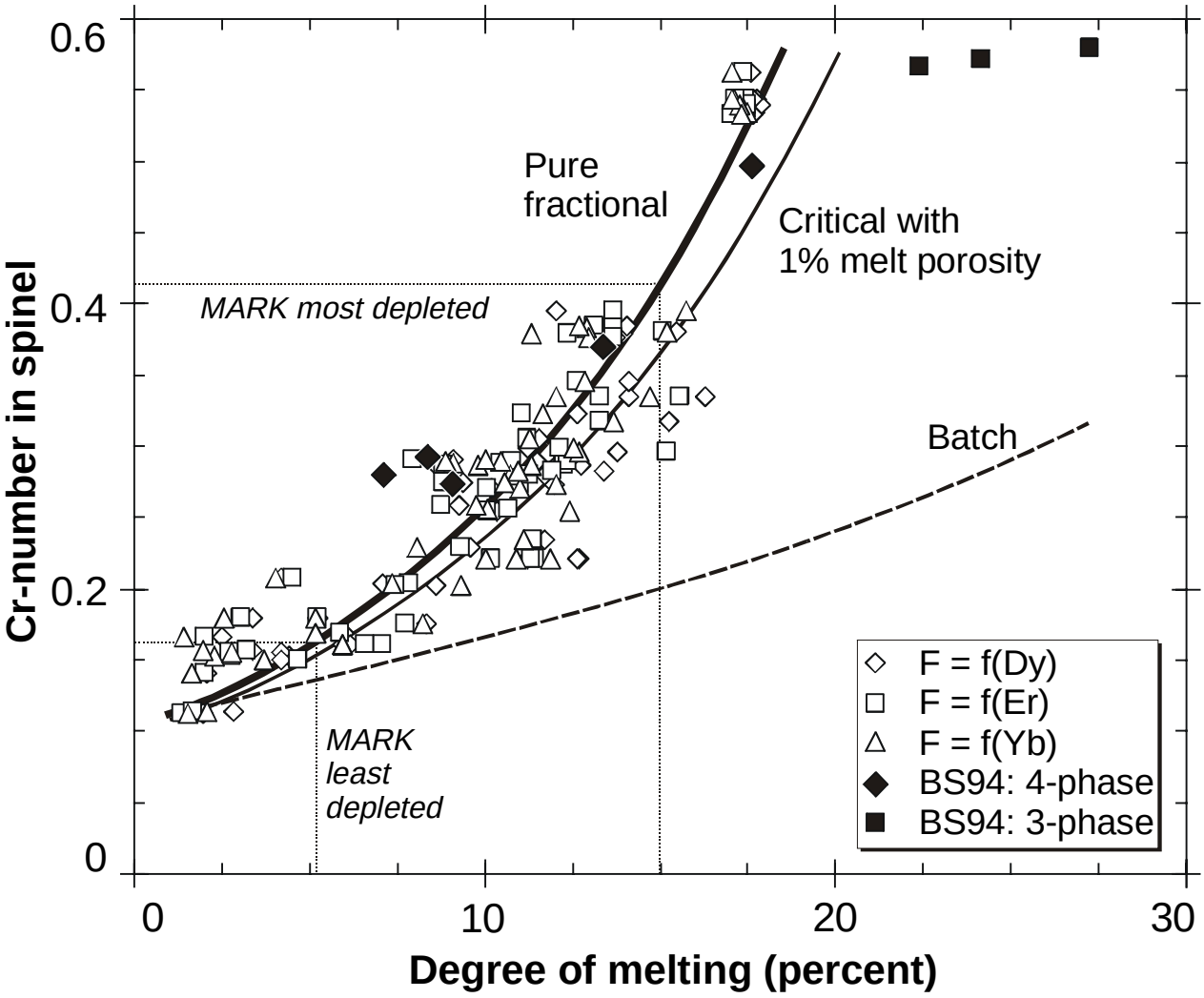

Fig. 3: Calculated degree of melting versus measured Cr-number of spinel. Degrees of melting are calculated from Dy, Er, and Yb concentrations in cpx yielding three independent degrees of melting for each spinel Cr-number. All individual data points are shown for pure fractional melting (open symbols). Exponential fit (thick black curve) is based on average degree of melting for each sample. Same procedure yields melting trajectories for batch melting (dashed curve) and critical melting with 1% residual melt porosity (thin black curve) using equations after (SOBOLEV and SHIMIZU, 1992). The degree of fractional melting (F) as a function of Cr-number can be expressed as F = 10 ln(Cr-number) + 24 for Cr-numbers between 0.1 and 0.6. Most and least depleted Cr-number compositions from the MARK area are shown. Experimental data agree with the melting trend for cpx-bearing residues shown as filled diamonds (BAKER and STOLPER, 1994).

As an independent test, spinel Cr-number – liquid fraction pairs from 10 kbar batch melting experiments (BAKER and STOLPER, 1994) are plotted as closed symbols in Figure 3. These are consistent with our calculated melting curve as long as cpx is present in the residue. Direct modeling of major elements chromium and aluminum yields similar results for batch and fractional melting, both of which agree with our results[1]. By contrast, in our models F is calculated from incompatible trace elements Dy, Er, and Yb, which show considerable differences between fractional and batch mechanisms (Fig.3). The experimental data plot above our fractional melting curve at low F. This is because the starting composition chosen for this particular experiment is relatively rich in chromium, resulting in a significantly higher initial spinel Cr-number than observed in the most fertile abyssal peridotites and a melting trend that is shifted towards higher Cr-numbers at a given melt fraction.

Using both major and trace element melting indicators, some interesting inferences can begin to be drawn regarding the geodynamic controls on melting globally. First, if only non-hotspot peridotites are considered, the degree of melting appears to be largely controlled by the spreading rate, as previously suggested by Niu and Hekinian (NIU and HEKINIAN, 1997). Moderately incompatible trace elements confirm their observation. However, there is a large compositional variation in the SWIR, AAR and CIR samples. Therefore the apparent correlation with spreading rate is biased because Hess Deep and MARK area (Mid-Atlantic Ridge south of Kane Fracture Zone) are the only locations on their respective ridges yet investigated for both major and trace elements.

A second geodynamic control on the degree of melting, one which is superimposed on the effect of the spreading rate, is the vicinity to a transform offset. Most abyssal peridotites are collected at fracture zones. Hess Deep mantle rocks on the other hand, were generated in the center of a spreading segment far from a transform fault (DICK and NATLAND, 1996), which may explain their extreme depletion. In our database, only three other locations are not situated directly at a major fracture zone (MARK area, Green Rock

[1] NOTE. In order to compare the difference between batch and fractional melting for the spinel Cr-number directly, we treated Al and Cr as “trace elements” and repeated the previously mentioned batch and fractional melting models to obtain the spinel composition. We calculated mineral/melt partition coefficients

Hill on CIR 25°S, and CIRCE93 samples on CIR axis 12°S). The two latter are among the most depleted samples from the CIR, indicating that all other CIR fracture zone samples may have been affected by a transform fault effect (deepening the final depth of melting near the cold edge of a transform fault) (BENDER ET AL., 1984; NATLAND and MELSON, 1980). Our quantitative tool of Figure 3 can now be used to estimate the degree of melting for oceanic mantle rocks where often only spinel data are available. The MARK area is of particular importance, because a large set of mantle melting residues contains evidence for this transform fault effect (GHOSE ET AL., 1996). Peridotites directly at Kane Fracture Zone have low Cr-number of around 0.17, a value that systematically increases to 0.41 in highly depleted residues near the ridge center (Fig.3.). Applying our melting function, we estimate the magnitude of the transform fault effect. The most depleted peridotite corresponds to 15% melting and the most fertile sample to 5%. Thus, the minimal difference in the degree of melting as a result of deepening of the final depth of melting towards the transform fault is 10% (i.e. a factor of three).

Finally, the vicinity of a hotspot is believed to increase the degree of melting. Johnson et al. (JOHNSON ET AL., 1990) attribute the strong trace element depletion in the Bouvet FZ peridotites to this phenomenon. Comparing these depleted Bouvet FZ samples to the fertile Islas Orcadas FZ peridotites away from the Bouvet hotspot provides an estimate of the additional hotspot-imposed melting, because of the identical spreading rate at the SWIR and the location at a fracture zone. For the SWIR, the additional degree of melting related to the vicinity of the Bouvet hotspot is 8%. On a global scale, the Bouvet FZ mantle rocks are not uniquely depleted. Green Rock Hill harzburgites have nearly identical major and trace element compositions to the Bouvet samples. Yet, no nearby hotspot has been detected in the area of Rodrigues Triple Junction. It therefore seems that the geodynamic combination near-hotspot, transform fault, slow-spreading ridge can produce similar residual mantle rocks as a hotspot-free, non-transform, intermediate spreading setting.

Another important question is whether the observed correlations shown in Fig.1 may also be inherited from the mantle source prior to melting. The calculations that are based on these observations assume that the premelting Cr-numbers and HREE concentrations are uniform. It is also possible that the two parameters were already similarly correlated prior

---

from the melting experiments of Baker and Stolper, and found that these extreme models yield very similar Cr-numbers at a given F. Therefore it is valid to plot the Baker and Stolper data in Fig.3.

to the most recent (MORB) melting event. If the latter is true, we would expect that the calculated degree of melting should not be correlated with tectonic parameters such as spreading rate. Further, this would imply that the systematic depletion trend of the MARK area peridotites (GHOSE ET AL., 1996) is fortuitous and not directly related to a transform fault effect. Such inherited depletion might be correlated with abundances of radiogenic isotopes. Future studies that focus on the relationship between melting and regional tectonics will help resolve this issue.

References

Anders E. and Grevesse N. (1989) Abundances of the elements: meteoric and solar. *Geochim. Cosmochim. Acta* **53**, 197-214.

Baker M. B. and Stolper E. M. (1994) Determining the composition of high-pressure mantle melts using diamond aggregates. *Geochim. Cosmochim. Acta* **58**, 2811-2827.

Batanova V. G., Suhr G., and Sobolev A. V. (1998) Origin of geochemical heterogeneity in the mantle peridotites from the Bay of Islands Ophiolite, Newfoundland, Canada; ion probe study of clinopyroxenes. *Geochim. Cosmochim. Acta* **62**(5), 853-866.

Bender J. F., Langmuir C. H., and Hanson G. N. (1984) Petrogenesis of basalts from the Tamayo Region, East Pacific Rise. *J. Petrol.* **25**, 231-254.

Dick H. J. B. (1989) Abyssal peridotites, very slow spreading ridges and ocean ridge magmatism. *Geol. Soc. Spec. Publ.* **42**, 71-105.

Dick H. J. B., Fisher R. L., and Bryan W. B. (1984) Mineralogic variability of the uppermost mantle along mid-ocean ridges. *Earth Planet . Sci. Lett.* **69**(1), 88-106.

Dick H. J. B. and Natland J. H. (1996) Late-stage melt evolution and transport in the shallow mantle beneath the East Pacific Rise. *Proc. ODP, Sci. Res.* **147**, 103-134.

Ghose I., Cannat M., and Seyler M. (1996) Transform fault effect on mantle melting in the MARK area (Mid-Atlantic Ridge south of the Kane transform). Geology 24(12), 1139-1142.

Hart S. R. and Dunn T. (1993) Experimental cpx/melt partitioning of 24 trace elements. Contrib. Mineral. Petrol. 113, 1-8.

Jochum K. P., Dingwell D. B., Rocholl A., Stoll B., Hofmann A. W., and others a. (2000) The preparation and preliminary characterisation of eight geological MPI-DING standard reference glasses for in-situ microanalysis. Geost. Newslett. 24, 87-133.

Johnson K. T. M. and Dick H. J. B. (1992) Open system melting and temporal and spatial variation of peridotite and basalt at the Atlantis II fracture zone. J. Geophys. Res. 97(6), 9219-9241.

Johnson K. T. M., Dick H. J. B., and Shimizu N. (1990) Melting in the oceanic upper mantle; an ion microprobe study of diopsides in abyssal peridotites. J. Geophys. Res. 95, 2661-2678.

Kelemen P. B., Hirth G., Shimizu N., Spiegelman M., and Dick H. J. B. (1997) A review of melt migration processes in the adiabatically upwelling mantle beneath oceanic spreading ridges. *Phil. Trans. R. Soc. London* **355**, 283-318.

Kelemen P. B., Shimizu N., and Salters V. J. M. (1995) Extraction of mid-ocean-ridge basalt from the upwelling mantle by focused flow of melt in dunite channels. *Nature* **375**, 747-753.

Michael P. J. and Bonatti E. (1985) Peridotite composition from the North Atlantic; regional and tectonic variations and implications for partial melting. *Earth Planet. Sci. Lett.* **73**(1), 91-104.

Natland J. H. and Melson W. G. (1980) Composition of basaltic glasses from the East Pacific Rise and Siqueros fracture zone, near 9 degrees N. *Ini. Rep. DSDP* **54**(1980), 705-724.

Niu Y. and Hekinian R. (1997) Spreading-rate dependence of the extent of mantle melting beneath ocean ridges. *Nature* **385**(6614), 326-329.

Pearce J. A., Barker P. F., Edwards S. J., Parkinson I. J., and Leat P. T. (2000) Geochemistry and tectonic significance of peridotites from the South Sandwich arc-basin system, South Atlantic. *Contrib. Mineral. Petrol.* **139**, 36-53.

Ross K. and Elthon D. (1997) Extreme incompatible trace-element depletion of diopside in residual mantle from south of the Kane F.Z. *Proc. ODP, Sci. Res.* **153**, 277-284.

Shimizu N., Semet M. P., and Allegre J. C. (1978) Geochemical applications of quantitative ion microprobe analysis. *Geochim. Cosmochim. Acta* **42**, 1321-1334.

Sobolev A. V. and Shimizu N. (1992) Extremely depleted magmas and oceanic mantle permeability. *Dokl. Akad. Nauk* **326**, 354-360.

Suhr G. (1999) Melt migration under oceanic ridges: inferences from reactive transport modelling of upper mantle hosted dunites. *J. Petrol.* **40**, 575-599.

Suhr G., Seck H. A., Shimizu N., Günther D., and Jenner G. (1998) Infiltration of refractory melts into the lowermost oceanic crust: evidence from dunite- and gabbro-hosted clinopyroxenes in he Bay of Islands Ophiolite. *Contrib. Mineral. Petrol.* **131**, 136-154.

Chapter 4: Mantle melting beneath the Gakkel Ridge (Arctic Ocean): Abyssal peridotite spinel compositions

Eric Hellebrand, Jonathan E. Snow & Richard Mühe

Submitted to *Chemical Geology*

Chapter 4: Mantle melting beneath the Gakkel Ridge (Arctic Ocean): Abyssal peridotite spinel compositions

Abstract – The ultra-slow spreading Gakkel Ridge represents one of the most extreme spreading environments on the Earth. Full spreading rates there of 0.6-1.3 cm/yr and $Na_{8.0}$ in basalts of 3.3 imply an extremely low degree of mantle partial melting. For this reason, the complementary degree of melting registered by abyssal peridotite melting residues is highly interesting. In a single sample of serpentinized peridotite from Gakkel Ridge, we found spinels which, though locally altered, have otherwise unzoned and thus primary compositions in the cores of the grains. These reflect a somewhat higher degree of melting of the uppermost oceanic mantle than indicated by basalt compositions. Cr/(Cr+Al) ratios of these grains lie between 0.23 and 0.24, which is significantly higher than spinels from peridotites collected along the faster spreading Mid-Atlantic and Southwest Indian Ridges. Crustal thickness at Gakkel Ridge can be calculated from the peridotite spinel compositions, and is thicker than the observed crustal thickness of less than 4 km estimated from gravity data, or predicted from global correlations between spreading rate and seismically determined crustal thickness. This unexpected result may be due to enhanced compositional heterogeneity at low degrees of melting, or may reflect a higher overall degree of depletion for the Gakkel Ridge than was previously thought.

4.1. Introduction

The Gakkel Ridge extends for 1800 km in the Arctic Ocean from the north coast of Greenland to the north coast of Siberia (Fig.1). It is the world‘s slowest-spreading mid-ocean ridge, with full spreading rates ranging from 1.3 cm/yr at the European end of the ridge to 0.6 cm/yr at the Siberian end in the Laptev Sea. The fastest part of the Gakkel ridge is thus slower than the slowest part of the next most well-studied ultraslow-spreading ridge, the Southwest Indian Ridge (SWIR). The Gakkel Ridge is characterized by an extremely deep rift valley, with axial depths between 4600 m and 5100 m (Coakley and Cochran, 1998). Major transform offsets are absent, and the spreading is completely orthogonal.

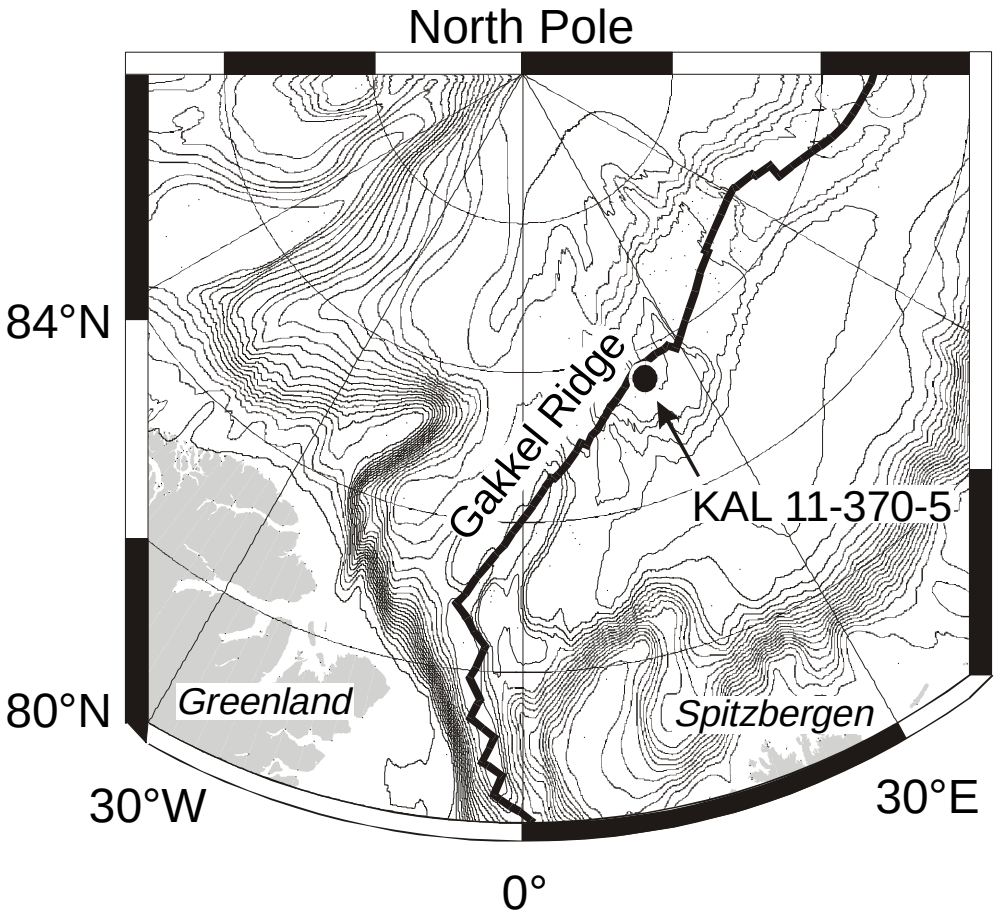

Fig. 1: Bathymetric map of the Arctic Ocean, showing the ultraslow spreading Gakkel Ridge, and the sampling location of box core ARK IV/3: KAL 11-370-5.

Except for a few basaltic glass shards and altered basalt fragments from two sediment cores (Mühe et al., 1997; Mühe et al., 1991; Mühe et al., 1993), little is known about the chemical composition of the Gakkel Ridge crust and mantle. The basalts appear to be the products of very low degrees of mantle melting and confirm its end member position in the global correlation between basalt chemistry and extent of mantle melting beneath ocean ridges (Klein and Langmuir, 1987; Langmuir et al., 1992). Further, gravity studies estimate a crustal thickness between 1 and 4 km for the western Gakkel Ridge (Coakley and Cochran, 1998), much lower than the canonical 6-7 km crust observed beneath the remainder of the Earth's oceans. This is in accordance with simple thermal models predicting a sharp drop-off in crustal thickness at spreading rates under 2-3 cm/yr (Reid and Jackson, 1981).

Spinel composition is a useful tracer of melting in residual peridotites (Dick and Bullen, 1984; Hellebrand et al., submitted). The relative degree of melting calculated from abyssal peridotite spinel compositions is thought to be correlated with spreading rate (Niu and Hekinian, 1997). Gakkel Ridge should thus represent the lower end member in terms of spreading rate and degree of melting on the global mid-ocean ridge system. For this reason, we located and studied relict spinel compositions in extremely altered serpentinized mantle peridotites from Gakkel Ridge.

4.2. Results

The abyssal peridotite fragments were collected in 1987 in box core KAL 11/370-5 during cruise ARK IV/3 of the RV Polarstern at a water depth of 4570 m at 85°54‘N, 22°43‘E (Thiede, 1988) (Fig.1). Altered basalt fragments were recovered in the same box core (Mühe et al., 1991; Mühe et al., 1993). At this location, the full spreading rate is 1.19 cm/yr (Coakley and Cochran, 1998). The sampling location is on the southern flank of the ridge at a distance of 3.3 km to the central axial valley (Mühe et al., 1991). This corresponds to a crustal age of 550 ka.

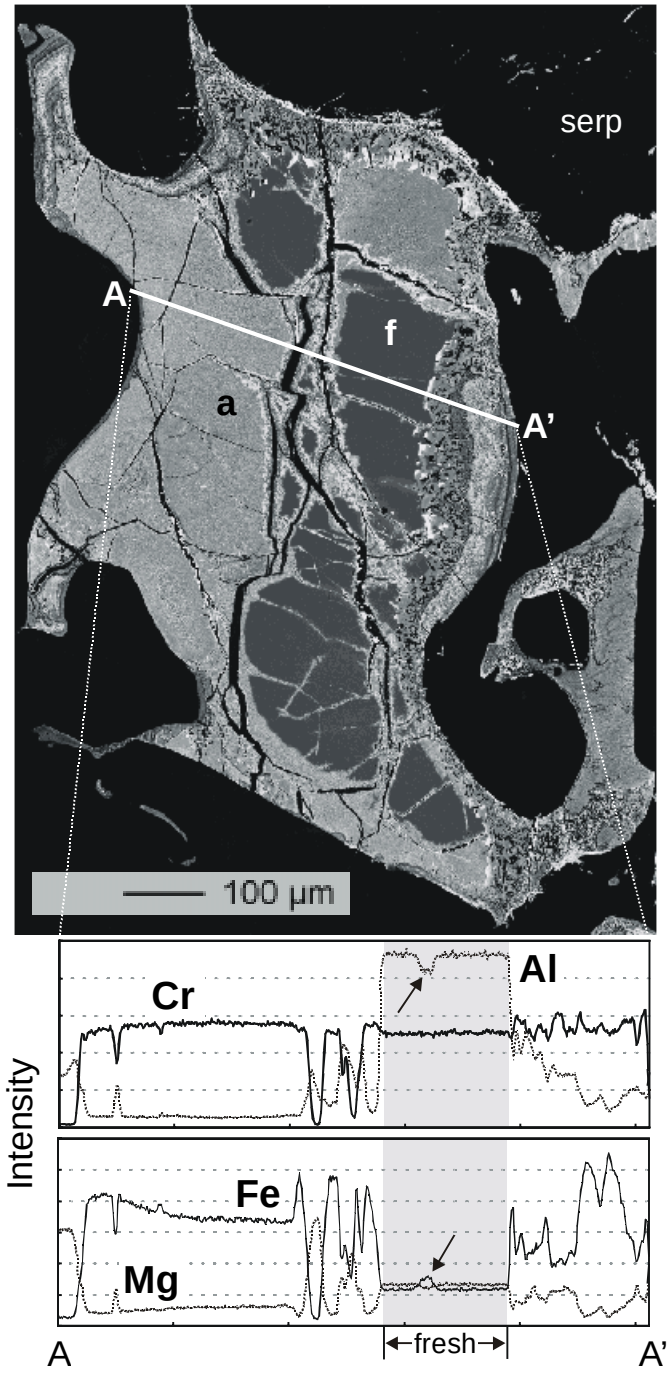

Fig. 2: Backscatter image of a highly altered, porphyroclastic spinel grain from serpentinized peridotite sample KAL 11/370-5-4. Dark grey areas represent unaltered, fresh spinel (f), bright areas are altered zones (a) and serp denotes the serpentinized silicate matrix. Element intensities of Cr, Al, Mg and Fe across profile A-A' profile are shown below. The unaltered region is highlighted in grey. Note the rapid decrease of Al at the boundary from fresh to altered spinel and the constant Cr intensity in the fresh as well as in the altered zones. The arrows in the grey highlighted area of the element profiles show the effect of a thin fracture that runs subparallel to the profile, resulting in a slight but significant decrease in aluminium and a similar increase in iron content.

About ten serpentinite fragments with diameters from 5 cm up to >10 cm (fist size) were studied (one to four polished thin sections). As a result of serpentinization and subsequent ocean floor weathering, primary silicates are not preserved, but textures of pyroxene pseudomorphs and spinels clearly indicate a mantle origin. Cr-spinels of most the samples appear completely oxidized and opaque in thin section. One sample KAL 11/370-5-4 contains small relicts of apparently unaltered spinel cores surrounded by alteration products. The spinels are pale yellow-brown in transmitted light indicating a low Cr content as observed in other relatively fertile peridotites. A backscattered electron image (Fig. 2) shows a porphyroclastic spinel from this sample, with a highly irregular holly-leaf shape that is typical for residual mantle rocks. Alteration progresses along fractures in the spinel. Dark grey areas show unaltered, primary Cr-spinel, whereas altered spinel is characterized by fine-grained, bright areas.

Several electron microprobe line profiles were run across the spinels in order to assess the degree of zoning imposed as a result of subsolidus reequilibration or low-temperature alteration. For this purpose, selected elements intensities (Al, Cr, Mg, and Fe) were measured on a JEOL JXA 8900RL electron probe microanalyzer using an acceleration potential of 20 kV, a beam current of 20 nA, a spot size of 2 µm, an interval of 1 µm and a dwell time of 1 s on each spot. The result of one of these line scans is also shown in Fig. 2. Fresh domains have constant counting rates for all elements that drastically change at fractures and, most importantly, at the weathering front. Within the fresh region, no compositional zoning is observed. In the altered material Al is rapidly removed from the spinel lattice, whereas Cr counting rates remain unchanged in the altered regions (bright) with respect to the fresh spinel.

Spot analyses were obtained in the centers of fresh areas of four different spinel porphyroclasts by electron microprobe (20 kV, 20 nA, spot size 2 µm). The average composition for each grain (two or three analyses each) is shown in Table 1. Fresh spinels from sample KAL 11/370-5-4 peridotite have Cr# (molar ratio Cr/(Cr+Al)) between 0.232 and 0.246. Their titanium content is very low (average TiO_2: 0.03%). At the immediate contact to the altered regions, only the Fe^{3+} and Ti contents are slightly higher.

The microprobe profiles and spot analyses show that the transition from the fresh spinel (yellow-brown in transmitted light) into oxidized (opaque) material is a sharp contact that is characterized by dramatic differences in Al and Fe. In the fresh domains the composition remains constant, except for the direct vicinity (~<5 µm) of cracks. At these fractures,

excursions in aluminium and iron content (arrows in Figure 2) are highly visible in BSE image and microprobe profiles. These features indicate that alteration has proceeded along an alteration front outward from cracks in the spinel and has not affected their cores.The analyses listed in Table 1 thus reflect the primary spinel composition.

Table 1: Spinel analyses (wt.%), from serpentinized peridotite sample KAL 11/370-5-4

	grain 1	grain 2	grain 3	grain 4
Oxides				
TiO_2	0.05	0.03	0.02	0.04
Al_2O_3	45.68	45.08	46.41	45.89
Cr_2O_3	21.84	21.95	20.86	21.53
FeO	13.20	13.94	13.18	13.53
MgO	19.00	18.53	18.82	18.72
MnO	0.14	0.18	0.17	0.18
CaO	0.00	0.01	0.01	0.01
NiO	0.25	0.22	0.24	0.26
Na_2O	0.00	0.01	0.02	0.00
K_2O	0.00	0.00	0.01	0.00
Sum	100.18	99.95	99.74	100.15
Cations (32 oxygens per formula unit)				
Ti	0.01	0.00	0.00	0.01
Al	11.66	11.58	11.86	11.72
Cr	3.74	3.78	3.58	3.69
Fe_t	2.39	2.54	2.39	2.45
Mg	6.13	6.02	6.08	6.05
Mn	0.03	0.03	0.03	0.03
Ca	0.00	0.00	0.00	0.00
Ni	0.04	0.04	0.04	0.04
Na	0.00	0.00	0.01	0.00
K	0.00	0.00	0.00	0.00
Sum	24	24	24	24
Fe^{3+}	0.59	0.64	0.56	0.57
Cr/(Cr+Al)	0.243	0.246	0.232	0.239
$Mg/(Mg+Fe^{2+})$	0.772	0.759	0.769	0.763

4.3. Discussion

The Cr# and Mg# (molar ratio $Mg/(Mg+Fe^{2+})$) of spinel has proven to be a very sensitive indicator for melt extraction (Dick, 1989; Dick and Bullen, 1984; Dick et al., 1984; Johnson and Dick, 1992; Johnson et al., 1990; Michael and Bonatti, 1985), melt-peridotite reactions during focused porous flow (Allan and Dick, 1996; Dick and Natland, 1996; Kelemen et al., 1992; Kelemen et al., 1997) and melt-wall rock reactions in the vicinity of intruding magmatic veins (Cannat et al., 1997; Hellebrand et al., 1999; Niu and Hekinian, 1997). With increasing degree of melting, decreasing activity of aluminium in the peridotite leads to an increase in equilibrium Cr# in spinel as shown in the melting trend of Fig 3. A systematic study of residual peridotites in the MARK (Mid-Atlantic Ridge near Kane fracture zone) area has shown very limited local variation of spinel compositions. On a regional scale, however, the mantle rocks become increasingly depleted away from the Kane FZ (Ghose et al., 1996).

Also shown in Fig. 3 are spinel compositions from selected localities, illustrating the limited local variation in residual mantle rocks. The samples from these dredge hauls and boreholes were specifically selected because they do not contain plagioclase (Seyler and Bonatti, 1997) or crosscutting magmatic veins (Hellebrand et al., 1999; Niida, 1997), which may significantly modify the host rock composition and produce large compositional variations, even on thin section scale. Therefore, it is important to estimate whether plagioclase was initially present in the peridotite. Plagioclase in abyssal peridotites is commonly interpreted as a trapped melt product in the widest sense (Dick, 1989), rather than being formed during the transition from spinel to plagioclase stability field (Hamlyn and Bonatti, 1980). Plagioclase-bearing peridotites commonly have high (>0.1 wt.%) TiO_2 contents (Dick, 1989; Dick and Bullen, 1984) as shown in Fig. 4. The very low Ti content in the spinel of the Gakkel Ridge sample supports the absence of plagioclase and attests to the residual nature of this particular sample.

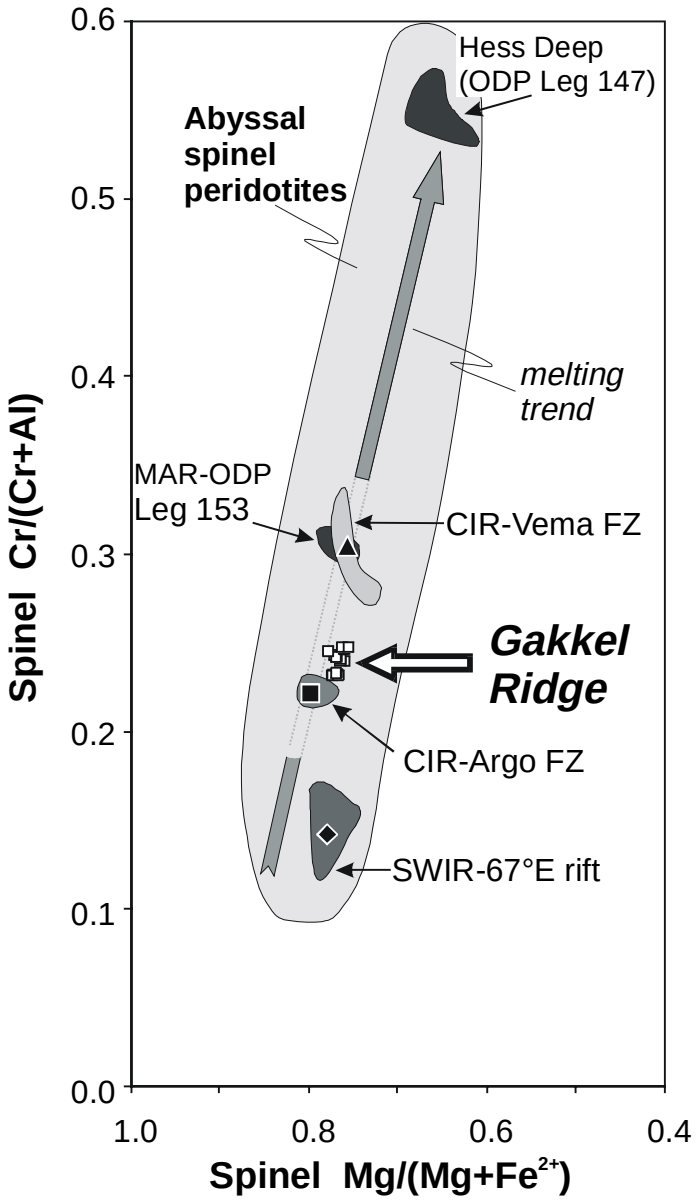

Fig. 3: Spinel Cr# vs. Mg# of serpentinized peridotite sample KAL 11/370-5-4. All point analyses shown. Spinel compositions from other abyssal peridotites are shown for comparison to illustrate the fairly narrow compositional range of plagioclase-free and vein-free peridotites from one location. Closed symbols are the average of this range, represented by the enclosing fields. The studied Gakkel Ridge peridotite is significantly more depleted than the most fertile spinel peridotite from the faster spreading easternmost SWIR (diamond). Spinel peridotite field after (Dick and Bullen, 1984). Other data unpublished results.

Basalts recovered along with these peridotites have extremely high $Na_{8.0}$ of 3.3 and chondrite-normalized Sm/Yb ratios of 1.4 to 1.5 that indicate some of the lowest degrees of melting ever observed along the mid-ocean ridges. The not particularly low Cr# of the peridotites is nowhere near the extremes observed at mid-ocean ridges. Indeed, many spinels from residual harzburgites from the Southwest Indian Ridge have lower Cr# (see Fig. 3). In fact, the Cr# of these samples corresponds to an estimated degree of fractional

melting of 9%, applying the quantitative melting tool of Hellebrand et al. (submitted). This is at least 5% more than the most fertile SWIR peridotites.

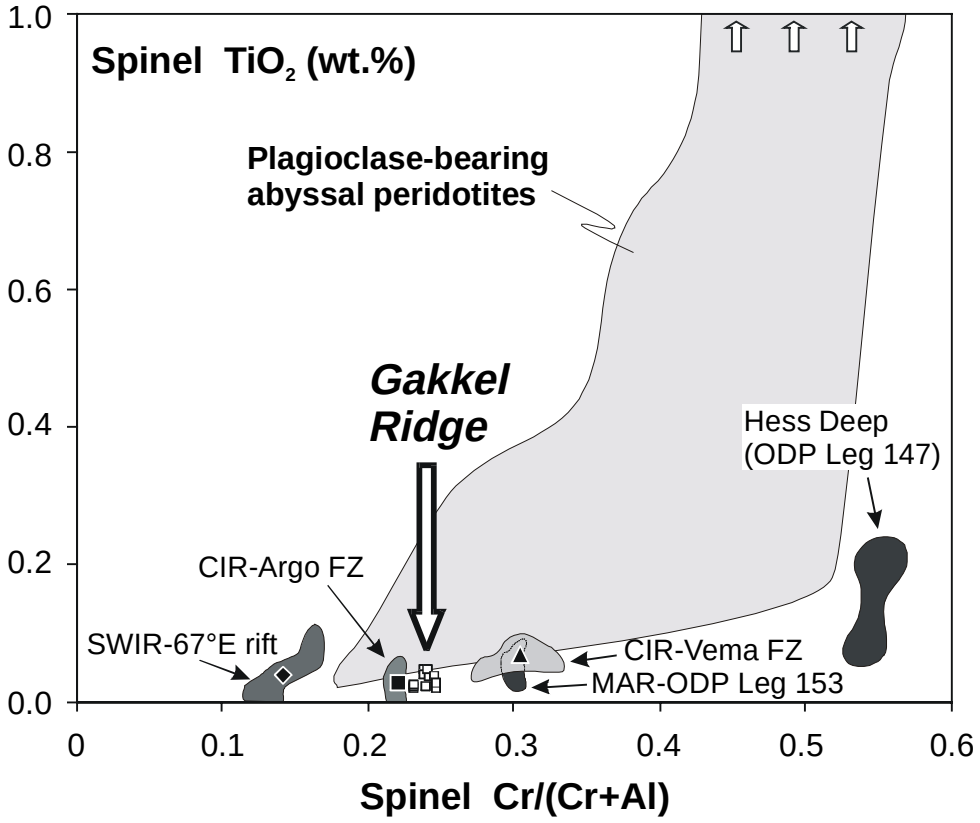

Fig. 4: Spinel TiO_2 vs. Cr# content of serpentinized peridotite sample KAL 11/370-5-4. All point analyses shown. Spinels from plagioclase-free peridotites are characterized by very low Ti contents, whereas plagioclase-bearing peridotite have elevated titanium concentrations, often exceeding 1 wt.%. Most plagioclase-bearing peridotites have higher Cr# than residual mantle rocks. Data from (Dick and Bullen, 1984; Dick et al., 1984) and own unpublished results.

In order to test presence or absence of a spreading rate dependence based on peridotite compositions, Gakkel Ridge peridotites should be compared to other abyssal peridotites from similar non-transform settings. As seen in the MARK area peridotites, the transform fault effect strongly influences peridotite compositions. At Kane FZ, fertile peridotites with an average spinel Cr# of 0.17 occur, a value that systematically increases to 0.41 away from the transform (Ghose et al., 1996). This means that the corresponding degree of melting increases from 5% at Kane FZ to 15% near the center of the segment (Hellebrand et al., submitted). Because of its magnitude, the transform fault effect, which is superimposed on the spreading rate effect, produces a strong bias in the global geodynamic systematics from a residual mantle perspective, since most abyssal peridotites were collected directly at fracture zone walls. Large-offset transform faults are

omnipresent along the very slow spreading SWIR. Therefore, the fertility of most SWIR peridotites, which are mainly low-degree partial melting residues, is the result of the slow spreading rate combined with the cooling effect of the transform faults.

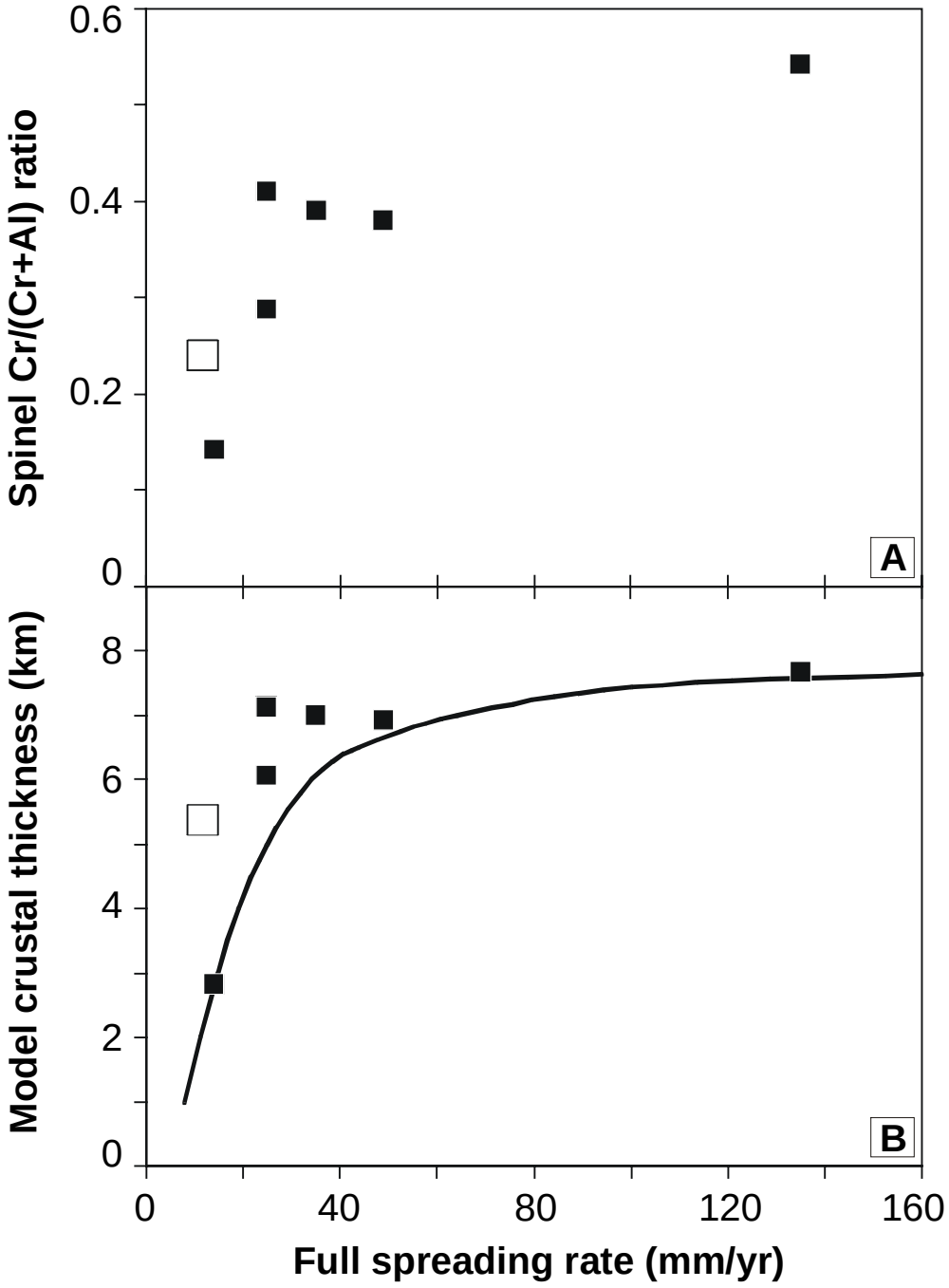

Fig. 5: (a) Local full spreading rate versus spinel Cr# of non-transform peridotites, and **(b)** model crustal thickness. Crustal thickness is calculated from average local spinel compositions, applying empirical melting tool of (Hellebrand et al., submitted) and equations by (Forsyth, 1993). Open square: Gakkel Ridge, closed squares: other non-transform peridotites. Thick black curve represents predicted spreading-rate dependent crustal thickness favored by Reid and Jackson (Reid and Jackson, 1981). Spreading rates (full) calculated from Nuvel 1 using the online calculator at InterRidge homepage.

At Gakkel Ridge, spreading is orthogonal and transform faults appear to be absent (Coakley and Cochran, 1998). In order to address the effect of the spreading rate, the spinels from these partial-melting residues should be compared to similar axial peridotite occurrences. Although they are not as common as in fracture zones, such peridotites do occur (Cannat, 1993; Cannat et al., 1995), but published mineral data are scarce. Only for Hess Deep in the Pacific (Dick and Natland, 1996) and the MARK area (Ghose et al., 1996; Niida, 1997; Sinton, 1978), published spinel data are available. Further, we have unpublished data for Green Rock Hill on the southermost CIR, the easternmost SWIR rift, and the CIR axis at 12°S (Hellebrand et al., *Chapter 2*). In Fig. 5a, spinel Cr# of these non-transform peridotites are plotted versus the local spreading rate. Despite the scarcity of the data, spinel Cr# increase with spreading rate.

We can now apply the quantitative melting tool that uses spinel compositions from residual peridotites to estimate global variations in crustal thickness, and its dependence on spreading rate. In principle, peridotite compositions provide a direct estimate of the maximum degree of melting of the melting column. In a simplified way, this total extent of melting, F_{max}, can be expressed as

$$F_{\max} = B \cdot \left(Z_0 - Z_f\right), \tag{1}$$

where B is the melt production rate per km and Z_0 and Z_f are the initial- and final depth of melting, respectively (Forsyth, 1993). Further, the crustal thickness, H, can also be expressed as a function of these variables:

$$H = \frac{B \cdot \left(Z_0^2 - Z_f^2\right)}{2}. \tag{2}$$

Assuming that B is constant throughout the melting column, and melting commences at a constant depth of 70 km, Z_f can be directly calculated from $F_{max} = F_{sp}$, where the observed relationship between cpx trace element composition and spinel Cr# yields the empirical melting function, as proposed by (Hellebrand et al., submitted)

$$F_{sp} = 0.1 \cdot \ln\left(Cr\#\right) + 0.24. \tag{3}$$

In Fig. 5b, the calculated crustal thickness for each average non-transform peridotite occurrence is plotted versus spreading rate. The thick black curve is a predicted relationship between spreading rate and oceanic crustal thickness, which is relatively

constant at fast spreading rates, but is believed to decrease rapidly at very slow spreading rates (Reid and Jackson, 1981). Clearly, the Gakkel Ridge sample yields a model crustal thickness that is much thicker than expected from this model. The thin crust at Gakkel Ridge, predicted by the thermal model of Reid and Jackson agrees well with the observed crustal thickness estimated from gravity data at Gakkel Ridge (Coakley and Cochran, 1998). There are three possible explanations to explain why the Gakkel Ridge peridotite produces this unexpected result.

The first interpretation is that the regional degree of melting is not as low as predicted from global correlation estimates. This would imply that mantle melting in general is not as strongly controlled by spreading rate as by other factors such as mantle temperature, mantle source composition or ridge obliquity. This interpretation, however, is not in agreement with the basalt compositions that indicate an extremely low degree of melting.

A second possibility is that the studied sample does not represent the local/dredge average, but may be an outlying point due to natural heterogeneity. Significant modal and compositional variations of peridotites within a single dredge haul or location are common (Dick and Bullen, 1984; Dick et al., 1984). However, the largest variations are mostly found in areas with abundant plagioclase-bearing peridotites, which are non-residual rocks (Dick, 1989; Seyler and Bonatti, 1997). Plagioclase-free peridotites from a single drill hole, away from crosscutting magmatic dikelets, have a fairly narrow Cr# range, typically ~0.02 – 0.06 (Dick and Natland, 1996; Niida, 1997; Sinton, 1978), as do most dredged residual abyssal peridotites. However, exceptions to this general rule exist, such as peridotites from Marie Celeste FZ on the CIR (Cr# from 0.17 to 0.29 within a single dredge) and an outcrop on the CIR axis at 12°S (Cr# from 0.31 to 0.53 within a single dredge) (Hellebrand et al., in prep). Accepting that these values represent the extreme local variations at a scale sampled by dredging, we can assume that the underlying average Cr# of the mantle at this part of Gakkel Ridge is not dramatically different from what we have measured.

Finally, these spinel compositions might reflect the heterogeneity of melt extraction at ultraslow spreading ridges. At slow spreading ridges, the degree of melting from the mantle has been proposed to vary along the spreading center (Whitehead et al., 1984). More melt is extracted at the center of the segment and less at the distal ends, The melt is laterally focused towards the center of the segments, as suggested by gravity patterns (Lin et al., 1990). This effect is expected to be more pronounced at ultraslow spreading rates, though insufficient data currently exist to test this proposition. The intermediate spinel

compositions seen here might then represent the center of a spreading cell. This would be consistent with their association with basalts. The lower average degree of melting of the basalts would agree with this scenario, as the basalts average a much larger melting volume than is sampled by the peridotites. Despite the scant evidence available regarding magmatic segmentation along Gakkel Ridge (Coakley and Cochran, 1998) this remains the most plausible scenario.

4.4. Conclusions

1. Spinel cores in this study represent primary mantle values despite advanced serpentinization and oxidation of the rock.

2. Overall degrees of melting are relatively low compared to global abyssal peridotites.

3. The extremely low degree of melting observed in spatially associated basalt glasses (Mühe et al., 1997; Mühe et al., 1991; Mühe et al., 1993) is not seen in these samples. Many areas (mostly on the very slow spreading SW Indian Ridge) show equivalent or lower Cr#.

4. Model crustal thickness at the ultraslow spreading Gakkel Ridge, as calculated from the peridotite spinel composition, is thicker than estimated from existing gravity data and predicted spreading-rate dependent correlations.

5. The reason for this greater than expected depletion may be local heterogeneity due to enhanced melt focussing at an ultra-slow spreading ridge.

These spinel analyses from a single sample of mid-ocean ridge mantle represent just a beginning. They are not in themselves sufficient to characterize an entire mid-ocean ridge. Further sampling and analysis of Arctic mantle rocks is required to fully address the evolution of this unique mid-ocean ridge system.

4.5. References

Allan, J.F. and Dick, H.J.B., 1996. Cr-rich spinel as a tracer for melt migration and melt-wall rock interaction in the mantle: Hess Deep, Leg 147. Proc. ODP, Sci. Res., 147: 157-172.

Cannat, M., 1993. Emplacement of mantle rocks in the seafloor at mid-ocean ridges. J. Geophys. Res., 98: 4163-4172.

Cannat, M., Chatin, F., Whitechurch, H. and Ceuleneer, G., 1997. Gabbroic rocks trapped in the upper mantle at the Mid-Atlantic Ridge. Proc. ODP, Sci. Res., 153: 243-264.

Cannat, M. et al., 1995. Thin crust, ultramafic exposures, and rugged faulting patterns at the Mid-Atlantic Ridge (22°-24°N). Geology, 23: 49-52.

Coakley, B.J. and Cochran, J.R., 1998. Gravity evidence of very thin crust at the Gakkel Ridge (Arctic Ocean). Earth Planet. Sci. Lett., 162: 81-95.

Dick, H.J.B., 1989. Abyssal peridotites, very slow spreading ridges and ocean ridge magmatism. Geol. Soc. London Spec. Publ., 42: 71-105.

Dick, H.J.B. and Bullen, T., 1984. Chromian spinel as a petrogenetic indicator in abyssal and alpine-type peridotites and spatially associated lavas. Contrib. Mineral. Petrol., 86: 54-76.

Dick, H.J.B., Fisher, R.L. and Bryan, W.B., 1984. Mineralogic variability of the uppermost mantle along mid-ocean ridges. Earth Planet. Sci. Lett., 69: 88-106.

Dick, H.J.B. and Natland, J.H., 1996. Late-stage melt evolution and transport in the shallow mantle beneath the East Pacific Rise. Proc. ODP, Sci. Res., 147: 103-134.

Forsyth, D.W., 1993. Crustal thickness and the average depth and degree of melting in fractional melting models of passive flow beneath mid-ocean ridges. J. Geophys. Res., 98: 16073-16079.

Ghose, I., Cannat, M. and Seyler, M., 1996. Transform fault effect on mantle melting in the MARK area (Mid-Atlantic Ridge south of the Kane transform). Geology, 24: 1139-1142.

Hamlyn, P.R. and Bonatti, E., 1980. Petrology of mantle-derived ultramafics from the Owen Fracture Zone, Northwest Indian Ocean: implications for the nature of the oceanic upper mantle. Earth Planet. Sci. Lett., 48: 65-79.

Hellebrand, E., Snow, J.E., Dick, H.J.B. and Hofmann, A.W., submitted. Major and trace element coupling in global mid-ocean ridge melting residues. submitted to Science.

Hellebrand, E.W., Snow, J.E., Dick, H.J.B., Devey, C.W. and Hofmann, A.W., 1999. Reactive crack flow in the oceanic mantle: an ion probe study on cpx from vein-bearing abyssal peridotites. Ofioliti, 24: 106-107.

Hellebrand, E.W., Snow, J.E. and Hofmann, A.W., in prep. Abyssal peridotites are residues of garnet field melting. .

Johnson, K.T.M. and Dick, H.J.B., 1992. Open system melting and temporal and spatial variation of peridotite and basalt at the Atlantis II fracture zone. J. Geophys. Res., 97: 9219-9241.

Johnson, K.T.M., Dick, H.J.B. and Shimizu, N., 1990. Melting in the oceanic upper mantle; an ion microprobe study of diopsides in abyssal peridotites. J. Geophys. Res., 95: 2661-2678.

Kelemen, P.B., Dick, H.J.B. and Quick, J.E., 1992. Formation of harzburgite by pervasive melt/rock reaction in the upper mantle. Nature, 358: 635-641.

Kelemen, P.B., Hirth, G., Shimizu, N., Spiegelman, M. and Dick, H.J.B., 1997. A review of melt migration processes in the adiabatically upwelling mantle beneath oceanic spreading ridges. Phil. Trans. R. Soc. London, 355: 283-318.

Klein, E.M. and Langmuir, C.H., 1987. Global correlations of ocean ridge basalts with axial depth and crustal thickness. J. Geophys. Res., 92: 8089-8115.

Langmuir, C.H., Klein, E.M. and Plank, T., 1992. Petrologic systematics of mid-ocean ridge basalts: constraints on melt generation beneath ocean ridges. In: J. Phipps-Morgan, D.K. Blackman and J.M. Sinton (Editors), Mantle flow and melt generation at mid-ocean ridges. AGU Monograph, pp. 183-280.

Lin, J., Purdy, G.M., Schouten, H., Sempere, J.C. and Zervas, C., 1990. Evidence from gravity data for focused magmatic accretion along the Mid-Atlantic Ridge. Nature, 344: 627-632.

Michael, P., J. and Bonatti, E., 1985. Peridotite composition from the North Atlantic; regional and tectonic variations and implications for partial melting. Earth Planet. Sci. Lett., 73: 91-104.

Mühe, R., Bohrmann, H., Garbe-Schönberg, D. and Kassens, H., 1997. E-MORB glasses from the Gakkel Ridge (Arctic Ocean) at 87°N: evidence for the Earth's most northerly volcanic activity. Earth Planet. Sci. Lett., 152: 1-9.

Mühe, R., Bohrmann, H., Hörmann, P.K., Thiede, J. and Stoffers, P., 1991. Spinifex basalts with komatiite-tholeiite trend from the Nansen-Gakkel Ridge (Arctic Ocean). Tectonophysics, 190: 95-108.

Mühe, R., Devey, C.W. and Bohrmann, H., 1993. Isotope and trace element geochemistry of MORB from the Nansen-Gakkel Ridge at 86° North. Earth Planet. Sci. Lett., 120: 103-109.

Niida, K., 1997. Mineralogy of MARK peridotites: replacement through magma channeling examined from Hole 920D, MARK area. Proc. ODP, Sci. Res., 153: 243-264.

Niu, Y. and Hekinian, R., 1997. Spreading-rate dependence of the extent of mantle melting beneath ocean ridges. Nature, 385: 326-329.

Reid, I. and Jackson, R., 1981. Oceanic spreading rate and crustal thickness. Mar. Geophys. Res., 5: 165-172.

Seyler, M. and Bonatti, E., 1997. Regional-scale melt-rock interaction in lherzolitic mantle in the Romanche fracture zone (Atlantic Ocean). Earth Planet. Sci. Lett., 146: 273-287.

Sinton, J., 1978. Petrology of (alpine-type) peridotites from Site 395, DSDP Leg 45. Ini. Rpts. DSDP, 45: 595-601.

Thiede, J., 1988. Scientific cruise report of Arctic Expedition ARK IV/3. Berichte zur Polarforschung, Reports on Polar Research, 43: 236pp.

Whitehead, J.A., Dick, H.J.B. and Schouten, H., 1984. A mechanism for magmatic accretion under spreading ridges. Nature, 312: 146-148.

Appendix A: Melting modeling

Perfect non-modal fractional melting, as described in *Chapter 2*, was calculated using the equations derived by GAST (1968). The concentration of element *i* in the peridotite residue, C_{wr}, at melt fraction *F* is

$$C_{wr} = \left(\frac{C_0}{1-F}\right)\cdot\left(1-\frac{P\cdot F}{D_0}\right)^{\frac{1}{P}} \quad \text{(A1)}$$

C_0 is the initial whole rock concentration. The initial bulk distribution coefficient D_0 is defined as

$$D_0 = \sum\left(Kd_i^{j/l}\cdot M_{0,j}\right), \quad \text{(A2)}$$

where $M_{0,j}$ is the initial mineral mode of phase *j*, and $Kd^{j/l}$ the experimentally determined mineral/liquid partition coefficient of phase *j*. Similarly, since melting is non-modal, the melt mode P describes the phase proportions that enter the melt.

$$P = \sum\left(Kd^{j/l}\cdot p_j\right), \quad \text{(A3)}$$

where p_j is the melt mode of phase *j*. The melt modes for garnet and spinel stability field are taken from WALTER (1998) and KINZLER (1997), respectively. A residual clinopyroxene that is in equilibrium with the whole rock has a trace element concentration

$$C_{cpx} = \frac{Kd^{cpx/l}}{D_{bulk}}\cdot C_{wr}, \quad \text{(A4)}$$

which can be rewritten to

$$C_{cpx} = \frac{Kd^{cpx/l}\cdot C_0}{D_{bulk}(1-F)}\cdot\left(1-\frac{P\cdot F}{D_0}\right)^{\frac{1}{P}}, \quad \text{(A5)}$$

The bulk distribution coefficient, D_{bulk}, changes during partial melting, because the mineral modes M_j change as a function of melt fraction *F*

$$D_{bulk} = \sum\left(Kd^{j/l}\cdot M_j\right), \quad \text{(A6)}$$

and

$$M_j = M_{0,j} \cdot (1 - X) + X \cdot p_j \,, \tag{A7}$$

Critical melting (MAALOE, 1982) is a more sophisticated melting model, which accounts for a small residual melt porosity α. The rationale behind this melt porosity is that 'critical' melt fractions cannot be segregated perfectly from the peridotite, but are retained on the grain boundaries or in interstices. At melt fractions below the residual melt porosity, the system is closed and compositions of melt and residue can be described by batch (equilibrium) melting equations (SHAW, 1970). Only when the melt fraction exceed the residual melt porosity, a melt fraction of (F-α) is extracted from the residual solid and the residual interstitial melt. The melt phase retained in these pores buffers the LREE budget of the residue at high melt fractions. The exact solution has been described for the liquid composition in two steps by SOBOLEV and SHIMIZU (1992). The solid residue can be described as follows:

For $0 \leq F < \alpha/(\alpha+1)$

$$C_{wr} = \left(\frac{D_0 - P \cdot F}{1 - F} \right) \cdot \left(\frac{C_0}{D_0 + F \cdot (1 - P)} \right) \tag{A8}$$

And for $F \geq \alpha/(\alpha+1)$

$$C_{wr} = \left(\frac{D_0 - P \cdot F}{1 - F} \right) \cdot \left(\frac{C_0}{D_0 + (1 - P) \cdot \frac{\alpha}{\alpha + 1}} \right) \cdot \left[\frac{(D_0 + \alpha) - (P + \alpha) \cdot F}{(D_0 + \alpha) - (P + \alpha) \cdot \frac{\alpha}{\alpha + 1}} \right]^{\frac{1-P}{P+\alpha}} \tag{A9}$$

These equations for critical melting were solved numerically applying the CMELT program developed by Dr. G. Suhr.

Appendix B: Melt entrapment modeling

The chemical effect of melt entrapment on a residual peridotite, as discussed in *Chapter 2* is derived in four simple steps:

First, the new whole rock composition after linear mixing is calculated.

$$C_{wr} = C_0 \cdot (1 - X) + C_l \cdot X \ , \tag{B1}$$

where X is the melt fraction added to the residual peridotite, and C_{wr} and C_0 are the new and initial whole rock compositions, respectively. After addition of a melt with concentration C_l, trace elements are redistributed, assuming that newly formed minerals that crystallized from the melt attain equilibrium with preexisting phases of the peridotite. The new mode M of phase j can be expressed as a function of X:

$$M_j = M_0 \cdot (1 - X) + X \cdot Z_j \ , \tag{B2}$$

where Z_j is the crystallization mode. This crystallization mode describes the proportions of new minerals that crystallize from the melt. For the model presented in Fig. 7, Z_{ol} and Z_{cpx} were 0.7 and 0.3, respectively (ELTHON, 1992). Using these new mineral modes, the new bulk distribution coefficient, D_{bulk}, can be calculated:

$$D_{bulk} = \sum \left(Kd^{\,j/l} \cdot M_j \right), \tag{B3}$$

The concentration in the reequilibrated cpx after melt addition depends on the modified bulk distribution coefficient and is identical to equation A4.

Appendix C: The strontium problem

Strontium is a very useful trace element for geochemists. It is sensitive to the presence of plagioclase in magmatic processes, because of its compatibility in plagioclase. This compatible behavior will produce a positive Sr-anomaly in plagioclase, which means that Sr is strongly enriched in plagioclase with respect to the neighbouring REE (Ce and Nd) on an extended trace element diagram. Recently, positive Sr-anomalies in melt inclusions in olivine phenocrysts from Hawaiian lavas were interpreted as evidence for recycled lower oceanic crust (SOBOLEV ET AL., 2000). Lower crustal cumulates are plagioclase-rich and therefore have a positive Sr-anomaly.

Recent partitioning experiments have raised some doubts about these interpretations (BLUNDY ET AL., 2000). The partitioning behavior of divalent Sr is different to that of the trivalent REE. Whereas $Kd^{cpx/l}$ of the REE strongly vary with pressure, temperature and composition, $Kd^{cpx/l}$ of Sr remains relatively constant and appears to behave independently from these variables. This results in a negative Sr-anomaly in the Kd-pattern of high-pressure cpx and a positive Sr-anomaly at low pressures (BLUNDY ET AL., 2000).

For these reasons, accurate analysis of Sr by ion probe is a highly desirable goal. At present, strontium is routinely measured by ion probe analysis. However, Sr concentrations in cpx of abyssal peridotites have not been given much attention. In Fig. C1a, the chondrite-normalized Sr concentrations in cpx are plotted versus Nd for Central Indian Ridge peridotite and samples from other locations (DICK and NATLAND, 1996; JOHNSON and DICK, 1992; JOHNSON ET AL., 1990; ROSS and ELTHON, 1997). Also shown in Fig. A1a is a perfect fractional melting curve in one percent increments up to 15% melting. This melting curve was calculated following the procedures described in *Appendix A*. Towards low Nd concentrations, most samples have higher Sr than predicted by melting and the total variation in Sr is much lower than expected. At low Nd concentrations, Sr appears not to go below 0.05 times chondritic (corresponding to 0.4 µg/g). This becomes clearer in Fig. C1b, where the chondrite-normalized Sr/Nd in cpx is plotted versus its Yb concentration. As Yb decreases with increasing degree of melting, Sr/Nd ratios increase. This suggests that Sr is more compatible than Nd. The calculated melting curve shows that the opposite should be true. Because of this unexpected behavior of Sr, we suspected that the measured Sr concentrations in depleted samples might suffer from molecular interferences.

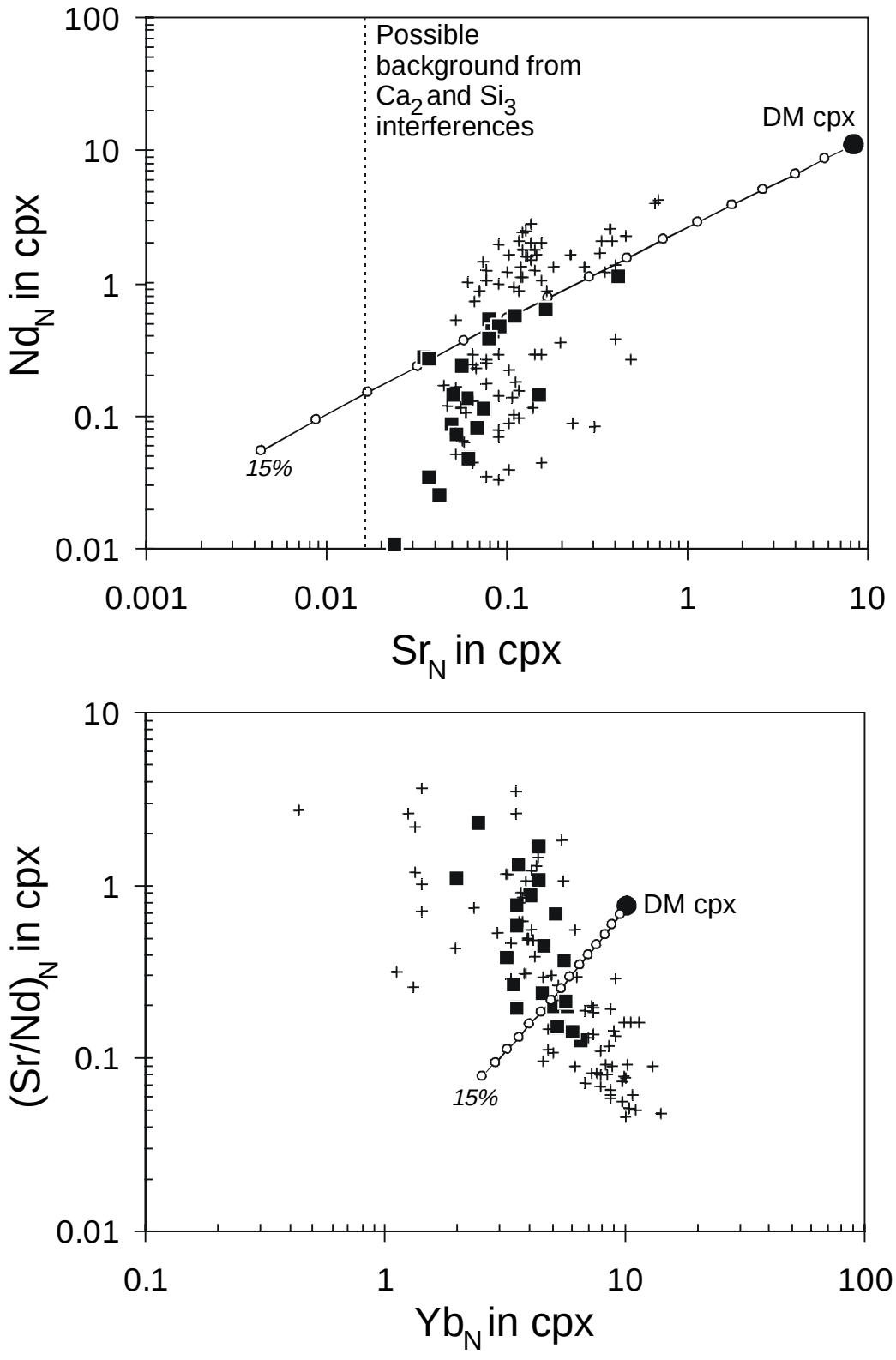

Fig C1: Chondrite-normalized cpx compositions (a) Nd vs Sr and (b) Sr/Nd vs Yb. Closed squares are CIR data, pluses from other mid-ocean ridges. Also shown fractional melting trajectory of a Depleted Mantle source in 1% increments. Sr appears to behave more incompatibly than Nd.

Ion probe analysis of Sr is determined on mass 88 (82.6 % isotopic abundance). Other interfering monovalent isobaric atoms are absent. Divalent interferences of mass 176 (Yb, Lu, and Hf with isotopic abundance of 12.7, 2.59, and 5.21% isotopic abundance, respectively) can be excluded, because of low absolute abundance and efficient energy filtering (Hoppe, pers. com.). Therefore, only molecules of very abundant major elements are not completely removed by the energy filtering technique (SHIMIZU ET AL., 1978).

Several combinations of major element molecules produce mass 88. Based on experience with molecular interferences on the REE, oxides commonly form interfering species. However, $^{72}Ge^{16}O$ is not believed to be abundant in the mantle and in mantle cpx. Diatomic molecules $^{44}Ca_2$ and $^{40}Ca^{48}Ti$ and triatomic molecules Si_3, $^{24}Mg_2{}^{40}Ca$, $^{23}Na_2{}^{42}Ca$, and FeO_2 are among the most likely to play a role. A rule of thumb predicts that triatomic molecules are much more likely, if not 'completely' removed by the energy offset. Experience has shown that this method is extremely efficient and there should not be any contribution of triatomic molecules (Hoppe, pers. com.). Since clinopyroxenes in abyssal peridotites have a virtually constant high calcium concentration (~21 wt.% CaO), we tested first if $^{44}Ca_2$ could be a candidate as an interfering molecule. For this purpose we first have to know the Ca_2^+/Ca^+ ratio. On standard glass NBS611 we measured the main calcium mass ^{40}Ca, the main Ca_2 molecule $^{80}Ca_2$. The $^{80}Ca_2/^{40}Ca$ ratio turned out to be much lower than expected: $3.4 \cdot 10^{-5}$.

In order to test if Ca_2 interferences occur in natural Sr-poor cpx, we selected a sample from the Central Indian Ridge on which we previously determined the lowest Sr concentration of the entire CIR sample set (ANTP89-5). In addition to the measurement of masses 40 and 80 determined on the NBS glass, we also measured the Sr masses: ^{86}Sr, ^{87}Sr (and ^{87}Rb), and ^{88}Sr. The $^{80}Ca_2/^{40}Ca$ ratio obtained on this cpx is higher than in the NBS standard: $8.6 \cdot 10^{-5}$. Considering that the average $^{80}Ca_2/^{30}Si$ is $3.05 \cdot 10^{-3}$, and the theoretical $^{88}Ca_2/^{80}Ca$ ratio is 0.004, we calculate a $^{88}Ca_2/^{30}Si$ ratio of $1.22 \cdot 10^{-5}$. The measured mass 88 to ^{30}Si rato is $3.34 \cdot 10^{-5}$. That means that for this low Sr cpx the contribution of Ca_2 on mass 88 is 36%! If Ca_2 is the only overlapping molecule, then the real concentration of Sr in this sample is 0.16 µg/g instead of 0.25 µg/g.

Another possible candidate as an interfering molecule is Si_3. The main mass of this triatomic molecule is 84 (78.4% theoretical abundance). The probability of Si_3 with a mass of 88 is 0.29%, which would give a theoretical $^{88}Si_3/^{84}Si_3$ of 0.00365. If we add mass 84

and repeat the analysis on the same sample we obtain 84/^{30}Si and 88/^{30}Si ratios of 1.18E-3 and 3.04E-5, respectively. The theoretical contribution of Si on mass 88 should then be $^{88}Si_3/^{84}Si_3$ times 84/^{30}Si: 4.31E-6. That is 14% of the total 88 mass, provided that no other mass then Si_3 lies on mass 84.

To summarize these simple tests: for this Sr-depleted cpx, the uncorrected Sr concentration would be 0.25 µg/g. But despite the rigorous energy filtering, molecular major element species appear to cause problematic interferences, which add up to 50% of the total concentration. Approximately 36% of this total concentration is contributed from Ca_2 and 14% from Si_3. Given that in a cpx matrix calcium and silicon have more or less constant concentrations, the constant 'background' because of their interference would be 0.12 µg/g. The reported values have not been corrected for these interferences, because the data were collected before any need for such a correction was identified.

However, if these calculated Ca_2 and Si_3 interferences are real, they are insufficient to explain the only small variation in Sr concentration observed in many (Sr-poor) cpx (Fig. C1a). It remains possible that the observed concentrations are real and suggest that Sr does not behave similarly to the REE during melting. Kinetic processes, as suspected to play a role for the fast-diffusing element sodium, cannot be excluded with the currently available data (see *Chapter 2*, Section 'Melt entrapment'). Nevertheless, sub-ppm Sr concentrations must be taken with caution.

References

Blundy J., Robinson J. A. C., and Wood B. (2000) Heavy REE are compatible in clinopyroxene on the spinel lherzolite solidus. *J. Conf. Abstr.* **5**(2), 219.

Dick H. J. B. and Natland J. H. (1996) Late-stage melt evolution and transport in the shallow mantle beneath the East Pacific Rise. *Proc. ODP, Sci. Res.* **147**, 103-134.

Johnson K. T. M. and Dick H. J. B. (1992) Open system melting and temporal and spatial variation of peridotite and basalt at the Atlantis II fracture zone. *J. Geophys. Res.* **97**, 9219-9241.

Johnson K. T. M., Dick H. J. B., and Shimizu N. (1990) Melting in the oceanic upper mantle; an ion microprobe study of diopsides in abyssal peridotites. *J. Geophys. Res.* **95**, 2661-2678.

Ross K. and Elthon D. (1997) Extreme incompatible trace-element depletion of diopside in residual mantle from south of the Kane F.Z. *Proc. ODP, Sci. Res.* **153**, 277-284.

Shimizu N., Semet M. P., and Allegre J. C. (1978) Geochemical applications of quantitative ion microprobe analysis. *Geochim. Cosmochim. Acta* **42**, 1321-1334.

Sobolev A. V., Hofmann A. W., and Nikogosian I. K. (2000) Recycled oceanic crust observed in 'ghost plagioclase' within the source of Mauna Loa lavas. *Nature* **404**, 986-990.

Appendix D: Electron microprobe data

Table D1: Spinel analyses

Sample	File	An#	Ngr	Nan	TiO2	Al2O3	Cr2O3	FeO*	MgO	MnO	NiO	Total	Mg#	Cr#
ANTP134-3	6	32	1	1	**0.03**	**43.52**	**24.58**	**14.28**	**17.89**	**0.13**	**0.21**	**100.64**	**0.734**	**0.275**
ANTP134-5														
s134-5_4-1	5	33			0.07	41.54	27.62	12.85	18.38	0.14	0.21	100.81	0.757	0.308
s134-5_4-2	5	34			0.08	41.31	27.44	13.08	18.52	0.13	0.21	100.77	0.762	0.308
avg			1	2	**0.07**	**41.43**	**27.53**	**12.97**	**18.45**	**0.14**	**0.21**	**100.79**	**0.759**	**0.308**
ANTP134-7														
s134-7_1-1	13	1			0.07	41.28	28.11	12.11	18.67	0.12	0.24	100.60	0.770	0.314
s134-7_1-2	13	2			0.09	41.21	28.18	12.50	18.35	0.14	0.24	100.71	0.757	0.314
s134-7_1-4	13	4			0.05	40.04	29.79	12.40	18.34	0.14	0.24	101.00	0.759	0.333
avg			1	3	**0.07**	**40.84**	**28.69**	**12.34**	**18.45**	**0.13**	**0.24**	**100.77**	**0.762**	**0.320**
sd					*0.02*	*0.70*	*0.95*	*0.20*	*0.19*	*0.01*	*0.00*	*0.19*	*0.007*	*0.011*
rel. sd					0.25	0.02	0.03	0.02	0.01	0.08	0.01	0.00	0.009	0.034
ANTP134-8														
s134-8_3-1	8	6			0.07	42.59	26.39	12.49	18.49	0.16	0.24	100.43	0.761	0.294
s134-8_3-2	8	7			0.09	42.16	27.26	12.30	18.30	0.17	0.22	100.49	0.755	0.303
avg			1	2	**0.08**	**42.38**	**26.83**	**12.40**	**18.40**	**0.16**	**0.23**	**100.46**	**0.758**	**0.298**
Circe93-2														
s93-2a_1-1	10	88			0.11	41.70	27.21	13.11	17.92	0.18	0.18	100.41	0.744	0.304
s93-2a_5-1	10	99			0.12	38.42	31.12	13.32	17.39	0.18	0.15	100.70	0.729	0.352
s93-2a_5-2	10	100			0.09	38.23	31.45	13.41	17.44	0.16	0.16	100.94	0.729	0.356
s93-2a_5-3	10	101			0.09	37.83	31.83	13.30	17.35	0.21	0.14	100.74	0.731	0.361
s93-2a_6-1	10	105			0.07	42.50	26.80	12.56	18.14	0.15	0.18	100.41	0.749	0.297
s93-2a_6-2	10	106			0.12	43.02	26.48	12.44	18.56	0.16	0.19	100.97	0.762	0.292
s93-2a_6-3	10	107			0.09	40.79	28.84	12.93	17.93	0.16	0.18	100.93	0.742	0.322
s93-2b_1-1	7	28			0.09	41.58	28.41	12.44	18.69	0.15	0.21	101.57	0.764	0.314
s93-2b_1-2	7	29			0.11	41.64	28.18	12.46	18.57	0.12	0.19	101.27	0.760	0.312
s93-2b_1-3	7	30			0.10	41.34	28.34	12.47	18.66	0.15	0.17	101.23	0.765	0.315
avg			4	10	**0.10**	**40.71**	**28.87**	**12.84**	**18.07**	**0.16**	**0.18**	**100.92**	**0.747**	**0.323**
sd					*0.02*	*1.86*	*1.95*	*0.41*	*0.54*	*0.02*	*0.02*	*0.37*	*0.015*	*0.025*
rel. sd					0.16	0.05	0.07	0.03	0.03	0.14	0.13	0.00	0.019	0.077
Circe93-3														
s93-3a_3-1	9	5			0.13	35.73	34.18	13.88	17.01	0.20	0.16	101.29	0.718	0.391
s93-3a_3-2	9	6			0.12	36.45	33.01	13.70	16.95	0.23	0.16	100.61	0.718	0.378
s93-3a_4-1	9	9			0.13	33.74	36.37	13.89	16.82	0.20	0.13	101.29	0.716	0.420
s93-3a_4-2	9	10			0.13	33.89	36.25	13.74	17.01	0.16	0.12	101.30	0.724	0.418
s93-3b_3-1	9	23			0.13	37.06	32.52	14.03	17.07	0.16	0.16	101.13	0.718	0.371
avg			3	5	**0.13**	**35.37**	**34.47**	**13.85**	**16.97**	**0.19**	**0.15**	**101.13**	**0.719**	**0.395**
sd					*0.01*	*1.50*	*1.79*	*0.13*	*0.09*	*0.03*	*0.02*	*0.31*	*0.003*	*0.023*
rel. sd					0.06	0.04	0.05	0.01	0.01	0.16	0.11	0.00	0.004	0.057
Circe93-4														
s93-4_2-1	6	71			0.05	41.52	27.46	12.57	18.53	0.14	0.21	100.48	0.766	0.307
s93-4_2-2	6	72			0.06	41.68	27.23	12.69	18.46	0.17	0.21	100.49	0.762	0.305
s93-4_2-3	6	73			0.07	41.85	27.33	12.71	18.54	0.14	0.22	100.85	0.762	0.305
avg			1	3	**0.06**	**41.68**	**27.34**	**12.66**	**18.51**	**0.15**	**0.21**	**100.61**	**0.763**	**0.306**
sd					*0.01*	*0.17*	*0.12*	*0.08*	*0.04*	*0.01*	*0.00*	*0.20*	*0.002*	*0.002*
rel. sd					0.15	0.00	0.00	0.01	0.00	0.09	0.02	0.00	0.003	0.005
Circe93-5														
s93-5a_2-1	12	34			0.06	28.54	41.26	14.71	16.42	0.21	0.11	101.32	0.715	0.492
s93-5a_2-2	12	35			0.10	28.54	41.63	14.55	16.34	0.22	0.12	101.49	0.710	0.495
s93-5a_3-1	12	36			0.09	23.16	46.32	17.43	14.41	0.28	0.08	101.76	0.649	0.573
s93-5a_3-2	12	37			0.10	23.26	46.21	17.24	14.34	0.23	0.07	101.45	0.646	0.571
avg			2	4	**0.09**	**25.88**	**43.86**	**15.98**	**15.38**	**0.23**	**0.09**	**101.50**	**0.680**	**0.533**
sd					*0.02*	*3.08*	*2.79*	*1.57*	*1.16*	*0.03*	*0.02*	*0.24*	*0.038*	*0.045*
rel. sd					0.19	0.12	0.06	0.10	0.08	0.13	0.25	0.00	0.055	0.085

Table D1: Spinel analyses

Sample	File	An#	Ngr	Nan	TiO2	Al2O3	Cr2O3	FeO*	MgO	MnO	NiO	Total	Mg#	Cr#
Circe93-7														
s93-7a_3-1	29	13			0.05	35.11	34.24	14.83	16.59	0.22	0.14	101.18	0.706	0.395
s93-7a_3-2	29	14			0.04	35.22	33.84	14.94	16.44	0.17	0.15	100.80	0.703	0.392
s93-7b_1-1	29	21			0.08	37.61	32.26	13.00	17.65	0.17	0.12	100.89	0.739	0.365
s93-7b_1-2	29	22			0.04	36.33	33.34	13.41	17.45	0.19	0.14	100.89	0.736	0.381
s93-7b_2-1	29	27			0.02	33.68	35.89	13.84	17.11	0.21	0.14	100.89	0.732	0.417
s93-7b_2-2	29	28			0.04	33.77	36.32	13.57	16.95	0.23	0.20	101.08	0.725	0.419
avg			3	6	**0.04**	**35.29**	**34.32**	**13.93**	**17.03**	**0.20**	**0.15**	**100.95**	**0.724**	**0.395**
sd					*0.02*	*1.51*	*1.54*	*0.79*	*0.47*	*0.02*	*0.03*	*0.17*	*0.015*	*0.021*
rel. sd					0.45	0.04	0.04	0.06	0.03	0.13	0.19	0.00	0.021	0.052
ANTP126-2														
s126-2_2-1	6	46			0.01	48.07	20.72	11.00	19.98	0.14	0.27	100.19	0.802	0.224
s126-2_2-2	6	47			0.00	48.24	20.77	11.19	20.10	0.09	0.28	100.67	0.803	0.224
s126-2_2b1	6	54			0.03	48.35	20.51	10.96	19.95	0.15	0.28	100.23	0.800	0.222
s126-2_2b2	6	55			0.05	48.12	20.82	11.23	20.04	0.13	0.27	100.66	0.799	0.225
s126-2_4-1	6	66			0.02	48.65	19.98	11.17	19.77	0.10	0.26	99.95	0.795	0.216
s126-2_4-2	6	67			0.04	48.54	19.91	11.14	19.91	0.16	0.26	99.95	0.799	0.216
avg			3	6	**0.02**	**48.33**	**20.45**	**11.12**	**19.96**	**0.13**	**0.27**	**100.28**	**0.800**	**0.221**
sd					*0.02*	*0.23*	*0.41*	*0.11*	*0.11*	*0.03*	*0.01*	*0.33*	*0.003*	*0.004*
rel. sd					0.77	0.00	0.02	0.01	0.01	0.22	0.04	0.00	0.003	0.019
ANTP126-5														
s126-5_3-1	5	20			0.03	48.63	20.41	10.97	19.87	0.12	0.27	100.30	0.796	0.220
s126-5_3-2	5	21			0.02	48.36	20.46	10.99	19.90	0.12	0.28	100.13	0.798	0.221
avg			1	2	**0.02**	**48.50**	**20.44**	**10.98**	**19.89**	**0.12**	**0.27**	**100.21**	**0.797**	**0.220**
ANTP126-D5														
s126-d5a_4-1	10	60			0.03	48.25	20.66	11.75	19.22	0.13	0.25	100.29	0.773	0.223
s126-d5a_7-1	10	72			0.04	48.59	20.57	10.92	19.91	0.13	0.28	100.44	0.798	0.221
s126-d5a_7-2	10	73			0.02	48.49	20.39	10.79	20.05	0.12	0.27	100.13	0.802	0.220
s126-d5a_7-3	10	74			0.06	48.62	20.63	11.02	20.01	0.15	0.27	100.76	0.798	0.222
s126-d5a_7-4	10	75			0.05	48.73	20.47	10.91	20.09	0.09	0.28	100.61	0.801	0.220
s126-d5a_7-5	10	76			0.04	48.63	20.47	10.77	19.80	0.06	0.27	100.05	0.795	0.220
avg			3	6	**0.04**	**48.55**	**20.53**	**11.03**	**19.85**	**0.11**	**0.27**	**100.38**	**0.795**	**0.221**
sd					*0.01*	*0.17*	*0.11*	*0.37*	*0.32*	*0.03*	*0.01*	*0.28*	*0.011*	*0.001*
rel. sd					0.37	0.00	0.01	0.03	0.02	0.28	0.04	0.00	0.014	0.006
ANTP84-11														
s84-11_4-1	24	31			0.00	39.15	29.34	14.45	18.05	0.17	0.21	101.36	0.749	0.335
s84-11_4-2	24	32			0.02	39.23	29.39	14.60	18.05	0.17	0.22	101.68	0.747	0.334
s84-11_4-3	24	33			0.01	39.14	29.48	14.51	18.13	0.16	0.19	101.62	0.750	0.336
avg			1	3	**0.01**	**39.17**	**29.40**	**14.52**	**18.08**	**0.17**	**0.20**	**101.55**	**0.749**	**0.335**
sd					*0.01*	*0.05*	*0.07*	*0.08*	*0.05*	*0.01*	*0.01*	*0.17*	*0.001*	*0.001*
rel. sd					0.87	0.00	0.00	0.01	0.00	0.06	0.07	0.00	0.002	0.002
ANTP87-5														
s87-5a_3-1	16	9			0.03	40.07	27.31	15.75	17.82	0.19	0.24	101.40	0.739	0.314
s87-5a_3-2	16	10			0.01	40.16	27.46	15.73	18.05	0.20	0.22	101.83	0.743	0.314
s87-5a_3-3	16	11			0.02	39.57	28.07	16.08	17.58	0.18	0.19	101.70	0.729	0.322
avg			1	3	**0.02**	**39.93**	**27.61**	**15.85**	**17.82**	**0.19**	**0.22**	**101.64**	**0.737**	**0.317**
sd					*0.01*	*0.32*	*0.40*	*0.20*	*0.24*	*0.01*	*0.02*	*0.20*	*0.008*	*0.005*
rel. sd					0.31	0.01	0.01	0.01	0.01	0.04	0.11	0.00	0.010	0.015
ANTP87-9														
s87-9_1-1	23	34			0.04	35.26	31.85	16.92	17.38	0.16	0.23	101.84	0.730	0.377
s87-9_1-2	23	35			0.03	33.82	33.20	17.18	17.28	0.16	0.22	101.90	0.729	0.397
s87-9_1-3	23	36			0.04	33.81	33.26	17.12	17.11	0.17	0.21	101.71	0.725	0.398
s87-9_2-1	23	37			0.04	35.19	31.20	18.13	16.56	0.19	0.18	101.49	0.703	0.373
s87-9_4-1	23	44			0.07	34.15	32.06	18.16	16.92	0.20	0.21	101.76	0.715	0.386
s87-9_4-2	23	45			0.05	35.09	31.36	17.50	17.18	0.19	0.23	101.60	0.725	0.375
avg			3	6	**0.04**	**34.55**	**32.16**	**17.50**	**17.07**	**0.18**	**0.21**	**101.72**	**0.721**	**0.384**
sd					*0.01*	*0.70*	*0.89*	*0.53*	*0.30*	*0.02*	*0.02*	*0.14*	*0.011*	*0.011*
rel. sd					0.29	0.02	0.03	0.03	0.02	0.09	0.09	0.00	0.015	0.029

Table D1: Spinel analyses

Sample	File	An#	Ngr	Nan	TiO2	Al2O3	Cr2O3	FeO*	MgO	MnO	NiO	Total	Mg#	Cr#
ANTP89-1														
s89-1_3-1	17	27			0.06	43.66	25.84	12.68	18.93	0.17	0.23	101.57	0.768	0.284
s89-1_3-1	19	13			0.07	43.22	26.18	12.55	19.09	0.16	0.24	101.51	0.775	0.289
s89-1_3-2	19	14			0.10	43.27	25.93	12.84	19.24	0.13	0.25	101.76	0.778	0.287
s89-1_3-2	17	28			0.06	43.37	25.76	12.68	18.90	0.13	0.24	101.14	0.769	0.285
s89-1_3-3	19	15			0.07	43.04	26.19	12.61	19.22	0.17	0.26	101.56	0.780	0.290
s89-1_3-3	17	29			0.06	43.26	26.15	12.52	19.17	0.12	0.23	101.51	0.777	0.289
avg			2	6	**0.07**	**43.30**	**26.01**	**12.65**	**19.09**	**0.15**	**0.24**	**101.51**	**0.775**	**0.287**
sd					*0.01*	*0.21*	*0.19*	*0.12*	*0.15*	*0.02*	*0.01*	*0.21*	*0.005*	*0.002*
rel. sd					0.20	0.00	0.01	0.01	0.01	0.15	0.05	0.00	0.006	0.008
ANTP89-2 (1)														
s89-2_1-1	28	1			0.05	44.81	23.89	14.78	17.80	0.14	0.25	101.72	0.723	0.263
s89-2_1-2	28	2			0.03	44.90	23.87	14.82	18.09	0.18	0.20	102.09	0.732	0.263
s89-2_3-1	28	3			0.03	45.29	23.76	13.13	19.05	0.14	0.25	101.65	0.767	0.260
s89-2_3-2	28	4			0.03	45.79	22.74	13.68	18.76	0.17	0.23	101.40	0.757	0.250
avg			2	4	**0.04**	**45.20**	**23.57**	**14.10**	**18.43**	**0.15**	**0.23**	**101.72**	**0.745**	**0.259**
sd					*0.01*	*0.45*	*0.55*	*0.84*	*0.58*	*0.02*	*0.02*	*0.30*	*0.021*	*0.006*
rel. sd					0.27	0.01	0.02	0.06	0.03	0.13	0.10	0.00	0.028	0.024
ANTP89-2 (2)														
s89-2_5-1	28	20			0.19	27.27	41.36	18.41	14.68	0.24	0.09	102.24	0.642	0.504
s89-2_5-2	28	21			0.17	29.22	39.70	17.85	15.16	0.27	0.07	102.44	0.659	0.477
s89-2_5-3	28	22			0.17	28.67	40.03	18.25	14.93	0.26	0.10	102.41	0.648	0.484
avg			1	**3**	**0.18**	**28.39**	**40.36**	**18.17**	**14.92**	**0.26**	**0.09**	**102.36**	**0.650**	**0.488**
sd					*0.02*	*1.01*	*0.88*	*0.29*	*0.24*	*0.01*	*0.02*	*0.14*	*0.009*	*0.014*
rel. sd					0.09	0.04	0.02	0.02	0.02	0.05	0.19	0.00	0.014	0.029
ANTP89-5														
s89-5_2-1	21	91			0.03	52.52	15.54	12.83	19.93	0.14	0.33	101.32	0.783	0.166
s89-5_2-2	21	92			0.04	50.68	17.03	13.81	19.39	0.16	0.30	101.41	0.767	0.184
avg			1	2	**0.04**	**51.60**	**16.29**	**13.32**	**19.66**	**0.15**	**0.31**	**101.36**	**0.775**	**0.175**
ANTP89-8														
s89-8_2-1	26	11			0.02	50.63	18.31	12.28	19.90	0.14	0.30	101.57	0.785	0.195
s89-8_2-2	26	12			0.02	50.63	18.43	12.38	19.94	0.16	0.29	101.84	0.785	0.196
s89-8_4-1	26	15			0.00	49.41	19.34	12.79	19.76	0.17	0.30	101.77	0.782	0.208
s89-8_4-2	26	16			0.01	49.44	19.25	12.76	19.73	0.14	0.28	101.61	0.781	0.207
avg			2	4	**0.01**	**50.03**	**18.83**	**12.55**	**19.83**	**0.15**	**0.29**	**101.70**	**0.783**	**0.202**
sd					*0.01*	*0.70*	*0.54*	*0.26*	*0.10*	*0.02*	*0.01*	*0.13*	*0.002*	*0.007*
rel. sd					0.72	0.01	0.03	0.02	0.01	0.11	0.03	0.00	0.002	0.034
ANTP89-15														
s89-15a_1-1	25	1			0.07	43.78	25.59	12.77	19.13	0.15	0.22	101.70	0.774	0.282
s89-15a_1-2	25	2			0.06	43.96	25.64	12.99	19.19	0.17	0.25	102.25	0.772	0.281
s89-15a_1-3	25	3			0.05	43.85	25.34	12.94	19.09	0.17	0.24	101.68	0.773	0.279
s89-15b_1-1	27	8			0.07	42.61	26.92	12.62	19.42	0.13	0.25	102.02	0.785	0.298
s89-15b_1-2	27	9			0.08	42.74	26.93	12.76	19.59	0.16	0.22	102.47	0.789	0.297
s89-15b_1-3	27	10			0.07	42.52	27.03	13.01	19.18	0.16	0.24	102.20	0.777	0.299
s89-15b_1-4	27	11			0.08	43.13	26.59	12.72	19.36	0.13	0.28	102.29	0.780	0.293
s89-15b_3-1	27	19			0.08	42.81	26.75	13.19	19.11	0.16	0.22	102.32	0.771	0.295
s89-15b_3-2	27	20			0.05	42.68	26.47	13.07	19.17	0.17	0.22	101.83	0.777	0.294
avg			3	9	**0.07**	**43.12**	**26.36**	**12.90**	**19.25**	**0.15**	**0.24**	**102.09**	**0.778**	**0.291**
sd					*0.01*	*0.58*	*0.66*	*0.19*	*0.17*	*0.02*	*0.02*	*0.30*	*0.006*	*0.008*
rel. sd					0.16	0.01	0.02	0.01	0.01	0.10	0.09	0.00	0.008	0.027
ANTP89-17														
s89-17_3-1	helle25	31			0.02	43.90	25.43	13.68	18.08	0.18	0.18	101.47	0.737	0.280
s89-17_3-2	helle25	32			0.02	44.03	25.53	13.97	18.19	0.14	0.19	102.08	0.737	0.280
s89-17_5a1	helle25	38			0.04	43.34	26.05	13.67	18.54	0.19	0.18	102.01	0.752	0.287
s89-17_5b1	helle25	39			0.03	43.31	25.77	13.66	18.05	0.13	0.18	101.14	0.738	0.285
s89-17_5b2	helle25	40			0.01	43.79	25.43	13.59	17.98	0.19	0.17	101.17	0.738	0.280
avg			2	5	**0.03**	**43.67**	**25.64**	**13.71**	**18.17**	**0.17**	**0.18**	**101.57**	**0.740**	**0.283**
sd					*0.01*	*0.33*	*0.27*	*0.15*	*0.22*	*0.03*	*0.01*	*0.46*	*0.006*	*0.003*
rel. sd					0.45	0.01	0.01	0.01	0.01	0.16	0.04	0.00	0.009	0.012

Table D1: Spinel analyses

Sample	File	An#	Ngr	Nan	TiO2	Al2O3	Cr2O3	FeO*	MgO	MnO	NiO	Total	Mg#	Cr#
60GTV														
s60-5_3-1	12	29			0.08	35.86	33.21	14.49	17.17	0.19	0.18	101.17	0.727	0.383
s60-5_3-2	12	30			0.10	35.98	33.09	14.72	17.07	0.17	0.18	101.31	0.720	0.382
s60-5_3-3	12	31			0.10	36.00	33.32	14.56	17.07	0.15	0.17	101.36	0.719	0.383
avg			1	3	**0.09**	**35.95**	**33.21**	**14.59**	**17.10**	**0.17**	**0.17**	**101.28**	**0.722**	**0.383**
sd					*0.01*	*0.08*	*0.12*	*0.12*	*0.06*	*0.02*	*0.01*	*0.06*	*0.004*	*0.001*
rel. sd					0.16	0.00	0.00	0.01	0.00	0.13	0.04	0.00	0.006	0.002
31GTV														
s31a_2-1	4	1			0.03	35.64	32.04	15.16	16.52	0.17	0.18	99.74	0.710	0.376
s31a_2-2	4	2			0.08	35.51	32.10	15.33	16.42	0.22	0.17	99.82	0.705	0.377
avg			1	2	**0.05**	**35.58**	**32.07**	**15.25**	**16.47**	**0.19**	**0.17**	**99.78**	**0.708**	**0.377**

Clinopyroxene and orthopyroxene analyses are grouped, depending on textures, grainsize and, for coarse grains, position within an individual grain:

P	Porphyroclast
RX	Medium- to coarse-grained (> ~100 µm) recrystallized aggregate
fXR	Fine-grained recrystallized aggregate (< ~100 µm on average)
Tw	Magmatic twin
i	intergranular (films, interstitial)
XS	Exsolution (mostly granular, or bleb, in opx)

The indices c and r denote 'core' and 'rim', so P-c = porphyroclast core, etc…

Table D2: Cpx analyses

Sample	File	An#	Text.	SiO2	TiO2	Al2O3	Cr2O3	FeO	MgO	MnO	CaO	NiO	Na2O	K2O	Total	Mg#
ANTP134-3																
c134-3_1a1	6	1	P-c	50.88	0.13	5.19	1.52	2.35	15.91	0.11	22.48	0.03	0.59	0.00	99.19	0.923
c134-3-1b1	6	2	fRX	51.38	0.17	4.55	1.38	2.21	16.30	0.10	22.58	0.05	0.46	0.00	99.18	0.929
c134-3-1b2	6	3	fRX	51.64	0.14	4.42	1.45	2.80	18.50	0.12	19.87	0.05	0.42	0.00	99.40	0.922
c134-3_2-1	6	5	RX-r	51.94	0.14	3.81	1.24	2.18	16.55	0.08	22.54	0.05	0.45	0.01	98.98	0.931
c134-3_2-2	6	6	RX-r	51.22	0.13	4.72	1.27	2.59	17.14	0.09	21.46	0.04	0.44	0.02	99.11	0.922
c134-3_2-3	6	7	RX-r	51.55	0.15	4.70	1.29	2.46	17.08	0.05	21.18	0.05	0.50	0.00	99.01	0.925
c134-3_2-4	6	8	RX-r	51.53	0.15	4.63	1.42	2.44	16.27	0.10	22.42	0.04	0.53	0.02	99.55	0.922
c134-3_2-5	6	9	RX-r	51.53	0.15	4.03	1.48	2.19	16.09	0.09	22.97	0.03	0.48	0.01	99.04	0.929
c134-3_2-6	6	10	RX-c	51.01	0.15	5.10	1.51	2.32	15.84	0.08	22.73	0.04	0.55	0.01	99.34	0.924
c134-3_2-7	6	11	RX-c	51.12	0.11	5.12	1.44	2.63	16.08	0.08	21.91	0.05	0.65	0.00	99.18	0.916
c134-3_2-8	6	12	RX-c	51.39	0.12	4.99	1.46	2.36	15.83	0.10	22.16	0.06	0.54	0.02	99.03	0.923
c134-3_4-1	6	26	Tw-r	52.14	0.14	3.86	1.20	2.11	16.43	0.05	23.02	0.04	0.43	0.01	99.44	0.933
c134-3_4-2	6	27	Tw-c	51.47	0.10	4.76	1.43	2.27	15.95	0.10	22.09	0.05	0.59	0.00	98.81	0.926
c134-3_4-3	6	28	Tw-r	51.73	0.16	4.19	1.18	2.16	16.19	0.10	22.75	0.04	0.40	0.02	98.92	0.930
c134-3_4-5	6	30	Tw-r	51.55	0.13	4.41	1.23	2.24	16.10	0.08	22.67	0.04	0.50	0.02	98.97	0.928
ave-all			**15**	**51.47**	**0.14**	**4.57**	**1.37**	**2.35**	**16.42**	**0.09**	**22.19**	**0.04**	**0.50**	**0.01**	**99.14**	**0.926**
sd				*0.33*	*0.02*	*0.45*	*0.12*	*0.20*	*0.70*	*0.02*	*0.83*	*0.01*	*0.07*	*0.01*	*0.21*	*0.00*
rel. sd				0.01	0.13	0.10	0.09	0.08	0.04	0.22	0.04	0.19	0.14	1.01	0.00	0.00
ave-tw			**4**	**51.72**	**0.13**	**4.31**	**1.26**	**2.20**	**16.17**	**0.08**	**22.63**	**0.04**	**0.48**	**0.01**	**99.04**	**0.929**
sd				*0.30*	*0.03*	*0.38*	*0.12*	*0.07*	*0.20*	*0.02*	*0.39*	*0.00*	*0.08*	*0.01*	*0.28*	*0.00*
rel. sd				0.01	0.19	0.09	0.09	0.03	0.01	0.29	0.02	0.09	0.17	0.79	0.00	0.00
ANTP134-4 (@40 mm from vein)																
c134-4_1-1	8	16	P-c	51.52	0.12	5.11	1.42	2.19	16.29	0.09	22.06	0.03	0.70	0.02	99.55	0.930
c134-4_1-3	8	20	RX-c	51.21	0.12	5.19	1.41	2.57	16.42	0.07	21.68	0.06	0.64	0.01	99.39	0.919
c134-4_1-4	8	21	RX-c	51.34	0.13	5.05	1.39	2.58	17.34	0.07	20.86	0.04	0.65	0.01	99.46	0.923
c134-4_1-5	8	22	RX-r	51.37	0.14	4.87	1.45	2.10	16.10	0.09	22.65	0.03	0.62	0.00	99.42	0.932
c134-4_1-6	8	23	RX-r	51.57	0.13	4.73	1.43	2.14	16.09	0.10	22.66	0.05	0.55	0.01	99.45	0.931
c134-4_1-7	8	24	P-c	51.53	0.11	5.14	1.44	2.70	17.28	0.10	20.68	0.05	0.63	0.00	99.65	0.919
c134-4_1-8	8	25	P-c	50.40	0.10	5.25	1.57	2.88	17.00	0.10	20.70	0.05	0.69	0.00	98.74	0.913
ave-all			**7**	**51.28**	**0.12**	**5.05**	**1.44**	**2.45**	**16.65**	**0.09**	**21.61**	**0.04**	**0.64**	**0.01**	**99.38**	**0.924**
sd				*0.41*	*0.01*	*0.19*	*0.06*	*0.31*	*0.55*	*0.01*	*0.88*	*0.01*	*0.05*	*0.01*	*0.30*	*0.01*
rel. sd				0.01	0.11	0.04	0.04	0.13	0.03	0.13	0.04	0.26	0.08	1.07	0.00	0.01
ANTP134-5																
c134-5_1-1	5	24	RX-r	51.60	0.15	4.10	1.29	2.20	16.77	0.04	22.12	0.02	0.53	0.01	98.82	0.931
c134-5_1-3	5	26	RX-r	51.73	0.14	4.08	1.35	1.93	16.41	0.09	23.23	0.06	0.48	0.01	99.50	0.938
c134-5_1-4	5	27	RX-r	51.73	0.11	4.59	1.39	2.39	16.58	0.12	21.84	0.04	0.57	0.01	99.38	0.925
c134-5_1-5	5	28	RX-c	51.64	0.13	4.50	1.42	2.23	16.35	0.11	22.20	0.03	0.52	0.02	99.15	0.929
ave-all			**4**	**51.68**	**0.13**	**4.32**	**1.36**	**2.19**	**16.53**	**0.09**	**22.35**	**0.04**	**0.52**	**0.01**	**99.21**	**0.931**
sd				*0.07*	*0.02*	*0.27*	*0.06*	*0.19*	*0.19*	*0.04*	*0.61*	*0.02*	*0.04*	*0.00*	*0.30*	*0.01*
rel. sd				0.00	0.11	0.06	0.04	0.09	0.01	0.40	0.03	0.42	0.08	0.26	0.00	0.01
ANTP134-7																
c134-7_2-1	13	6	fRX	51.35	0.18	4.80	1.41	2.16	16.20	0.09	22.67	0.04	0.57	0.00	99.45	0.930
c134-7_2-2	13	7	fRX	51.66	0.17	4.23	1.44	1.94	16.36	0.10	23.11	0.03	0.63	0.00	99.67	0.938
c134-7_2-3	13	8	fRX	51.51	0.16	4.40	1.44	1.91	16.24	0.06	22.76	0.05	0.53	0.02	99.07	0.938
c134-7_2-4	13	9	fRX	51.39	0.14	4.84	1.30	2.21	16.60	0.07	21.56	0.04	0.63	0.00	98.78	0.930
c134-7_2-5	13	10	fRX	51.48	0.14	4.97	1.37	2.21	16.57	0.09	21.81	0.04	0.66	0.01	99.35	0.930
c134-7_3-1	13	11	P-r	51.52	0.15	4.50	1.37	2.18	16.48	0.07	22.26	0.05	0.63	0.01	99.21	0.931
c134-7_3-2	13	12	P-r	51.69	0.15	4.24	1.19	2.17	16.44	0.07	22.36	0.03	0.59	0.02	98.95	0.931
c134-7_3-3	13	13	P-r	52.08	0.14	4.25	1.20	2.23	16.64	0.08	21.91	0.06	0.56	0.02	99.17	0.930
c134-7_3-4	13	14	P-r	52.11	0.17	4.36	1.23	2.55	16.88	0.12	21.65	0.04	0.61	0.00	99.73	0.922
ave-all			**9**	**51.64**	**0.15**	**4.51**	**1.33**	**2.17**	**16.49**	**0.08**	**22.23**	**0.04**	**0.60**	**0.01**	**99.26**	**0.931**
sd				*0.28*	*0.01*	*0.29*	*0.10*	*0.18*	*0.21*	*0.02*	*0.54*	*0.01*	*0.04*	*0.01*	*0.32*	*0.00*
rel. sd				0.01	0.10	0.06	0.07	0.08	0.01	0.23	0.02	0.20	0.07	0.98	0.00	0.01
ANTP134-8																
c134-8_1-1	8	3	fRX	51.36	0.12	5.00	1.28	2.40	16.42	0.04	21.90	0.03	0.64	0.02	99.21	0.924
c134-8_4-5	8	14	fRX	51.22	0.13	4.96	1.34	1.98	15.67	0.08	22.54	0.04	0.65	0.00	98.60	0.934
c134-8_4-6	8	15	fRX	51.61	0.12	5.01	1.26	2.38	16.77	0.08	21.94	0.04	0.64	0.00	99.86	0.926
c134-8_4-1	8	10	P-c	51.14	0.09	5.25	1.52	2.51	16.11	0.06	21.59	0.03	0.61	0.00	98.92	0.920
c134-8_4-2	8	11	P-c	51.34	0.13	5.31	1.52	2.93	17.98	0.09	19.25	0.04	0.54	0.00	99.13	0.916
c134-8_4-4	8	13	P-c	50.84	0.11	5.55	1.57	2.53	15.86	0.09	21.79	0.06	0.68	0.01	99.08	0.918
ave-n			**3**	**51.40**	**0.12**	**4.99**	**1.29**	**2.25**	**16.29**	**0.07**	**22.13**	**0.04**	**0.64**	**0.01**	**99.22**	**0.928**
sd				*0.20*	*0.01*	*0.03*	*0.04*	*0.24*	*0.56*	*0.02*	*0.36*	*0.01*	*0.00*	*0.01*	*0.63*	*0.01*
rel. sd				0.00	0.06	0.01	0.03	0.11	0.03	0.31	0.02	0.14	0.00	1.73	0.01	0.01
ave-P-c			**3**	**51.11**	**0.11**	**5.37**	**1.54**	**2.66**	**16.65**	**0.08**	**20.88**	**0.04**	**0.61**	**0.00**	**99.04**	**0.918**
sd				*0.25*	*0.02*	*0.16*	*0.03*	*0.24*	*1.16*	*0.02*	*1.41*	*0.01*	*0.07*	*0.01*	*0.11*	*0.00*
rel. sd				0.00	0.15	0.03	0.02	0.09	0.07	0.21	0.07	0.25	0.11	1.73	0.00	0.00

Table D2: Cpx analyses

Sample	File	An#	Text.	SiO2	TiO2	Al2O3	Cr2O3	FeO	MgO	MnO	CaO	NiO	Na2O	K2O	Total	Mg#
Circe93-2a																
c93-2a_1-1	10	84	i	51.58	0.19	4.29	1.20	2.42	17.39	0.09	22.06	0.05	0.28	0.00	99.55	0.928
c93-2a_1-2	10	85	i	51.90	0.17	4.13	1.15	2.53	17.92	0.11	21.52	0.06	0.22	0.00	99.72	0.927
c93-2a-1-3	10	86	i	51.69	0.21	4.25	1.24	2.46	17.79	0.12	21.55	0.04	0.23	0.01	99.58	0.928
c93-2a_1-4	10	87	i	51.51	0.16	4.30	1.23	2.61	18.04	0.09	21.25	0.04	0.25	0.00	99.49	0.925
o93-2a_6-1	10	115	i	51.21	0.20	4.61	1.30	2.21	16.78	0.10	22.27	0.05	0.25	0.00	98.98	0.931
o93-2a_6-2	10	116	i	51.64	0.16	4.40	1.25	2.34	17.16	0.06	21.97	0.05	0.31	0.00	99.34	0.929
o93-2a_6-3	10	117	i	51.60	0.18	4.21	1.25	2.15	17.10	0.08	22.37	0.05	0.30	0.01	99.30	**0.934**
c93-2a_3-1	10	92	i	51.80	0.16	3.98	1.14	2.24	17.21	0.09	22.72	0.04	0.26	0.01	99.66	0.932
c93-2a_3-2	10	93	i	51.51	0.15	4.17	1.18	2.56	17.28	0.05	22.19	0.04	0.18	0.00	99.31	0.923
c93-2a_3-3	10	94	i	52.04	0.16	3.79	0.99	2.52	17.76	0.11	22.15	0.04	0.21	0.02	99.79	0.926
c93-2a_6-1	10	108	i	51.47	0.19	4.57	1.29	2.47	17.67	0.07	21.58	0.03	0.27	0.01	99.61	0.927
c93-2a_6-2	10	110	i	51.48	0.16	4.11	1.23	2.44	17.46	0.09	21.94	0.05	0.29	0.00	99.24	0.927
c93-2a_6-4	10	111	i	51.55	0.16	4.20	1.19	2.58	17.89	0.08	21.35	0.06	0.27	0.00	99.32	0.925
c93-2a_6-2	10	109	i	51.37	0.15	4.44	1.23	2.56	17.77	0.05	21.47	0.04	0.20	0.01	99.29	0.925
ave-all			**14**	**51.60**	**0.17**	**4.25**	**1.20**	**2.44**	**17.52**	**0.09**	**21.89**	**0.05**	**0.25**	**0.00**	**99.44**	**0.928**
sd				*0.21*	*0.02*	*0.22*	*0.08*	*0.15*	*0.37*	*0.02*	*0.44*	*0.01*	*0.04*	*0.01*	*0.22*	*0.00*
rel. sd				0.00	0.11	0.05	0.06	0.06	0.02	0.26	0.02	0.16	0.16	1.36	0.00	0.00
Circe93-4																
c93-4_3b1	6	78	P-c	50.37	0.12	4.94	1.38	2.42	17.02	0.09	22.11	0.04	0.14	0.00	98.64	0.926
c93-4_3b2	6	79	P-c	50.29	0.10	5.06	1.49	2.40	16.72	0.07	22.75	0.05	0.10	0.01	99.04	0.925
c93-4_3b3	6	80	P-c	50.23	0.07	5.04	1.39	2.60	16.98	0.06	22.21	0.06	0.07	0.00	98.71	0.921
c93-4_3b5	6	82	P-c	50.22	0.11	5.09	1.44	2.63	17.27	0.08	21.90	0.04	0.10	0.03	98.90	0.921
ave-all			**4**	**50.28**	**0.10**	**5.03**	**1.43**	**2.51**	**17.00**	**0.08**	**22.24**	**0.05**	**0.10**	**0.01**	**98.82**	**0.923**
sd				*0.07*	*0.02*	*0.07*	*0.05*	*0.12*	*0.23*	*0.01*	*0.36*	*0.01*	*0.03*	*0.01*	*0.18*	*0.00*
rel. sd				0.00	0.20	0.01	0.03	0.05	0.01	0.18	0.02	0.16	0.28	1.32	0.00	0.00
Circe93-7																
c93-7_1-1	29	1	i	52.50	0.10	3.77	1.56	2.25	17.65	0.07	21.44	0.04	0.70	0.00	100.08	0.933
c93-7_1-2	29	2	i	52.81	0.11	3.72	1.44	2.24	17.87	0.12	21.81	0.04	0.56	0.03	100.73	0.934
c93-7_2-1	29	10	i	52.81	0.07	3.86	1.58	2.38	17.67	0.07	21.73	0.06	0.63	0.00	100.86	0.930
c93-7_2-2	29	11	i	53.07	0.08	3.78	1.43	2.18	17.62	0.12	21.58	0.02	0.75	0.00	100.62	0.935
c93-7_2-3	29	12	i	53.16	0.09	3.51	1.42	2.14	17.64	0.10	21.83	0.03	0.72	0.00	100.64	0.936
c93-7_3-1	29	15	i	53.31	0.09	3.36	1.23	2.12	17.82	0.14	21.99	0.07	0.65	0.03	100.81	0.937
c93-7_3-2	29	16	i	52.71	0.12	3.91	1.46	2.14	17.22	0.11	22.24	0.04	0.68	0.00	100.63	0.935
c93-7_4-1	29	17	i	52.02	0.08	4.06	1.66	2.14	17.07	0.12	21.57	0.06	0.69	0.00	99.47	0.934
c93-7_4-2	29	18	i	52.15	0.10	4.08	1.65	2.03	16.90	0.07	22.10	0.01	0.61	0.01	99.71	0.937
c93-7_4-3	29	19	i	52.24	0.12	4.13	1.72	2.18	17.01	0.02	21.72	0.07	0.66	0.00	99.86	0.933
c93-7_4-4	29	20	i	51.95	0.08	4.10	1.81	2.25	17.28	0.14	21.42	0.08	0.65	0.00	99.76	0.932
c93-7b_2-1	29	31	i	52.65	0.09	3.58	1.42	2.25	17.70	0.07	21.79	0.06	0.67	0.00	100.27	0.933
c93-7b_2-2	29	32	i	52.26	0.08	3.72	1.66	2.18	17.11	0.15	21.66	0.06	0.67	0.01	99.57	0.933
ave-all			**13**	**52.59**	**0.09**	**3.81**	**1.54**	**2.19**	**17.43**	**0.10**	**21.76**	**0.05**	**0.66**	**0.01**	**100.23**	**0.934**
sd				*0.44*	*0.01*	*0.24*	*0.16*	*0.09*	*0.34*	*0.04*	*0.24*	*0.02*	*0.05*	*0.01*	*0.51*	*0.00*
rel. sd				0.01	0.16	0.06	0.10	0.04	0.02	0.38	0.01	0.44	0.07	1.78	0.01	0.00
ANTP126-2																
c126-2_2-1	6	52	fRX	50.66	0.09	5.78	1.32	2.97	16.96	0.12	20.91	0.04	0.34	0.01	99.18	0.911
c126-2_2-2	6	53	fRX	50.22	0.08	5.69	1.25	2.90	16.76	0.09	21.29	0.04	0.36	0.02	98.70	0.912
c126-2_3-1	6	56	RX-c	51.13	0.03	5.09	1.15	2.91	17.85	0.10	20.47	0.05	0.22	0.00	99.01	0.916
c126-2_3-2	6	57	RX-c	50.97	0.08	5.34	1.16	2.92	17.60	0.10	20.44	0.05	0.23	0.00	98.89	0.915
c126-2_3p1e	6	59	RX-c	50.92	0.08	5.34	1.17	3.01	17.76	0.11	20.18	0.07	0.27	0.00	98.90	0.913
c126-2_3p1s	6	58	RX-c	51.00	0.04	5.23	1.13	2.99	17.97	0.08	20.30	0.06	0.20	0.00	98.99	0.915
c126-2_3p2e	6	61	RX-c	50.62	0.08	5.32	1.19	2.88	17.64	0.08	20.61	0.05	0.25	0.01	98.72	0.916
c126-2_4-2	6	63	RX-c	50.60	0.08	5.02	1.10	3.00	18.03	0.07	20.75	0.05	0.30	0.01	99.01	0.915
c126-2_4-3	6	64	RX-c	50.94	0.06	4.94	0.98	2.98	18.10	0.07	20.29	0.06	0.25	0.00	98.66	0.915
c126-2_4-4	6	65	RX-c	50.83	0.06	5.01	1.00	2.89	17.66	0.09	20.96	0.05	0.28	0.00	98.82	0.916
ave-all			**10**	**50.79**	**0.07**	**5.28**	**1.14**	**2.95**	**17.63**	**0.09**	**20.62**	**0.05**	**0.27**	**0.01**	**98.89**	**0.914**
sd				*0.27*	*0.02*	*0.28*	*0.10*	*0.05*	*0.44*	*0.02*	*0.35*	*0.01*	*0.05*	*0.01*	*0.17*	*0.00*
rel. sd				0.01	0.28	0.05	0.09	0.02	0.03	0.18	0.02	0.15	0.19	1.45	0.00	0.00
ANTP126-5																
c126-5_2-1	5	17	RX-c	51.07	0.04	5.68	1.19	2.79	17.20	0.09	20.95	0.05	0.33	0.01	99.40	0.917
c126-5_2-2	5	18	RX-c	50.94	0.06	5.84	1.26	3.06	17.69	0.10	19.73	0.05	0.27	0.00	98.99	0.912
c126-5_2-3	5	19	RX-c	51.08	0.06	5.80	1.30	3.28	18.22	0.14	18.80	0.06	0.25	0.01	99.00	0.908
ave-all			**3**	**51.03**	**0.05**	**5.77**	**1.25**	**3.04**	**17.70**	**0.11**	**19.83**	**0.06**	**0.28**	**0.01**	**99.13**	**0.912**
sd				*0.08*	*0.01*	*0.08*	*0.06*	*0.25*	*0.51*	*0.03*	*1.08*	*0.00*	*0.05*	*0.01*	*0.23*	*0.00*
rel. sd				0.00	0.23	0.01	0.05	0.08	0.03	0.24	0.05	0.08	0.16	0.90	0.00	0.00

Table D2: Cpx analyses

Sample	File	An#	Text.	SiO2	TiO2	Al2O3	Cr2O3	FeO	MgO	MnO	CaO	NiO	Na2O	K2O	Total	Mg#
ANTP125-D5																
c126-d5a_2-1	10	55	i	51.29	0.11	4.93	1.08	2.81	16.99	0.10	21.39	0.05	0.37	0.03	99.15	0.915
c126-d5a_2-2	10	56	i	50.75	0.07	5.43	1.07	2.86	17.34	0.10	20.79	0.06	0.28	0.01	98.76	0.915
c126-d5a_3-1	10	57	i	50.66	0.11	5.93	1.23	2.95	17.21	0.12	20.48	0.05	0.28	0.02	99.04	0.912
c126-d5a_6-1	10	67	RX-c	51.32	0.10	5.08	1.01	2.97	18.00	0.12	20.45	0.04	0.25	0.00	99.35	0.915
c126-d5a_6-2	10	68	RX-c	51.62	0.10	5.09	0.99	3.04	18.42	0.10	19.73	0.06	0.27	0.01	99.43	0.915
c126-d5a_6-3	10	69	RX-c	51.78	0.08	4.86	0.95	3.01	18.27	0.05	19.75	0.06	0.25	0.01	99.08	0.915
c126-d5a_6-4	10	70	RX-c	51.12	0.10	5.41	1.06	2.94	18.06	0.10	20.33	0.05	0.26	0.03	99.46	0.916
c126-d5a_6-5	10	71	RX-c	51.10	0.08	5.12	1.09	3.05	18.01	0.10	20.42	0.06	0.21	0.00	99.24	0.913
ave-all			**8**	**51.21**	**0.09**	**5.23**	**1.06**	**2.95**	**17.79**	**0.10**	**20.42**	**0.05**	**0.27**	**0.02**	**99.19**	**0.915**
sd				*0.39*	*0.01*	*0.35*	*0.08*	*0.08*	*0.53*	*0.02*	*0.54*	*0.01*	*0.05*	*0.01*	*0.23*	*0.00*
rel. sd				0.01	0.16	0.07	0.08	0.03	0.03	0.22	0.03	0.14	0.17	0.85	0.00	0.00
31GTV-4																
c31a_1-1	4	4	P-c	50.96	0.13	4.90	1.38	3.10	18.22	0.04	19.38	0.06	0.02	0.01	98.18	0.913
c31a_1-2	4	5	P-c	51.02	0.09	4.82	1.38	3.14	18.22	0.11	19.55	0.04	0.03	0.00	98.38	0.912
ol31a_1-1	4	7	fRX	50.85	0.05	4.41	1.28	2.53	16.49	0.07	21.67	0.05	0.06	0.01	97.48	0.921
ol31a_1-2	4	8	fRX	50.66	0.06	4.39	1.36	2.64	16.44	0.08	21.54	0.05	0.01	0.01	97.24	0.917
ave-all			**4**	**50.87**	**0.08**	**4.63**	**1.35**	**2.85**	**17.34**	**0.08**	**20.54**	**0.05**	**0.03**	**0.01**	**97.82**	**0.916**
sd				*0.16*	*0.03*	*0.27*	*0.04*	*0.31*	*1.01*	*0.03*	*1.24*	*0.01*	*0.02*	*0.01*	*0.55*	*0.00*
rel. sd				0.00	0.43	0.06	0.03	0.11	0.06	0.38	0.06	0.18	0.87	0.69	0.01	0.00
60GTV-5																
c60-5_1-10	12	10	P-c	50.93	0.07	4.30	1.36	2.70	17.83	0.08	21.64	0.05	0.03	0.01	99.00	0.922
c60-5_1-11	12	11	P-c	50.94	0.10	4.36	1.42	2.88	18.05	0.07	20.94	0.04	0.01	0.01	98.81	0.918
c60-5_1-16	12	16	P-r	51.02	0.11	4.11	1.24	2.66	17.49	0.13	22.20	0.03	0.01	0.00	99.01	0.921
c60-5_1-17	12	17	P-r	51.45	0.11	3.96	1.25	2.83	18.24	0.08	21.54	0.05	0.02	0.01	99.55	0.920
c60-5_1-18	12	18	P-r	51.03	0.07	4.13	1.29	2.78	17.76	0.11	21.80	0.06	0.05	0.00	99.08	0.919
c60-5_1-19	12	19	P-r	51.70	0.12	4.12	1.28	2.63	17.68	0.10	21.65	0.06	0.01	0.00	99.35	0.923
c60-5_1-2	12	2	P-c	51.42	0.12	4.74	1.46	2.76	16.97	0.05	21.92	0.05	0.04	0.01	99.54	0.916
c60-5_1-20	12	20	P-r	51.80	0.09	4.08	1.29	2.61	17.02	0.09	22.53	0.05	0.05	0.00	99.60	0.921
c60-5_1-21	12	21	P-r	51.25	0.10	3.95	1.19	2.82	18.36	0.09	20.83	0.04	0.04	0.01	98.68	0.921
c60-5_1-22	12	22	P-r	52.54	0.07	4.05	1.21	3.39	20.15	0.10	18.37	0.06	0.02	0.02	99.97	0.914
c60-5_1-4	12	4	P-c	50.48	0.10	4.92	1.55	2.82	17.29	0.13	22.17	0.05	0.04	0.02	99.57	0.916
c60-5_1-5	12	5	P-c	50.76	0.11	4.72	1.42	2.96	17.52	0.07	21.89	0.04	0.05	0.00	99.54	0.913
c60-5_1-6	12	6	P-c	50.86	0.10	4.62	1.42	2.91	18.08	0.07	20.92	0.03	0.02	0.01	99.04	0.917
c60-5_1-7	12	7	P-c	51.00	0.08	4.78	1.41	3.08	18.08	0.12	20.50	0.05	0.04	0.00	99.14	0.913
c60-5_1-8	12	8	P-c	50.57	0.11	4.97	1.53	3.04	17.76	0.10	21.07	0.04	0.01	0.00	99.19	0.912
c60-5_1-9	12	9	P-c	51.22	0.11	4.37	1.42	2.89	18.16	0.09	21.11	0.05	0.03	0.01	99.44	0.918
c60-5_2-4	12	26	P-c	51.15	0.13	4.37	1.32	2.60	17.48	0.08	22.00	0.06	0.03	0.01	99.22	0.923
c60-5_2-5	12	27	P-c	50.92	0.08	4.34	1.36	2.95	19.08	0.07	20.31	0.04	0.02	0.01	99.18	0.920
c60-5_2-1	12	23	fRX	52.09	0.12	3.63	1.07	2.56	17.62	0.05	22.48	0.04	0.06	0.00	99.72	0.925
c60-5_2-2	12	24	fRX	51.84	0.09	3.82	1.03	2.65	18.17	0.12	21.81	0.03	0.05	0.01	99.62	0.924
c60-5_2-3	12	25	fRX	51.55	0.12	3.69	1.03	2.55	17.90	0.11	22.16	0.03	0.02	0.00	99.16	0.926
c60-5_1-14	12	14	fRX	51.38	0.10	3.35	1.08	2.20	17.74	0.07	22.79	0.04	0.05	0.02	98.82	0.935
c60-5_1-15	12	15	fRX	51.32	0.11	3.80	1.26	2.26	17.42	0.08	22.65	0.04	0.07	0.00	99.00	0.932
ave-fRX			**4**	**51.64**	**0.11**	**3.66**	**1.10**	**2.44**	**17.77**	**0.09**	**22.38**	**0.04**	**0.05**	**0.01**	**99.26**	**0.928**
sd				*0.32*	*0.01*	*0.19*	*0.10*	*0.20*	*0.28*	*0.03*	*0.40*	*0.00*	*0.02*	*0.01*	*0.39*	*0.00*
rel. sd				0.01	0.13	0.05	0.09	0.08	0.02	0.34	0.02	0.14	0.39	1.44	0.00	0.01
ave-p			**18**	**51.17**	**0.10**	**4.38**	**1.36**	**2.85**	**17.94**	**0.09**	**21.30**	**0.05**	**0.03**	**0.01**	**99.27**	**0.918**
sd				*0.49*	*0.02*	*0.33*	*0.10*	*0.20*	*0.75*	*0.02*	*0.96*	*0.01*	*0.01*	*0.01*	*0.32*	*0.00*
rel. sd				0.01	0.18	0.08	0.08	0.07	0.04	0.24	0.05	0.20	0.49	0.95	0.00	0.00

Table D2: Cpx analyses

Sample	File	An#	Text.	SiO2	TiO2	Al2O3	Cr2O3	FeO	MgO	MnO	CaO	NiO	Na2O	K2O	Total	Mg#
74GTV																
c74a_2	1	4		52.25	0.07	4.18	1.26	2.85	18.01	0.12	21.44	0.05	0.03	0.01	100.22	0.918
c74a_3	1	5		52.22	0.05	4.16	1.16	3.05	17.79	0.13	21.54	0.04	0.02	0.02	100.13	0.912
c74a_4	1	6		51.37	0.05	4.08	1.35	3.10	18.04	0.13	21.13	0.03	0.07	0.00	99.32	0.912
c74a_5	1	7		52.57	0.11	4.04	1.16	2.89	17.92	0.06	21.57	0.03	0.04	0.00	100.37	0.917
c74a_6	1	8		52.51	0.06	3.85	1.11	2.84	18.05	0.12	21.58	0.06	0.03	0.01	100.17	0.919
c74a_2	1	9		52.61	0.06	4.39	1.31	3.72	21.16	0.08	16.86	0.04	0.04	0.02	100.24	0.910
c74a_2-2	1	10		52.60	0.06	4.27	1.27	3.72	20.32	0.06	18.33	0.04	0.03	0.02	100.67	0.907
c74a_2-4	1	12		51.97	0.11	4.34	1.33	2.74	17.34	0.06	22.39	0.04	0.04	0.00	100.32	0.919
c74a_2-5	1	13		52.19	0.11	4.36	1.35	2.86	17.44	0.06	21.66	0.05	0.02	0.01	100.06	0.916
c74a_3	1	17		51.54	0.07	4.66	1.48	3.21	17.53	0.12	21.42	0.04	0.01	0.00	100.03	0.907
c74a_3-2	1	18		51.71	0.08	4.93	1.45	2.87	17.54	0.19	21.27	0.03	0.05	0.01	100.09	0.916
c74a_3-3	1	19		52.12	0.05	4.62	1.41	3.34	17.87	0.00	21.03	0.03	0.06	0.00	100.50	0.905
c74a_4	1	20		52.27	0.07	4.46	1.38	2.81	17.37	0.06	22.23	0.06	0.03	0.00	100.68	0.917
c74a_4-2	1	21		52.23	0.07	4.21	1.20	2.71	17.34	0.08	22.11	0.04	0.05	0.00	100.00	0.919
c74b_1-3	1	29		51.48	0.09	4.95	1.61	2.97	16.94	0.10	21.96	0.04	0.03	0.02	100.13	0.910
c74b_1-4	1	30		51.56	0.12	4.63	1.61	2.98	17.57	0.12	21.27	0.05	0.03	0.01	99.88	0.913
c74b_1-5	1	31		52.36	0.08	4.34	1.29	3.15	18.34	0.11	20.95	0.04	0.03	0.00	100.65	0.912
c74b_1-6	1	32		51.95	0.07	4.37	1.44	3.06	18.04	0.07	21.64	0.03	0.05	0.01	100.70	0.913
c74b_2	1	36		51.96	0.06	4.27	1.42	3.17	18.77	0.08	20.16	0.03	0.02	0.00	99.89	0.913
c74b_3	1	40		52.43	0.11	3.94	1.10	2.82	17.77	0.12	21.71	0.06	0.04	0.02	100.05	0.918
c74b_3-2	1	41		52.60	0.09	3.86	1.11	2.74	17.55	0.09	22.17	0.04	0.03	0.00	100.24	0.920
ave-all			**21**	**52.12**	**0.08**	**4.33**	**1.32**	**3.03**	**18.03**	**0.09**	**21.16**	**0.04**	**0.04**	**0.01**	**100.21**	**0.914**
sd				*0.40*	*0.02*	*0.31*	*0.15*	*0.28*	*0.99*	*0.04*	*1.31*	*0.01*	*0.01*	*0.01*	*0.33*	*0.00*
rel. sd				0.01	0.30	0.07	0.11	0.09	0.06	0.42	0.06	0.25	0.41	1.00	0.00	0.00
ANTP 84-11																
c84-11_1-1	24	17	RX-c	50.56	0.02	4.40	1.30	2.61	17.19	0.09	23.39	0.05	0.17	0.01	99.79	0.921
c84-11_1-2	24	18	RX-c	50.99	0.02	4.26	1.32	2.65	17.46	0.11	23.03	0.06	0.10	0.00	99.99	0.922
c84-11_1-3	24	19	P-c	50.70	0.00	4.60	1.44	2.71	16.94	0.07	22.90	0.05	0.10	0.01	99.52	0.918
c84-11_1-4	24	20	P-c	50.61	0.04	4.40	1.45	2.63	16.81	0.11	23.33	0.06	0.12	0.02	99.56	0.919
c84-11_2-1	24	21	RX-c	50.63	0.02	4.38	1.31	2.75	17.70	0.07	22.84	0.06	0.10	0.00	99.86	0.920
c84-11_2-2	24	22	RX-c	50.81	0.03	4.41	1.37	2.62	17.28	0.11	22.91	0.05	0.08	0.00	99.68	0.922
c84-11_2-4	24	24	P-c	51.13	0.03	4.63	1.46	3.08	19.05	0.11	20.94	0.05	0.12	0.00	100.59	0.917
ave-all			**7**	**50.78**	**0.02**	**4.44**	**1.38**	**2.72**	**17.49**	**0.09**	**22.76**	**0.05**	**0.11**	**0.01**	**99.85**	**0.920**
sd				*0.21*	*0.01*	*0.13*	*0.07*	*0.17*	*0.75*	*0.02*	*0.83*	*0.01*	*0.03*	*0.01*	*0.36*	*0.00*
rel. sd				0.00	0.54	0.03	0.05	0.06	0.04	0.20	0.04	0.12	0.25	1.33	0.00	0.00
ANTP 87-5																
c87-5a_1-1	16	7	XS	51.40	0.06	4.58	1.16	3.04	17.25	0.11	22.15	0.07	0.14	0.00	99.96	0.910
c87-5a_4-1	16	14	i	51.65	0.05	4.31	1.19	2.97	17.74	0.08	21.96	0.06	0.24	0.00	100.24	0.914
c87-5a_4-2	16	15	i	51.88	0.03	4.39	1.17	2.86	17.56	0.08	21.93	0.05	0.23	0.00	100.18	0.916
c87-5a_4-3	16	16	i	51.50	0.06	4.42	1.20	3.02	17.63	0.07	22.08	0.03	0.19	0.00	100.19	0.912
c87-5a_5-3	16	21	i	52.03	0.04	4.43	1.29	3.41	18.87	0.10	20.31	0.07	0.23	0.02	100.81	0.908
c87-5a_5-5	16	23	i	51.76	0.04	4.39	1.22	2.98	17.65	0.08	22.00	0.06	0.27	0.00	100.45	0.913
c87-5a_5-6	16	24	i	51.91	0.04	4.44	1.26	3.54	19.23	0.09	19.75	0.04	0.21	0.00	100.51	0.906
ave-all			**7**	**51.73**	**0.05**	**4.42**	**1.21**	**3.12**	**17.99**	**0.09**	**21.45**	**0.06**	**0.21**	**0.00**	**100.33**	**0.912**
sd				*0.23*	*0.01*	*0.08*	*0.05*	*0.25*	*0.75*	*0.01*	*0.99*	*0.02*	*0.04*	*0.01*	*0.28*	*0.00*
rel. sd				0.00	0.22	0.02	0.04	0.08	0.04	0.15	0.05	0.27	0.19	2.65	0.00	0.00
ANTP 87-9																
c87-9_2-2	23	39	i	51.86	0.06	4.27	1.32	3.21	18.28	0.10	20.84	0.07	0.30	0.00	100.32	0.910
c87-9_4-1	23	46	i	52.41	0.08	3.67	1.15	2.96	18.10	0.10	21.48	0.04	0.39	0.00	100.39	0.916
c87-9_4-2	23	47	i	52.06	0.07	4.03	1.30	3.21	18.17	0.08	21.23	0.05	0.34	0.01	100.54	0.910
c87-9_4-3	23	48	i	52.26	0.04	3.93	1.24	3.13	18.12	0.10	21.19	0.05	0.35	0.00	100.41	0.912
c87-9_4-4	23	49	i	52.16	0.05	3.75	1.18	2.82	17.34	0.09	22.26	0.04	0.49	0.00	100.19	0.916
c87-9_5-1	23	50	XS	52.06	0.03	4.26	1.35	3.21	18.16	0.08	20.51	0.01	0.34	0.00	100.01	0.910
c87-9_5-2	23	51	XS	51.54	0.07	4.24	1.44	3.08	17.66	0.12	21.32	0.05	0.35	0.00	99.86	0.911
ave-all			**7**	**52.05**	**0.06**	**4.02**	**1.28**	**3.09**	**17.98**	**0.09**	**21.26**	**0.05**	**0.37**	**0.00**	**100.25**	**0.912**
sd				*0.28*	*0.02*	*0.25*	*0.10*	*0.15*	*0.34*	*0.01*	*0.55*	*0.02*	*0.06*	*0.00*	*0.24*	*0.00*
rel. sd				0.01	0.30	0.06	0.08	0.05	0.02	0.13	0.03	0.40	0.17	2.65	0.00	0.00

Table D2: Cpx analyses

Sample	File	An#	Text.	SiO2	TiO2	Al2O3	Cr2O3	FeO	MgO	MnO	CaO	NiO	Na2O	K2O	Total	Mg#
ANTP 89-1																
c89-1_2-1	19	7	fRX	52.19	0.08	4.08	1.03	2.25	16.92	0.08	22.80	0.04	0.59	0.01	100.06	0.931
c89-1_2-3	19	9	fRX	52.30	0.11	3.93	0.95	2.47	17.58	0.04	22.13	0.04	0.53	0.00	100.08	0.927
o89-1_4-2	19	19	fRX	52.05	0.13	4.12	1.04	2.23	16.96	0.11	23.03	0.06	0.55	0.00	100.27	0.931
c89-1_2-2	19	8	RX-c	51.21	0.13	5.01	1.50	2.40	16.31	0.09	22.51	0.06	0.57	0.02	99.80	0.924
c89-1_2-4	19	10	RX-c	51.06	0.14	4.97	1.43	2.34	16.53	0.11	22.66	0.04	0.60	0.01	99.89	0.926
c89-1_4-1	19	16	P-c	50.97	0.21	5.74	1.59	2.68	17.17	0.07	20.74	0.05	0.66	0.02	99.89	0.919
c89-1_4-2	19	17	P-c	50.62	0.24	6.07	1.68	2.44	16.30	0.10	22.12	0.05	0.58	0.00	100.20	0.923
ave-p, RX			**4**	**50.97**	**0.18**	**5.45**	**1.55**	**2.47**	**16.58**	**0.09**	**22.01**	**0.05**	**0.60**	**0.01**	**99.94**	**0.923**
sd				*0.25*	*0.05*	*0.55*	*0.11*	*0.15*	*0.41*	*0.02*	*0.88*	*0.01*	*0.04*	*0.01*	*0.18*	*0.00*
rel. sd				0.00	0.30	0.10	0.07	0.06	0.02	0.21	0.04	0.11	0.07	0.84	0.00	0.00
ave-fRX			**3**	**52.18**	**0.10**	**4.04**	**1.01**	**2.32**	**17.15**	**0.08**	**22.65**	**0.05**	**0.56**	**0.00**	**100.14**	**0.930**
sd				*0.13*	*0.02*	*0.10*	*0.05*	*0.13*	*0.37*	*0.04*	*0.47*	*0.01*	*0.03*	*0.00*	*0.12*	*0.00*
rel. sd				0.00	0.21	0.02	0.04	0.06	0.02	0.47	0.02	0.24	0.06	1.73	0.00	0.00
ANTP 89-2																
c89-2_3-1	28	5	RX-c	51.10	0.14	5.36	1.42	2.58	16.84	0.12	22.30	0.05	0.38	0.01	100.30	0.921
c89-2_3-2	28	6	RX-c	51.11	0.12	5.37	1.40	2.64	16.85	0.13	22.57	0.05	0.43	0.02	100.68	0.919
c89-2_4-1	28	12	RX-c	51.03	0.14	5.05	1.33	2.59	16.29	0.09	23.16	0.04	0.40	0.00	100.11	0.918
c89-2_4-2	28	13	RX-c	51.18	0.11	5.23	1.35	2.68	16.94	0.08	22.09	0.04	0.36	0.00	100.06	0.918
c89-2_4-3	28	14	RX-c	50.96	0.11	5.17	1.42	2.59	16.54	0.09	23.16	0.05	0.38	0.00	100.46	0.919
c89-2_4-4	28	15	RX-c	51.12	0.12	5.07	1.42	2.47	16.60	0.09	22.97	0.05	0.37	0.00	100.28	0.923
c89-2_4-5	28	16	RX-c	51.34	0.10	5.26	1.44	2.63	16.91	0.12	22.36	0.02	0.34	0.01	100.53	0.920
c89-2_4-6	28	17	RX-c	50.70	0.15	5.28	1.34	2.60	16.60	0.05	22.50	0.05	0.38	0.02	99.66	0.919
c89-2_4-7	28	18	RX-c	51.02	0.12	5.31	1.36	2.56	16.55	0.09	23.03	0.03	0.40	0.00	100.48	0.920
c89-2_4-8	28	19	RX-c	51.10	0.13	5.32	1.34	2.47	16.51	0.10	23.15	0.05	0.38	0.00	100.54	0.923
ave-all			**10**	**51.07**	**0.12**	**5.24**	**1.38**	**2.58**	**16.66**	**0.10**	**22.73**	**0.04**	**0.38**	**0.01**	**100.31**	**0.920**
sd				*0.16*	*0.02*	*0.11*	*0.04*	*0.07*	*0.21*	*0.02*	*0.41*	*0.01*	*0.02*	*0.01*	*0.30*	*0.00*
rel. sd				0.00	0.13	0.02	0.03	0.03	0.01	0.24	0.02	0.25	0.06	1.38	0.00	0.00
ANTP 89-5																
c89-5_2-1	21	93	i	50.89	0.19	5.40	1.00	2.71	16.25	0.09	23.25	0.04	0.34	0.00	100.16	0.914
c89-5_2-2	21	94	i	50.79	0.20	5.37	1.01	2.65	15.94	0.08	23.21	0.02	0.28	0.01	99.56	0.915
c89-5_2-3	21	95	i	51.70	0.18	4.59	0.91	2.74	16.98	0.07	22.62	0.01	0.26	0.00	100.06	0.917
c89-5_2-4	21	96	i	51.31	0.16	5.19	1.02	2.83	16.71	0.10	22.66	0.04	0.23	0.01	100.26	0.913
c89-5_3-1	21	97	P-c	50.42	0.13	6.19	1.24	2.81	16.01	0.13	23.12	0.04	0.32	0.00	100.41	0.910
c89-5_3-2	21	98	P-c	50.11	0.16	6.18	1.24	2.93	16.60	0.11	22.29	0.05	0.26	0.01	99.94	0.910
c89-5_3-3	21	99	P-c	50.64	0.15	6.13	1.21	3.10	17.22	0.11	21.35	0.06	0.26	0.00	100.24	0.908
c89-5_3-4	21	100	P-c	50.93	0.13	6.13	1.22	3.18	17.33	0.12	21.34	0.05	0.25	0.00	100.68	0.907
c89-5_3-11	21	109	fRX	51.63	0.21	4.62	1.02	2.75	16.81	0.09	23.09	0.03	0.27	0.00	100.51	0.916
c89-5_3-12	21	110	fRX	51.60	0.17	4.50	1.03	2.78	16.87	0.09	22.88	0.06	0.26	0.00	100.23	0.915
c89-5_3-13	21	111	fRX	51.12	0.15	4.47	1.04	3.00	17.37	0.10	22.25	0.06	0.25	0.01	99.81	0.912
c89-5_3-14	21	112	fRX	51.16	0.19	5.22	1.12	2.78	16.16	0.11	23.29	0.03	0.22	0.01	100.28	0.912
ave-i			**4**	**51.17**	**0.18**	**5.14**	**0.98**	**2.73**	**16.47**	**0.09**	**22.94**	**0.03**	**0.28**	**0.00**	**100.01**	**0.915**
sd				*0.42*	*0.02*	*0.38*	*0.05*	*0.08*	*0.46*	*0.01*	*0.34*	*0.01*	*0.05*	*0.01*	*0.31*	*0.00*
rel. sd				0.01	0.09	0.07	0.05	0.03	0.03	0.16	0.01	0.56	0.17	1.23	0.00	0.00
ave-p			**4**	**50.53**	**0.14**	**6.16**	**1.23**	**3.01**	**16.79**	**0.12**	**22.03**	**0.05**	**0.27**	**0.00**	**100.32**	**0.909**
sd				*0.35*	*0.01*	*0.03*	*0.01*	*0.17*	*0.61*	*0.01*	*0.86*	*0.01*	*0.03*	*0.01*	*0.31*	*0.00*
rel. sd				0.01	0.10	0.01	0.01	0.06	0.04	0.07	0.04	0.20	0.12	2.00	0.00	0.00
ave-fRX			**4**	**51.38**	**0.18**	**4.70**	**1.05**	**2.83**	**16.80**	**0.10**	**22.88**	**0.04**	**0.25**	**0.00**	**100.21**	**0.914**
sd				*0.28*	*0.03*	*0.35*	*0.04*	*0.12*	*0.50*	*0.01*	*0.45*	*0.02*	*0.02*	*0.01*	*0.29*	*0.00*
rel. sd				0.01	0.14	0.07	0.04	0.04	0.03	0.11	0.02	0.42	0.08	1.17	0.00	0.00
ANTP 89-8																
c89-8_1-1	26	7	P-c	50.17	0.14	6.14	1.34	2.79	16.42	0.15	22.68	0.04	0.26	0.01	100.14	0.913
c89-8_1-2	26	8	P-c	50.64	0.13	6.22	1.33	3.09	17.42	0.10	21.08	0.06	0.26	0.00	100.32	0.909
c89-8_1-3	26	9	P-c	50.14	0.12	6.15	1.35	2.66	16.24	0.10	22.57	0.03	0.26	0.00	99.62	0.916
c89-8_1-4	26	10	P-c	50.57	0.16	6.21	1.39	2.70	16.32	0.11	22.74	0.04	0.33	0.00	100.55	0.915
c89-8_4-1	26	17	P-c	51.04	0.12	5.80	1.31	2.51	16.24	0.11	23.19	0.05	0.35	0.00	100.72	0.920
c89-8_4-2	26	18	P-c	50.98	0.13	5.86	1.31	2.69	16.52	0.10	22.73	0.03	0.34	0.00	100.69	0.916
c89-8_4-3	26	21	fRX	51.58	0.14	4.97	0.89	2.41	16.68	0.08	23.33	0.05	0.26	0.00	100.38	0.925
c89-8_4-4	26	22	fRX	51.62	0.14	4.82	0.92	2.46	16.60	0.08	23.64	0.04	0.27	0.01	100.60	0.923
ave-p			**6**	**50.59**	**0.13**	**6.06**	**1.34**	**2.74**	**16.53**	**0.11**	**22.50**	**0.04**	**0.30**	**0.00**	**100.34**	**0.915**
sd				*0.38*	*0.01*	*0.18*	*0.03*	*0.19*	*0.45*	*0.02*	*0.73*	*0.01*	*0.05*	*0.00*	*0.42*	*0.00*
rel. sd				0.01	0.10	0.03	0.02	0.07	0.03	0.17	0.03	0.29	0.15	2.45	0.00	0.00
ave-fRX			**2**	**51.60**	**0.14**	**4.90**	**0.90**	**2.44**	**16.64**	**0.08**	**23.49**	**0.04**	**0.26**	**0.01**	**100.49**	**0.924**

Table D2: Cpx analyses

Sample	File	An#	Text.	SiO2	TiO2	Al2O3	Cr2O3	FeO	MgO	MnO	CaO	NiO	Na2O	K2O	Total	Mg#
ANTP 89-15																
c89-15a_2-1	25	4	fRX	50.95	0.14	5.34	1.59	2.65	17.20	0.11	21.57	0.04	0.59	0.01	100.18	0.920
c89-15b_2-1	27	15	RX-c	51.44	0.16	5.02	1.45	2.48	16.68	0.07	22.67	0.03	0.53	0.01	100.54	0.923
c89-15b_2-2	27	16	RX-c	51.42	0.18	5.05	1.47	2.58	17.16	0.08	21.99	0.05	0.52	0.00	100.49	0.922
c89-15b_2-3	27	17	RX-c	51.19	0.15	4.93	1.48	2.37	16.85	0.09	22.55	0.06	0.58	0.00	100.24	0.927
c89-15b_2-4	27	18	RX-c	51.23	0.19	4.97	1.41	2.50	16.85	0.11	22.16	0.04	0.54	0.01	100.00	0.923
c89-15b_4-1	27	23	i	51.13	0.22	5.32	1.55	2.15	16.32	0.10	23.03	0.06	0.65	0.00	100.53	0.931
c89-15b_4-2	27	24	i	50.98	0.21	5.37	1.60	2.30	16.55	0.06	22.77	0.07	0.50	0.00	100.41	0.928
c89-15b_4-3	27	25	i	51.06	0.20	5.34	1.48	2.54	17.03	0.08	22.05	0.05	0.55	0.00	100.38	0.923
ave-all			**8**	**51.18**	**0.18**	**5.17**	**1.50**	**2.45**	**16.83**	**0.09**	**22.35**	**0.05**	**0.56**	**0.00**	**100.35**	**0.925**
sd				*0.18*	*0.03*	*0.19*	*0.07*	*0.16*	*0.30*	*0.02*	*0.48*	*0.01*	*0.05*	*0.00*	*0.19*	*0.00*
rel. sd				0.00	0.17	0.04	0.05	0.07	0.02	0.19	0.02	0.25	0.09	1.42	0.00	0.00
ANTP 89-17																
c89-17_2-1	25	25	RX-c	51.10	0.12	4.72	1.20	2.44	17.02	0.07	23.23	0.04	0.04	0.00	99.98	0.926
c89-17_2-2	25	26	RX-c	51.03	0.06	4.85	1.36	2.51	17.22	0.09	22.95	0.08	0.07	0.00	100.21	0.924
c89-17_2-3	25	27	RX-c	51.57	0.09	4.61	1.33	2.68	17.31	0.10	22.44	0.05	0.07	0.01	100.26	0.920
c89-17_2-4	25	28	RX-c	50.73	0.09	5.02	1.49	2.40	16.78	0.13	23.37	0.05	0.07	0.00	100.13	0.926
c89-17_2-5	25	29	RX-c	50.94	0.06	4.84	1.43	2.83	17.90	0.12	21.91	0.08	0.04	0.01	100.16	0.919
c89-17_2-6	25	30	RX-c	50.99	0.07	4.79	1.39	2.33	17.03	0.10	23.28	0.05	0.09	0.00	100.11	0.929
c89-17_4-1	25	34	RX-c	51.18	0.03	4.64	1.34	2.50	17.22	0.11	23.33	0.06	0.09	0.00	100.49	0.925
c89-17_4-2	25	35	RX-c	51.59	0.06	4.33	1.17	2.50	17.41	0.10	23.00	0.04	0.07	0.01	100.28	0.925
c89-17_3-1	25	33	i	51.64	0.11	4.07	1.16	2.31	17.42	0.10	23.19	0.04	0.07	0.00	100.11	0.931
c89-17_4-3	25	36	i	52.12	0.10	3.55	0.92	2.28	17.54	0.08	23.58	0.03	0.05	0.00	100.26	0.932
ave-p			**8**	**51.14**	**0.07**	**4.73**	**1.34**	**2.52**	**17.24**	**0.10**	**22.94**	**0.06**	**0.07**	**0.00**	**100.20**	**0.924**
sd				*0.30*	*0.03*	*0.21*	*0.11*	*0.16*	*0.33*	*0.02*	*0.51*	*0.01*	*0.02*	*0.01*	*0.15*	*0.00*
rel. sd				0.01	0.38	0.04	0.08	0.06	0.02	0.19	0.02	0.26	0.26	1.44	0.00	0.00
ave-i			**2**	**51.88**	**0.10**	**3.81**	**1.04**	**2.30**	**17.48**	**0.09**	**23.39**	**0.04**	**0.06**	**0.00**	**100.18**	**0.931**

Table D3: Opx analyses

Sample	file	An#	Text.	SiO2	TiO2	Al2O3	Cr2O3	FeO	MgO	MnO	CaO	NiO	Na2O	K2O	Total	Mg#
ANTP134-3																
o134-3_2-1	6	13	RX-c	54.28	0.05	3.89	0.86	5.60	33.26	0.12	1.35	0.07	0.05	0.00	99.53	0.914
o134-3_2-2	6	14	RX-c	54.33	0.08	3.97	0.82	5.53	32.38	0.10	1.97	0.08	0.03	0.01	99.29	0.913
o134-3_2-3	6	15	RX-c	54.48	0.07	3.87	0.83	5.85	33.53	0.14	0.83	0.08	0.03	0.00	99.71	0.911
o134-3_2-4	6	16	RX-c	54.39	0.05	3.77	0.91	5.69	33.50	0.14	0.99	0.10	0.03	0.01	99.57	0.913
o134-3_4cpe	6	34	P-c	54.60	0.05	4.06	0.90	5.62	32.58	0.14	1.60	0.11	0.04	0.00	99.70	0.912
o134-3_4rpe	6	36	P-r	54.17	0.02	4.27	0.90	5.74	33.52	0.14	0.89	0.09	0.03	0.00	99.77	0.912
c134-3_3-1	6	21	fRX	54.52	0.04	3.60	0.74	5.55	33.05	0.18	1.63	0.09	0.04	0.02	99.45	0.914
c134-3_3-2	6	22	fRX	54.12	0.04	3.51	0.73	5.50	33.38	0.14	1.58	0.10	0.04	0.00	99.12	0.915
ave-P, RX			**6**	**54.38**	**0.05**	**3.97**	**0.87**	**5.67**	**33.13**	**0.13**	**1.27**	**0.09**	**0.03**	**0.00**	**99.59**	**0.912**
sd				*0.17*	*0.02*	*0.24*	*0.07*	*0.12*	*0.45*	*0.02*	*0.41*	*0.01*	*0.01*	*0.01*	*0.22*	*0.00*
rel. sd				0.00	0.34	0.06	0.08	0.02	0.01	0.16	0.32	0.15	0.23	1.83	0.00	0.00
ave-fRX			**2**	**54.32**	**0.04**	**3.56**	**0.73**	**5.53**	**33.22**	**0.16**	**1.61**	**0.09**	**0.04**	**0.01**	**99.29**	**0.91**
ANTP134-4 (@4 mm from vein)																
o134-4_3-1	8	32	P-c	54.65	0.04	3.98	0.85	5.60	33.45	0.13	1.33	0.10	0.02	0.01	100.17	0.914
o134-4_3-2	8	33	P-c	54.57	0.05	4.11	0.91	5.58	33.38	0.12	1.12	0.09	0.03	0.00	99.96	0.914
o134-4_4-1	8	38	P-c	54.06	0.05	4.16	0.95	5.36	31.80	0.12	3.11	0.10	0.10	0.00	99.80	0.914
o134-4_4-2	8	39	P-c	54.00	0.06	4.31	0.93	5.62	32.91	0.11	1.42	0.10	0.01	0.00	99.47	0.913
o134-4_2-1	8	27	fRX	55.09	0.08	3.71	0.70	5.06	32.71	0.14	2.53	0.07	0.06	0.00	100.15	0.920
o134-4_2-2	8	28	fRX	54.88	0.04	3.73	0.72	5.31	32.70	0.14	2.03	0.09	0.06	0.00	99.69	0.916
o134-4_5-1	8	44	fRX	54.69	0.07	3.66	0.70	5.35	33.63	0.10	1.43	0.07	0.00	0.00	99.70	0.918
o134-4_5-2	8	45	fRX	54.82	0.06	3.53	0.73	5.19	33.85	0.14	1.14	0.07	0.02	0.00	99.55	0.921
ave-P-c			**4**	**54.32**	**0.05**	**4.14**	**0.91**	**5.54**	**32.89**	**0.12**	**1.75**	**0.10**	**0.04**	**0.00**	**99.85**	**0.914**
sd				*0.29*	*0.01*	*0.12*	*0.04*	*0.10*	*0.66*	*0.01*	*0.79*	*0.00*	*0.04*	*0.01*	*0.26*	*0.00*
rel. sd				0.01	0.13	0.03	0.04	0.02	0.02	0.07	0.45	0.03	0.88	1.73	0.00	0.00
ave-fRX			**4**	**54.87**	**0.06**	**3.66**	**0.71**	**5.23**	**33.22**	**0.13**	**1.78**	**0.07**	**0.03**	**0.00**	**99.77**	**0.919**
sd				*0.14*	*0.02*	*0.08*	*0.01*	*0.11*	*0.52*	*0.02*	*0.54*	*0.01*	*0.03*	*0.00*	*0.23*	*0.00*
rel. sd				0.00	0.26	0.02	0.02	0.02	0.02	0.15	0.30	0.09	0.79		0.00	0.00
ANTP134-5																
o134-5_2-1	5	29	P-c	54.07	0.05	4.15	0.92	5.40	32.99	0.12	1.77	0.11	0.03	0.00	99.60	0.916
o134-5_2-2	5	30	P-c	54.63	0.02	3.95	0.90	5.57	33.37	0.07	1.02	0.11	0.00	0.01	99.66	0.914
ave-P-c			**2**	**54.35**	**0.04**	**4.05**	**0.91**	**5.49**	**33.18**	**0.09**	**1.39**	**0.11**	**0.01**	**0.01**	**99.63**	**0.92**
ANTP134-8																
o134-8_1-1	8	1	P-c	54.20	0.05	4.29	0.95	5.48	32.88	0.13	1.83	0.09	0.03	0.00	99.93	0.914
o134-8_1-2	8	2	P-c	53.90	0.05	4.22	1.01	5.30	31.99	0.13	2.36	0.10	0.03	0.00	99.09	0.915
o134-8_3-1	8	8	fRX	54.90	0.06	3.59	0.81	5.58	33.24	0.16	1.48	0.10	0.04	0.00	99.95	0.914
o134-8_3-2	8	9	fRX	55.14	0.04	3.28	0.67	5.50	33.72	0.13	0.90	0.09	0.00	0.01	99.47	0.916
ave-P-c			**2**	**54.05**	**0.05**	**4.26**	**0.98**	**5.39**	**32.44**	**0.13**	**2.10**	**0.09**	**0.03**	**0.00**	**99.51**	**0.91**
ave-fRX			**2**	**55.02**	**0.05**	**3.44**	**0.74**	**5.54**	**33.48**	**0.14**	**1.19**	**0.09**	**0.02**	**0.01**	**99.71**	**0.92**
Circe93-2																
o2a_4-1	10	95	P-c	54.44	0.07	3.88	0.94	5.41	32.96	0.13	1.88	0.09	0.02	0.00	99.82	0.916
o2a_4-2	10	96	P-c	54.25	0.07	3.93	0.91	5.39	32.87	0.15	2.08	0.11	0.00	0.01	99.77	0.916
o2a_4-3	10	97	P-c	54.61	0.05	3.79	0.95	5.25	32.72	0.12	2.19	0.10	0.00	0.02	99.80	0.917
o2a_4-4	10	98	P-c	54.71	0.05	3.74	0.92	5.45	33.19	0.12	2.08	0.11	0.00	0.01	100.37	0.916
o2a_1-1	10	80	P-r	54.99	0.06	3.39	0.71	5.46	33.75	0.14	1.29	0.09	0.03	0.00	99.91	0.917
o2a_1-2	10	81	P-r	54.81	0.09	3.29	0.80	5.38	33.70	0.14	1.52	0.09	0.04	0.01	99.86	0.918
o2a_1-3	10	82	P-r	54.88	0.07	3.36	0.76	5.35	33.25	0.13	1.91	0.07	0.00	0.00	99.77	0.917
o2a_1-4	10	83	P-r	54.56	0.09	3.60	0.82	5.37	33.17	0.15	1.81	0.08	0.03	0.00	99.67	0.917
o2a_5-1	10	102	fRX	54.79	0.04	3.23	0.77	5.67	33.87	0.12	1.24	0.08	0.01	0.00	99.83	0.914
o2a_5-2	10	103	fRX	55.15	0.06	3.29	0.64	5.49	33.98	0.14	1.18	0.08	0.01	0.00	100.02	0.917
o2a_5-3	10	104	fRX	55.52	0.07	2.68	0.53	5.63	34.36	0.17	1.05	0.09	0.00	0.01	100.11	0.916
Ave-P-c			**4**	**54.50**	**0.06**	**3.84**	**0.93**	**5.38**	**32.94**	**0.13**	**2.06**	**0.10**	**0.00**	**0.01**	**99.94**	**0.916**
sd				*0.17*	*0.01*	*0.07*	*0.02*	*0.08*	*0.17*	*0.01*	*0.11*	*0.01*	*0.01*	*0.01*	*0.25*	*0.00*
rel. sd				0.00	0.22	0.02	0.02	0.01	0.01	0.09	0.05	0.07	1.73	0.70	0.00	0.00
Ave-P-r			**4**	**54.81**	**0.08**	**3.41**	**0.77**	**5.39**	**33.47**	**0.14**	**1.63**	**0.08**	**0.02**	**0.00**	**99.80**	**0.917**
sd				*0.16*	*0.01*	*0.12*	*0.04*	*0.04*	*0.26*	*0.01*	*0.24*	*0.01*	*0.01*	*0.01*	*0.09*	*0.00*
rel. sd				0.00	0.17	0.03	0.05	0.01	0.01	0.06	0.15	0.09	0.61	1.73	0.00	0.00
Ave-fRX			**3**	**55.15**	**0.06**	**3.07**	**0.65**	**5.60**	**34.07**	**0.14**	**1.16**	**0.08**	**0.01**	**0.00**	**99.99**	**0.916**
sd				*0.30*	*0.01*	*0.27*	*0.10*	*0.08*	*0.21*	*0.02*	*0.08*	*0.01*	*0.00*	*0.00*	*0.12*	*0.00*
rel. sd				0.01	0.18	0.09	0.16	0.01	0.01	0.15	0.07	0.08	0.71	1.41	0.00	0.00

Table D3: Opx analyses

Sample	file	An#	Text.	SiO2	TiO2	Al2O3	Cr2O3	FeO	MgO	MnO	CaO	NiO	Na2O	K2O	Total	Mg#
Circe93-3																
o3a_2-1	9	3	P-c	55.15	0.09	3.17	0.94	5.10	33.71	0.12	1.53	0.10	0.03	0.00	99.94	0.922
o3a_2-2	9	4	P-c	55.10	0.08	3.17	0.92	5.05	33.20	0.12	1.70	0.10	0.08	0.00	99.53	0.921
o3b_4-1	9	25	P-r	55.13	0.09	2.97	0.91	4.96	33.08	0.11	2.57	0.07	0.12	0.00	100.01	0.922
o3b_4-2	9	26	P-r	55.18	0.05	3.08	0.87	5.14	33.97	0.16	1.67	0.10	0.03	0.00	100.24	0.922
Ave-P-c			**2**	**55.13**	**0.09**	**3.17**	**0.93**	**5.08**	**33.46**	**0.12**	**1.62**	**0.10**	**0.06**	**0.00**	**99.73**	**0.92**
Ave-P-r			**2**	**55.16**	**0.07**	**3.03**	**0.89**	**5.05**	**33.53**	**0.13**	**2.12**	**0.09**	**0.07**	**0.00**	**100.13**	**0.92**
Circe93-4																
o93-4_3-4	6	77	P-c	53.46	0.07	4.22	1.05	5.43	32.34	0.17	2.77	0.11	0.03	0.01	99.65	0.914
o93-4_3-3	6	76	P-c	53.69	0.05	3.98	0.99	5.53	32.84	0.17	2.12	0.11	0.02	0.00	99.50	0.914
Ave-P-r			**2**	**53.58**	**0.06**	**4.10**	**1.02**	**5.48**	**32.59**	**0.17**	**2.45**	**0.11**	**0.03**	**0.00**	**99.58**	**0.91**
o93-4_3-1	**6**	**74**	P-r	**54.06**	**0.03**	**3.27**	**0.73**	**5.33**	**33.34**	**0.16**	**1.88**	**0.09**	**0.02**	**0.01**	**98.92**	**0.918**
Circe93-5																
o5a_4-1	12	40	P-c	56.17	0.04	**1.65**	0.76	4.91	34.48	0.14	1.63	0.11	0.09	0.01	99.98	**0.926**
o5a_4-2	12	41	P-c	56.08	0.03	**1.87**	0.86	5.07	34.48	0.14	1.32	0.08	0.01	0.01	99.95	**0.924**
Ave-P-c			**2**	**56.13**	**0.04**	**1.76**	**0.81**	**4.99**	**34.48**	**0.14**	**1.47**	**0.09**	**0.05**	**0.01**	**99.97**	**0.92**
Circe93-7																
c93-7_1-3	29	3	P-c	56.18	0.01	2.80	0.74	5.40	34.79	0.14	1.07	0.10	0.03	0.00	101.26	0.920
c93-7_1-4	29	4	P-c	56.19	0.04	2.94	0.74	5.27	34.47	0.12	1.17	0.11	0.01	0.00	101.05	0.921
o93-7_1-1	29	8	P-c	55.77	0.04	2.69	0.79	4.99	34.06	0.13	2.12	0.08	0.08	0.01	100.76	0.924
o93-7_1-2	29	9	P-c	55.90	0.00	2.75	0.81	5.02	33.87	0.12	1.99	0.13	0.06	0.02	100.67	0.923
o93-8_1-1	29	25	P-c	55.46	0.03	3.16	0.95	5.18	33.69	0.09	1.82	0.09	0.06	0.01	100.56	0.921
o93-8_1-2	29	26	P-c	55.45	0.03	2.90	0.95	4.96	33.07	0.12	2.76	0.09	0.10	0.02	100.45	0.922
Ave-P-c			**6**	**55.83**	**0.02**	**2.87**	**0.83**	**5.14**	**33.99**	**0.12**	**1.82**	**0.10**	**0.06**	**0.01**	**100.79**	**0.922**
ANTP126-2																
o126-2_2p1e	6	43	P-c	54.21	0.05	4.06	0.70	5.52	32.59	0.12	1.84	0.11	0.02	0.00	99.21	0.913
o126-2_2p1s	6	42	P-c	54.21	0.05	3.90	0.63	5.72	32.90	0.10	1.67	0.09	0.06	0.00	99.32	0.911
o126-2_2p2e	6	45	P-c	53.98	0.01	4.20	0.78	5.71	32.49	0.13	2.18	0.10	0.05	0.00	99.62	0.910
o126-2_2p2s	6	44	P-c	53.75	0.04	4.22	0.80	5.56	32.76	0.12	2.05	0.11	0.05	0.00	99.46	0.913
on126-2_2-1	6	50	fRX	53.43	0.03	4.51	0.83	5.80	32.70	0.11	1.68	0.10	0.00	0.00	99.19	0.909
on126-2_2-2	6	51	fRX	53.96	0.03	4.18	0.77	5.73	32.82	0.15	1.66	0.11	0.06	0.01	99.49	0.911
Ave-P-c			**4**	**54.04**	**0.04**	**4.10**	**0.73**	**5.63**	**32.69**	**0.12**	**1.94**	**0.10**	**0.04**	**0.00**	**99.41**	**0.912**
sd				*0.19*	*0.02*	*0.13*	*0.06*	*0.09*	*0.16*	*0.01*	*0.20*	*0.01*	*0.02*	*0.00*	*0.16*	*0.00*
rel. sd				0.00	0.44	0.03	0.09	0.02	0.00	0.11	0.10	0.09	0.36	#DIV/0!	0.00	0.00
Ave-fRX			**2**	**53.70**	**0.03**	**4.35**	**0.80**	**5.77**	**32.76**	**0.13**	**1.67**	**0.11**	**0.03**	**0.01**	**99.34**	**0.91**
ANTP126-4																
o126-4_2c1	5	11	P-c	54.37	0.05	4.16	0.96	5.26	30.80	0.12	3.78	0.10	0.04	0.00	99.63	0.913
o126-4_2c2	5	12	P-c	54.65	0.05	3.98	0.88	5.58	32.76	0.15	1.65	0.10	0.00	0.01	99.82	0.913
o126-4_2r1	5	9	P-r	54.74	0.03	3.59	0.81	5.73	33.00	0.16	1.77	0.09	0.01	0.00	99.93	0.911
o126-4_2r2	5	10	P-r	54.94	0.01	3.57	0.81	5.44	32.41	0.18	2.08	0.09	0.07	0.00	99.60	0.914
o126-4_2-1	5	5	fRX	54.81	0.02	3.77	0.76	5.72	33.13	0.16	1.73	0.10	0.02	0.00	100.22	0.912
o126-4_2-2	5	6	fRX	55.30	0.01	3.36	0.68	5.68	33.25	0.14	1.65	0.10	0.03	0.00	100.20	0.913
Ave-P-c			**2**	**54.51**	**0.05**	**4.07**	**0.92**	**5.42**	**31.78**	**0.13**	**2.72**	**0.10**	**0.02**	**0.01**	**99.72**	**0.91**
Ave-P-r			**2**	**54.84**	**0.02**	**3.58**	**0.81**	**5.59**	**32.71**	**0.17**	**1.93**	**0.09**	**0.04**	**0.00**	**99.77**	**0.91**
Ave-fRX			**2**	**55.06**	**0.01**	**3.57**	**0.72**	**5.70**	**33.19**	**0.15**	**1.69**	**0.10**	**0.03**	**0.00**	**100.21**	**0.91**
ANTP126-5																
o126-5_1-1	5	13	P-c	54.26	0.02	4.73	0.91	5.66	32.71	0.12	1.49	0.10	0.04	0.00	100.04	0.912
o126-5_1-2	5	14	P-c	54.29	0.00	4.66	0.92	5.67	32.47	0.12	1.62	0.12	0.00	0.00	99.87	0.911
Ave-P-c			**2**	**54.28**	**0.01**	**4.70**	**0.91**	**5.67**	**32.59**	**0.12**	**1.56**	**0.11**	**0.02**	**0.00**	**99.96**	**0.91**
o126-5_3-1	5	23	fRX	54.98	0.02	3.83	0.63	5.51	32.79	0.12	1.73	0.08	0.05	0.01	99.75	0.914

Table D3: Opx analyses

Sample	file	An#	Text.	SiO2	TiO2	Al2O3	Cr2O3	FeO	MgO	MnO	CaO	NiO	Na2O	K2O	Total	Mg#
ANTP125-D5																
o126-d5a_5-1	10	61	P-c	53.94	0.02	**4.70**	**0.85**	5.70	32.11	0.14	2.29	0.09	0.03	0.01	99.89	0.909
o126-d5a_5-2	10	62	P-c	53.89	0.04	**4.56**	**0.75**	5.79	32.53	0.15	1.82	0.10	0.03	0.01	99.66	0.909
o126-d5a_5-3	10	63	P-c	54.10	0.02	**4.42**	**0.74**	5.69	32.67	0.19	1.77	0.09	0.00	0.01	99.70	0.911
o126-d5a_5-4	10	64	P-c	53.93	0.02	**4.61**	**0.78**	5.67	32.77	0.12	1.87	0.11	0.00	0.00	99.88	0.912
o126-d5a_3-1	10	58	fRX	54.03	0.04	**4.50**	**0.74**	5.79	32.60	0.13	1.64	0.09	0.03	0.00	99.59	0.909
o126-d5a_3-2	10	59	fRX	54.24	0.05	**4.09**	**0.73**	5.87	33.01	0.16	1.69	0.09	0.04	0.00	99.96	0.909
o126-d5a_5-5	10	65	fRX	54.27	0.06	**4.40**	**0.73**	5.86	32.94	0.13	1.64	0.10	0.00	0.01	100.13	0.909
o126-d5a_5-6	10	66	fRX	54.59	0.03	**4.13**	**0.68**	5.76	33.13	0.14	1.69	0.08	0.00	0.00	100.24	0.911
Ave-P-c			**4**	**53.97**	**0.03**	**4.57**	**0.78**	**5.71**	**32.52**	**0.15**	**1.94**	**0.10**	**0.01**	**0.01**	**99.78**	**0.910**
sd				*0.08*	*0.01*	*0.10*	*0.04*	*0.05*	*0.25*	*0.02*	*0.21*	*0.01*	*0.01*	*0.01*	*0.10*	*0.00*
rel. sd				0.00	0.27	0.02	0.06	0.01	0.01	0.15	0.11	0.06	1.00	0.62	0.00	0.00
Ave-fRX			**4**	**54.28**	**0.04**	**4.28**	**0.72**	**5.82**	**32.92**	**0.14**	**1.67**	**0.09**	**0.02**	**0.00**	**99.98**	**0.910**
sd				*0.20*	*0.01*	*0.17*	*0.02*	*0.05*	*0.20*	*0.01*	*0.02*	*0.01*	*0.02*	*0.00*	*0.24*	*0.00*
rel. sd				0.00	0.22	0.04	0.03	0.01	0.01	0.08	0.02	0.07	1.01	1.73	0.00	0.00
ANTP 84-11																
o89-11_2-2	24	26	P	54.67	0.02	3.24	0.70	6.11	33.98	0.13	1.76	0.07	0.00	0.02	100.69	0.908
o89-11_3-2	24	30	P	54.57	0.00	3.34	0.78	6.23	33.95	0.14	1.44	0.10	0.00	0.00	100.55	0.907
o89-11_3-1	24	29	P	54.50	0.03	3.34	0.78	6.12	33.58	0.17	1.79	0.10	0.00	0.00	100.41	0.907
Ave-P			**3**	**54.58**	**0.01**	**3.31**	**0.75**	**6.15**	**33.84**	**0.15**	**1.66**	**0.09**	**0.00**	**0.01**	**100.55**	**0.907**
ANTP 87-5																
o87-5a_3-2	16	13	P	54.99	0	3.51	0.72	5.73	33.38	0.123	1.93	0.098	0.012	0.00	100.493	0.912
o87-5a_4-1	16	17	P	54.92	0.013	3.56	0.788	5.76	33.37	0.132	1.94	0.086	0	0.00	100.569	0.912
Ave-P			**2**	**54.96**	**0.01**	**3.54**	**0.75**	**5.75**	**33.38**	**0.13**	**1.94**	**0.09**	**0.01**	**0.00**	**100.53**	**0.912**
ANTP 87-7																
o87-7a_1-1	24	7	P	54.94	0.05	2.94	0.92	5.51	33.66	0.15	2.26	0.09	0.05	0.02	100.59	0.916
o87-7a_1-2	24	8	P	55.08	0.04	2.84	0.91	5.43	33.36	0.11	2.75	0.08	0.14	0.00	100.74	0.916
o87-7a_2-1	24	9	P	55.34	0.05	2.82	0.91	5.58	34.28	0.13	1.71	0.10	0.06	0.00	100.98	0.916
o87-7a_2-2	24	10	P	55.15	0.04	2.95	0.91	5.65	34.08	0.11	1.78	0.10	0.07	0.00	100.84	0.915
o87-7b_1-1	24	1	fRX	55.66	0.02	2.62	0.84	5.59	34.54	0.14	1.59	0.08	0.05	0.00	101.12	0.917
o87-7b_1-2	24	2	fRX	55.60	0.04	2.65	0.87	5.49	34.18	0.13	1.77	0.13	0.09	0.02	100.96	0.917
Ave-P			**4**	**55.13**	**0.05**	**2.89**	**0.91**	**5.54**	**33.85**	**0.13**	**2.13**	**0.09**	**0.08**	**0.01**	**100.79**	**0.916**
sd				*0.29*	*0.01*	*0.14*	*0.03*	*0.08*	*0.43*	*0.02*	*0.44*	*0.02*	*0.03*	*0.01*	*0.19*	*0.00*
rel. sd				0.01	0.29	0.05	0.04	0.01	0.01	0.12	0.21	0.22	0.43	1.82	0.00	0.00
Ave-fRX			**2**	**55.63**	**0.03**	**2.64**	**0.85**	**5.54**	**34.36**	**0.13**	**1.68**	**0.11**	**0.07**	**0.01**	**101.04**	**0.917**
ANTP 89-1																
o89-1_2-1	19	11	fRX	54.85	0.039	3.7	0.768	5.56	33.82	0.121	1.69	0.105	0.053	0.02	100.726	0.916
o89-1_2-2	19	12	fRX	54.98	0.059	3.59	0.745	5.52	33.44	0.116	2.22	0.105	0.055	0.00	100.83	0.915
Ave-fRX			**2**	**54.92**	**0.05**	**3.65**	**0.76**	**5.54**	**33.63**	**0.12**	**1.96**	**0.11**	**0.05**	**0.01**	**100.78**	**0.915**
ANTP 89-1																
o89-1_4-1	19	18	P	53.81	0.06	4.48	1.057	5.21	31.39	0.108	3.59	0.079	0.06	0.02	99.865	0.915
ANTP 89-2																
o89-2_1-1	17	20	fRX	54.97	0.058	3.63	0.777	5.77	33.97	0.149	1.46	0.075	0.01	0.00	100.868	0.913
o89-2_3-1	28	9	P	54.55	0.03	4.17	0.83	5.94	34.02	0.12	1.51	0.11	0.00	0.00	101.28	0.911
o89-2_3-2	28	10	P	54.74	0.04	4.10	0.83	5.90	33.93	0.15	1.29	0.10	0.02	0.01	101.11	0.911
o89-2_3-3	28	11	P	54.66	0.04	4.13	0.81	5.84	34.04	0.18	1.35	0.10	0.04	0.00	101.19	0.912
o89-2_6-1	28	23	P	54.01	0.05	4.41	1.05	5.18	31.41	0.13	4.86	0.09	0.10	0.01	101.31	0.915
o89-2_6-2	28	24	P	53.64	0.04	5.26	1.07	5.72	32.69	0.12	2.39	0.12	0.04	0.01	101.09	0.911
o89-2_6-3	28	25	P	54.46	0.05	4.59	1.04	5.95	34.11	0.15	0.99	0.11	0.03	0.00	101.47	0.911
o89-2_6-4	28	26	P	54.01	0.06	4.16	0.99	5.25	31.42	0.14	4.99	0.09	0.09	0.01	101.22	0.914
o89-2_6-5	28	27	P	54.64	0.02	4.16	0.95	5.72	33.41	0.11	2.19	0.11	0.07	0.01	101.39	0.912
o89-2_6-6	28	28	P	54.62	0.07	4.23	0.97	5.63	33.30	0.14	2.30	0.08	0.03	0.00	101.38	0.913
Ave-P			**9**	**54.37**	**0.04**	**4.36**	**0.95**	**5.68**	**33.15**	**0.14**	**2.43**	**0.10**	**0.05**	**0.01**	**101.27**	**0.912**
ANTP 89-5																
o89-5_1-1	21	83	P	53.65	0.045	5.09	0.857	6.27	32.65	0.155	1.75	0.081	0.033	0.01	100.588	0.903
o89-5_1-3	21	85	P	53.51	0.021	5.14	0.882	6.45	32.87	0.124	1.093	0.114	0.036	0.00	100.239	0.901
o89-5_1-4	21	86	P	53.69	0.036	5.34	0.862	6.3	32.35	0.11	1.58	0.103	0.041	0.01	100.424	0.901
o89-5_3-3	21	113	fRX	53.91	0.052	4.91	0.793	6.87	33.04	0.143	0.88	0.094	0.023	0.00	100.715	0.896
o89-5_3-4	21	114	fRX	54.18	0.023	4.98	0.808	6.76	33.11	0.136	0.857	0.094	0	0.00	100.947	0.897
o89-8_3-1	26	13	fRX	54.08	0.02	4.91	0.84	5.95	33.17	0.13	1.75	0.10	0.00	0.01	100.97	0.909
Ave-P			**3**	**53.62**	**0.03**	**5.19**	**0.87**	**6.34**	**32.62**	**0.13**	**1.47**	**0.10**	**0.04**	**0.01**	**100.42**	**0.902**
Ave-fRX			**3**	**54.06**	**0.03**	**4.93**	**0.81**	**6.53**	**33.11**	**0.14**	**1.16**	**0.10**	**0.01**	**0.00**	**100.88**	**0.900**

Table D3: Opx analyses

Sample	file	An#	Text.	SiO2	TiO2	Al2O3	Cr2O3	FeO	MgO	MnO	CaO	NiO	Na2O	K2O	Total	Mg#
ANTP 89-8																
o89-8_3-2	26	14	P	53.90	0.03	4.81	0.85	5.87	33.08	0.15	1.97	0.12	0.02	0.01	100.80	0.909
o89-8_4-1	26	19	fRX	54.49	0.03	4.43	0.76	6.14	34.30	0.12	0.96	0.11	0.01	0.01	101.36	0.909
o89-8_4-2	26	20	fRX	54.53	0.03	4.48	0.80	6.24	34.16	0.16	0.97	0.12	0.01	0.00	101.49	0.907
Ave-fRX			**2**	**54.51**	**0.03**	**4.46**	**0.78**	**6.19**	**34.23**	**0.14**	**0.96**	**0.11**	**0.01**	**0.01**	**101.43**	**0.908**
ANTP 89-15																
o89-15a_2-1	25	8	P	54.29	0.03	4.06	0.94	5.82	34.04	0.13	1.50	0.10	0.02	0.01	100.93	0.912
o89-15a_2-2	25	9	P	54.62	0.04	4.11	0.97	5.93	34.33	0.13	0.97	0.09	0.00	0.01	101.20	0.912
o89-15b_4-1	27	21	P	54.25	0.05	4.37	1.01	5.80	34.02	0.14	1.23	0.11	0.03	0.02	101.03	0.913
o89-15b_1-1	27	13	fRX	55.39	0.04	3.30	0.70	5.81	34.74	0.16	1.26	0.07	0.02	0.00	101.50	0.914
o89-15b_1-2	27	14	fRX	55.10	0.05	3.45	0.68	5.64	34.42	0.10	1.65	0.08	0.02	0.00	101.18	0.916
Ave-P			**3**	**54.39**	**0.04**	**4.18**	**0.97**	**5.85**	**34.13**	**0.13**	**1.23**	**0.10**	**0.02**	**0.01**	**101.05**	**0.912**
Ave-fRX			**2**	**55.25**	**0.05**	**3.38**	**0.69**	**5.73**	**34.58**	**0.13**	**1.45**	**0.07**	**0.02**	**0.00**	**101.34**	**0.915**
ANTP 89-17																
o89-17_1-1	25	22	P	54.45	0.01	3.95	0.94	5.90	32.57	0.15	3.06	0.10	0.00	0.00	101.14	0.908
o89-17_1-2	25	23	P	54.32	0.01	3.90	0.91	6.11	33.11	0.12	1.60	0.09	0.01	0.01	100.19	0.906
o89-17_1-3	25	24	P	54.34	0.04	3.99	0.97	6.09	33.53	0.15	1.83	0.10	0.00	0.00	101.03	0.908
Ave-P			**3**	**54.37**	**0.02**	**3.95**	**0.94**	**6.03**	**33.07**	**0.14**	**2.16**	**0.10**	**0.00**	**0.00**	**100.79**	**0.907**
74GTV																
o31a_3-1	1	14	P-c	55.26	0.05	3.61	0.95	6.00	32.43	0.12	1.90		0.01	0.00	100.32	0.906
o31a_3-2	1	15	P-c	55.48	0.07	3.51	0.98	5.81	32.71	0.18	1.96		0.02	0.00	100.73	0.909
o31a_3-3	1	16	P-c	55.67	0.00	3.32	0.93	5.88	32.58	0.15	1.94		0.00	0.00	100.47	0.908
o31a_4-1	1	23	P-r	56.21	0.03	3.00	0.75	5.80	33.07	0.17	1.79		0.00	0.00	100.81	0.910
o31a_4-3	1	25	P-c	55.86	0.04	3.24	0.87	5.64	33.10	0.10	1.36		0.01	0.00	100.21	0.913
o31a_4-4	1	26	P-c	55.74	0.06	3.34	0.86	5.72	32.88	0.11	1.61		0.00	0.00	100.30	0.911
o31b_1-1	1	33	P-r	55.63	0.00	3.29	0.82	5.98	33.26	0.19	1.22		0.00	0.05	100.45	0.908
o31b_1-2	1	34	P-r	55.51	0.00	3.18	0.83	5.80	32.49	0.12	2.14		0.00	0.00	100.07	0.909
o31b_1-3	1	35	P-r	55.54	0.01	3.11	0.76	5.70	32.63	0.09	1.95		0.00	0.00	99.77	0.911
o31b_3-1	1	37	P-c	55.92	0.04	3.33	0.84	5.91	32.36	0.11	2.50		0.01	0.00	101.01	0.907
o31b_3-2	1	38	P-c	55.83	0.07	3.45	0.83	5.59	32.13	0.16	2.41		0.02	0.00	100.48	0.911
o31b_3-3	1	39	P-c	55.90	0.05	3.30	0.86	5.68	32.30	0.08	2.53		0.01	0.01	100.72	0.910
Ave-P			**12**	**55.71**	**0.03**	**3.31**	**0.86**	**5.79**	**32.66**	**0.13**	**1.94**		**0.01**	**0.01**	**100.44**	**0.910**

Table D4: Olivine analyses

Sample	Text.	SiO2	TiO2	Al2O3	Cr2O3	FeO	MgO	MnO	CaO	NiO	Total	Mg#
ANTP134-3												
ol134-3_2-1	P	39.96	0.00	0.00	0.02	8.62	50.52	0.12	0.02	0.38	99.64	0.913
ol134-3_2-2	P	40.06	0.00	0.00	0.02	8.52	50.86	0.13	0.02	0.39	100.03	0.914
ol134-3_3-1	P	40.00	0.01	0.00	0.00	8.48	50.78	0.13	0.01	0.39	99.80	0.914
ol134-3_4-1	P	40.44	0.00	0.01	0.03	8.66	50.69	0.16	0.03	0.39	100.42	0.913
ol134-3_4-2	P	40.29	0.01	0.00	0.00	8.54	50.63	0.12	0.03	0.38	100.03	0.914
in134-3_3-1	Incl	40.32	0.00	0.00	0.06	7.74	51.36	0.13	0.05	0.44	100.10	0.922
in134-3_3-2	Incl	40.30	0.00	0.00	0.08	7.73	51.64	0.09	0.04	0.44	100.32	0.923
ave-P	**5**	**40.15**	**0.00**	**0.00**	**0.01**	**8.56**	**50.70**	**0.13**	**0.02**	**0.39**	**99.98**	**0.913**
sd		*0.21*	*0.01*	*0.00*	*0.01*	*0.07*	*0.13*	*0.02*	*0.01*	*0.01*	*0.30*	*0.001*
rel. sd		0.01	1.40	2.24	0.96	0.01	0.00	0.13	0.33	0.02	0.00	0.001
ave-Incl	**2**	**40.31**	**0.00**	**0.00**	**0.07**	**7.74**	**51.50**	**0.11**	**0.04**	**0.44**	**100.21**	**0.922**
ANTP134-4												
ol134-4_1-1	P	40.33	0.02	0.00	0.01	8.50	51.12	0.13	0.00	0.39	100.50	0.915
ol134-4_1-2	P	40.31	0.00	0.00	0.00	8.50	51.15	0.13	0.02	0.41	100.52	0.915
ol134-4_2-1	P	40.26	0.00	0.02	0.00	8.54	51.02	0.09	0.04	0.37	100.34	0.914
ol134-4_5-2	P	40.28	0.01	0.00	0.02	8.34	50.55	0.14	0.03	0.37	99.74	0.915
ol134-4_3-1	P	40.88	0.02	0.00	0.03	8.57	51.24	0.12	0.03	0.38	101.26	0.914
ol134-4_3-2	P	40.79	0.00	0.01	0.02	8.69	51.28	0.13	0.02	0.38	101.32	0.913
ave-P	**6**	**40.48**	**0.01**	**0.01**	**0.01**	**8.52**	**51.06**	**0.12**	**0.02**	**0.38**	**100.62**	**0.914**
sd		*0.28*	*0.01*	*0.01*	*0.01*	*0.11*	*0.27*	*0.02*	*0.01*	*0.02*	*0.59*	*0.00*
rel. sd		0.01	1.13	1.59	0.91	0.01	0.01	0.16	0.61	0.04	0.01	0.00
ANTP134-5												
ol134-5_3-1	P	40.10	0.00	0.00	0.02	8.43	51.51	0.12	0.06	0.39	100.63	0.916
ol134-5_3-2	P	39.89	0.00	0.00	0.01	8.44	51.40	0.10	0.04	0.38	100.30	0.916
ave-P	**2**	**40.00**	**0.00**	**0.00**	**0.02**	**8.44**	**51.46**	**0.11**	**0.05**	**0.39**	**100.47**	**0.916**
ANTP134-8												
ol134-8_2-1	P	40.28	0.00	0.02	0.00	8.59	50.36	0.08	0.06	0.38	99.77	0.913
ol134-8_2-2	P	40.23	0.01	0.00	0.05	8.34	50.66	0.17	0.05	0.39	99.95	0.915
ave-P	**2**	**40.26**	**0.01**	**0.01**	**0.02**	**8.47**	**50.51**	**0.12**	**0.05**	**0.38**	**99.86**	**0.914**
Circe93-2												
ol93-2a_3-1	P	40.22	0.00	0.02	0.02	8.51	51.09	0.15	0.07	0.39	100.46	0.915
ol93-2a_3-2	P	40.22	0.00	0.01	0.02	8.66	51.09	0.10	0.06	0.37	100.53	0.913
ol93-2a_3-3	P	40.48	0.01	0.00	0.04	8.53	51.18	0.08	0.07	0.38	100.77	0.914
ol93-2a_6-1	P	40.28	0.00	0.00	0.00	8.76	51.13	0.09	0.03	0.36	100.65	0.912
ol93-2a_6-2	P	40.29	0.01	0.00	0.00	8.59	50.94	0.13	0.05	0.35	100.38	0.914
ol93-2a_6-3	P	40.14	0.04	0.00	0.02	8.64	51.14	0.13	0.02	0.37	100.52	0.913
ave-P	**6**	**40.27**	**0.01**	**0.00**	**0.02**	**8.62**	**51.10**	**0.11**	**0.05**	**0.37**	**100.55**	**0.914**
sd		*0.12*	*0.01*	*0.01*	*0.02*	*0.09*	*0.08*	*0.03*	*0.02*	*0.01*	*0.14*	*0.00*
rel. sd		0.00	1.49	1.61	0.97	0.01	0.00	0.24	0.40	0.03	0.00	0.001
Circe93-3												
ol93-3a_1-1	P	40.71	0.00	0.00	0.00	7.76	51.35	0.10	0.01	0.40	100.33	0.922
ol93-3a_1-2	P	40.74	0.03	0.00	0.00	7.68	51.57	0.12	0.02	0.41	100.57	0.923
c93-3a_3-1	P	40.40	0.03	0.00	0.00	7.97	51.35	0.11	0.01	0.39	100.26	0.920
c93-3a_3-2	P	40.61	0.05	0.00	0.00	7.81	51.02	0.13	0.02	0.40	100.03	0.921
ol93-3b_1-1	P	40.32	0.02	0.01	0.05	8.11	51.19	0.12	0.07	0.39	100.32	0.918
ol93-3b_1-2	P	40.37	0.00	0.02	0.01	8.15	51.26	0.12	0.08	0.37	100.38	0.918
c93-3b_3-1	P	40.48	0.00	0.00	0.02	7.67	51.56	0.08	0.02	0.41	100.24	0.923
c93-3b_4-1	P	40.49	0.01	0.01	0.00	8.04	51.17	0.14	0.02	0.38	100.28	0.919
c93-3b_4-2	P	40.46	0.01	0.00	0.02	8.26	51.04	0.12	0.03	0.38	100.31	0.917
c93-3b_5-1	P	40.42	0.00	0.00	0.01	8.01	51.28	0.13	0.02	0.38	100.27	0.919
ave-P	**10**	**40.50**	**0.01**	**0.00**	**0.01**	**7.95**	**51.28**	**0.12**	**0.03**	**0.39**	**100.30**	**0.920**
sd		*0.14*	*0.02*	*0.01*	*0.02*	*0.21*	*0.19*	*0.02*	*0.03*	*0.01*	*0.13*	*0.00*
rel. sd		0.00	1.10	1.68	1.49	0.03	0.00	0.15	0.83	0.03	0.00	0.002
Circe93-4												
ol93-4_1-1	P	40.09	0.00	0.00	0.00	8.72	50.54	0.11	0.06	0.38	99.92	0.912
ol93-4_1-2	P	40.01	0.01	0.00	0.00	8.65	50.74	0.14	0.05	0.38	99.99	0.913
ol93-4_1-3	P	40.17	0.00	0.00	0.00	8.62	50.99	0.15	0.07	0.38	100.40	0.913
ave-P	**3**	**40.09**	**0.00**	**0.00**	**0.00**	**8.66**	**50.76**	**0.13**	**0.06**	**0.38**	**100.10**	**0.913**
sd		*0.08*	*0.01*	*0.00*	*0.00*	*0.05*	*0.23*	*0.02*	*0.01*	*0.00*	*0.26*	*0.00*
rel. sd		0.00	1.73			0.01	0.00	0.16	0.24	0.01	0.00	0.001

Table D4: Olivine analyses

Sample	Text.	SiO2	TiO2	Al2O3	Cr2O3	FeO	MgO	MnO	CaO	NiO	Total	Mg#
Circe93-5												
ol93-5a_1-1	P	40.55	0.00	0.02	0.00	7.87	51.36	0.17	0.08	0.37	100.42	0.921
ol93-5a_1-2	P	40.49	0.00	0.00	0.01	7.80	51.50	0.07	0.08	0.38	100.35	0.922
ol93-5a_4-1	P	40.72	0.02	0.00	0.04	7.88	51.69	0.11	0.03	0.38	100.88	0.921
c93-5a_4-1	P	40.68	0.00	0.00	0.00	7.94	51.13	0.08	0.02	0.37	100.23	0.920
ave-P	**4**	**40.61**	**0.01**	**0.00**	**0.01**	**7.87**	**51.42**	**0.11**	**0.05**	**0.37**	**100.47**	**0.921**
sd		*0.11*	*0.01*	*0.01*	*0.02*	*0.06*	*0.24*	*0.05*	*0.03*	*0.01*	*0.29*	*0.00*
rel. sd		0.00	2.00	2.00	1.47	0.01	0.00	0.43	0.55	0.02	0.00	0.001
Circe93-7												
ol93-7_1-1	P	40.57	0.00	0.03	0.10	7.76	51.74	0.13	0.01	0.40	100.73	0.922
ol93-7_1-2	P	40.69	0.00	0.01	0.12	7.95	51.12	0.10	0.03	0.39	100.43	0.920
ol93-7_2-1	P	41.01	0.03	0.01	0.06	7.91	52.14	0.12	0.05	0.43	101.80	0.922
ol93-7_2-2	P	40.96	0.00	0.00	0.03	7.84	51.91	0.15	0.04	0.40	101.35	0.922
ave-P	**4**	**40.81**	**0.01**	**0.01**	**0.08**	**7.87**	**51.73**	**0.12**	**0.03**	**0.40**	**101.08**	**0.921**
sd		*0.21*	*0.01*	*0.01*	*0.04*	*0.08*	*0.44*	*0.02*	*0.02*	*0.02*	*0.62*	*0.00*
rel. sd		0.01	2.00	0.80	0.49	0.01	0.01	0.16	0.49	0.05	0.01	0.001
ANTP125-2												
ol125-2b_1	P	40.31	0.00	0.00	0.04	9.24	50.35	0.16	0.06	0.39	100.56	0.907
ol125-2b_5-1	Incl	40.06	0.01	0.02	0.04	9.00	50.10	0.10	0.03	0.42	99.78	0.908
ol125-2b_5-2	Incl	40.09	0.00	0.03	0.02	8.98	50.09	0.14	0.02	0.41	99.79	0.909
ol125-2b_5-3	Incl	39.96	0.00	0.03	0.03	8.93	50.37	0.11	0.04	0.42	99.90	0.910
ave-Incl	**3**	**40.04**	**0.00**	**0.02**	**0.03**	**8.97**	**50.19**	**0.12**	**0.03**	**0.41**	**99.82**	**0.909**
sd		*0.07*	*0.01*	*0.00*	*0.01*	*0.04*	*0.16*	*0.02*	*0.01*	*0.01*	*0.06*	*0.00*
rel. sd		0.00	1.73	0.19	0.41	0.00	0.00	0.15	0.26	0.02	0.00	0.001
ANTP126-2												
ol126-2_1-1	P	40.04	0.02	0.00	0.03	9.11	50.63	0.13	0.09	0.38	100.46	0.908
ol126-2_1-2	P	39.94	0.00	0.00	0.02	9.04	50.12	0.11	0.09	0.38	99.71	0.908
ol126-2_1-3	P	39.60	0.01	0.02	0.03	8.97	50.66	0.14	0.12	0.37	99.94	0.910
in126-2_2-1	Incl	39.95	0.02	0.04	0.28	8.07	51.26	0.13	0.07	0.43	100.24	0.919
in126-2_2-2	Incl	40.04	0.00	0.07	0.24	8.16	51.18	0.15	0.07	0.41	100.35	0.918
ave-P	**3**	**39.86**	**0.01**	**0.01**	**0.03**	**9.04**	**50.47**	**0.13**	**0.10**	**0.38**	**100.04**	**0.909**
sd		*0.23*	*0.01*	*0.01*	*0.01*	*0.07*	*0.30*	*0.02*	*0.02*	*0.00*	*0.39*	*0.00*
rel. sd		0.01	0.95	1.73	0.24	0.01	0.01	0.14	0.18	0.01	0.00	0.001
ave-Incl	**2**	**40.00**	**0.01**	**0.06**	**0.26**	**8.12**	**51.22**	**0.14**	**0.07**	**0.42**	**100.30**	**0.918**
ANTP126-4	P	40.53	0.00	0.02	0.06	8.74	50.48	0.14	0.07	0.38	100.44	0.911
ANTP126-5												
ol126-5_1-1	P	40.21	0.00	0.01	0.02	9.07	50.43	0.14	0.06	0.39	100.33	0.908
ol126-5_1-2	P	40.01	0.00	0.01	0.03	9.02	50.23	0.13	0.04	0.39	99.86	0.908
ol126-5_3-1	P	40.39	0.00	0.02	0.00	8.94	50.53	0.14	0.06	0.37	100.46	0.910
ave-P	**3**	**40.20**	**0.00**	**0.01**	**0.02**	**9.01**	**50.40**	**0.14**	**0.05**	**0.38**	**100.22**	**0.909**
sd		*0.19*	*0.00*	*0.00*	*0.01*	*0.07*	*0.15*	*0.01*	*0.01*	*0.01*	*0.32*	*0.00*
rel. sd		0.00		0.29	0.94	0.01	0.00	0.04	0.16	0.03	0.00	0.001
ANTP126-D5												
ol126-d5a_1-1	P	40.32	0.00	0.03	0.00	9.09	50.48	0.13	0.10	0.38	100.54	0.908
ol126-d5a_1-2	P	40.28	0.03	0.02	0.00	8.85	50.18	0.11	0.10	0.37	99.97	0.910
ol126-d5a_7-1	Incl	40.17	0.00	0.02	0.02	8.71	50.61	0.16	0.12	0.39	100.19	0.912
ol126-d5a_7-2	Incl	40.42	0.00	0.05	0.03	8.77	50.39	0.14	0.13	0.39	100.33	0.911
ol126-d5a_7-3	Incl	40.30	0.01	0.02	0.02	8.62	50.63	0.15	0.11	0.39	100.26	0.913
ave-P	**2**	**40.30**	**0.02**	**0.03**	**0.00**	**8.97**	**50.33**	**0.12**	**0.10**	**0.38**	**100.26**	**0.909**
ave-Incl	**3**	**40.30**	**0.00**	**0.03**	**0.02**	**8.70**	**50.54**	**0.15**	**0.12**	**0.39**	**100.26**	**0.912**
sd		*0.13*	*0.01*	*0.02*	*0.01*	*0.08*	*0.13*	*0.01*	*0.01*	*0.00*	*0.07*	*0.00*
rel. sd		0.00	1.73	0.60	0.42	0.01	0.00	0.07	0.11	0.01	0.00	0.001
ANTP84-11												
ol84-11_2-1	P	39.60	0.00	0.00	0.00	9.50	52.24	0.15	0.03	0.38	101.94	0.907
olin84-11_3-1	Incl	39.41	0.00	0.03	0.02	9.49	52.12	0.14	0.02	0.45	101.67	0.907

Appendix E: Ion microprobe data

Table E1: MPI trace element analyses

Sample	Ti	V	Cr	Sr	Y	Zr	*Ba*	La	Ce	Nd	Sm	Eu	Gd	Dy	Er	Yb
ANTP134-3_1alt	681	143	7746	*1.10*	5.69	0.57	*0.25*	0.001	0.017	0.21	0.27	0.14	0.57	1.07	0.79	0.76
ANTP134-3_2	730	152	7311	0.63	6.63	0.68	0.06	0.002	0.012	0.27	0.41	0.14	0.74	1.36	0.89	0.96
ANTP134-3	**705**	**148**	**7528**	***0.63***	**6.16**	**0.62**	***0.15***	**0.001**	**0.014**	**0.24**	**0.34**	**0.14**	**0.66**	**1.22**	**0.84**	**0.86**
ANTP134-4-2cm1	608	127	6917	0.76	5.95	0.58	0.03	0.002	0.032	0.26	0.22	0.12	0.71	1.07	0.76	0.78
ANTP134-4-2cm2	600	140	7815	0.93	5.48	0.53	0.07	0.004	0.032	0.28	0.23	0.13	0.60	1.04	0.66	0.83
ANTP134-4-2cm3	590	139	8199	0.94	5.75	0.51	0.06	0.001	0.044	0.23	0.35	0.14	0.72	1.15	0.77	0.88
ANTP134-4	**600**	**135**	**7644**	**0.88**	**5.73**	**0.54**	**0.06**	**0.002**	**0.04**	**0.26**	**0.27**	**0.13**	**0.68**	**1.09**	**0.73**	**0.83**
ANTP134-8	**544**	**128**	**7819**	**0.65**	**4.73**	**0.47**	**0.03**	**0.002**	**0.024**	**0.19**	**0.19**	**0.08**	**0.65**	**0.93**	**0.54**	**0.58**
c93-2_1	873	139	6267	0.87	5.22	0.38	0.06	0.014	0.028	0.06	0.14	0.07	0.45	0.83	0.60	0.61
c93-2_2alt	889	131	5839	*1.51*	5.67	0.42	*0.49*	*0.047*	*0.069*	0.07	0.11	0.05	0.40	0.66	0.68	0.82
CIRCE 93-2	**881**	**135**	**6053**	***0.87***	**5.45**	**0.40**	***0.06***	***0.014***	***0.028***	**0.06**	**0.12**	**0.06**	**0.42**	**0.75**	**0.64**	**0.72**
c93-4-1	506	159	7380	0.44	5.36	0.22	0.02	0.003	0.015	0.10	0.14	0.05	0.39	0.96	0.69	0.72
c93-4-2	500	165	7338	0.44	4.67	0.16	0.02		0.011	0.11	0.08	0.05	0.36	0.82	0.56	0.75
CIRCE 93-4	**503**	**162**	**7359**	**0.44**	**5.01**	**0.19**	**0.02**	**0.003**	**0.01**	**0.11**	**0.11**	**0.05**	**0.37**	**0.89**	**0.63**	**0.74**
c93-7_1	510	160	8335	3.65	3.95	3.20	0.34	0.017	0.103	0.51	0.50	0.22	0.84	0.83	0.44	0.52
c93-7_2	587	164	7351	2.84	4.41	3.73	0.16	0.013	0.086	0.48	0.42	0.21	0.84	0.85	0.44	0.53
CIRCE 93-7	**549**	**162**	**7843**	**3.24**	**4.18**	**3.47**	**0.25**	**0.02**	**0.09**	**0.50**	**0.46**	**0.21**	**0.84**	**0.84**	**0.44**	**0.53**
ANTP126-2_1	367	163	6072	0.48	4.49	0.24	0.05	0.008	0.057	0.03	0.07	0.04	0.25	0.74	0.63	0.66
ANTP126-2_2	346	161	6375	0.61	4.47	0.19	0.08	0.010	0.040	0.04	0.08	0.04	0.26	0.72	0.59	0.66
ANTP126-2	**357**	**162**	**6224**	**0.54**	**4.48**	**0.21**	**0.06**	**0.01**	**0.05**	**0.04**	**0.07**	**0.04**	**0.25**	**0.73**	**0.61**	**0.66**
ANTP126-5_1	384	170	6777	0.49	4.76	0.17	0.02	0.012	0.050	0.06	0.09	0.04	0.32	0.73	0.67	0.74
ANTP126-5_2	325	155	7027	0.44	4.45	0.17	0.02	0.007	0.040	0.06	*0.05*	0.04	0.35	0.75	0.57	0.76
ANTP126-5	**354**	**163**	**6902**	**0.47**	**4.60**	**0.17**	**0.02**	**0.01**	**0.05**	**0.06**	***0.09***	**0.04**	**0.34**	**0.74**	**0.62**	**0.75**
ANTP126-d5_2	500	167	5589	0.60	5.34	0.19	0.02	0.005	0.024	0.06	0.13	0.06	0.41	0.92	0.79	0.84
ANTP126-d5_1	442	155	5123	0.57	5.07	0.16	0.04	0.006	0.016	0.04	0.14	0.06	0.36	0.95	0.64	0.83
ANTP126-D5	**471**	**161**	**5356**	**0.58**	**5.20**	**0.17**	**0.03**	**0.005**	**0.02**	**0.05**	**0.13**	**0.06**	**0.39**	**0.94**	**0.71**	**0.84**
ANTP84-11_1	108	136	7208	0.15	1.84	0.07	0.04	0.0004	0.002	0.005	0.01	0.002	0.05	0.25	0.28	0.36
ANTP84-11_2	129	147	6945	0.23	2.24	0.07	0.08	0.0004	0.003		0.01	0.004	0.07	0.34	0.30	0.45
ANTP84-11	**118**	**141**	**7076**	**0.19**	**2.04**	**0.07**	**0.06**	**0.0004**	**0.002**	**0.005**	**0.01**	**0.003**	**0.06**	**0.29**	**0.29**	**0.40**
ANTP87-5_4-1	238	107	6321	0.25	2.77	0.08	0.07	0.004	0.002		0.03	0.02	0.12	0.42	0.43	0.50
ANTP87-5_4-2	235	107	6680	0.24	2.83	0.08	0.04	0.001	0.002	0.00	0.03	0.02	0.14	0.42	0.49	0.49
ANTP87-5	**236**	**107**	**6500**	**0.25**	**2.80**	**0.08**	**0.05**	**0.002**	**0.00**	**0.002**	**0.03**	**0.02**	**0.13**	**0.42**	**0.46**	**0.49**
ANTP87-9_5	309	119	7440	0.39	3.65	0.13	0.08		0.006	0.013	0.05	0.04	0.20	0.57	0.42	0.56
ANTP87-9_4	322	120	6629	0.56	3.96	0.10	0.16	0.005	0.009	0.030	0.03	0.03	0.23	0.55	0.52	0.61
ANTP87-9	**315**	**119**	**7035**	**0.48**	**3.81**	**0.11**	**0.12**	**0.005**	**0.01**	**0.02**	**0.04**	**0.04**	**0.22**	**0.56**	**0.47**	**0.59**

Ba concentrations are used only to monitor alteration
Values in italics are not used to calculate avg

Table E1: MPI trace element analyses

Sample	Ti	V	Cr	Sr	Y	Zr	*Ba*	La	Ce	Nd	Sm	Eu	Gd	Dy	Er	Yb
ANTP89-1_2	821	149	7693	0.73	6.79	0.73	0.06	0.003	0.013	0.23	0.29	0.13	0.71	1.35	0.87	0.93
ANTP89-1_1	847	144	7573	0.71	6.76	0.83	0.05	0.001	0.012	0.20	0.32	0.13	0.81	1.31	0.81	0.98
ANTP89-1	**834**	**146**	**7633**	**0.72**	**6.78**	**0.78**	**0.05**	**0.002**	**0.01**	**0.21**	**0.30**	**0.13**	**0.76**	**1.33**	**0.84**	**0.95**
ANTP89-2-3	632	140	7168	0.43	6.03	0.28	0.08	0.002	0.003	0.04	0.14	0.10	0.51	1.05	0.78	0.80
ANTP89-2-4	768	165	7629	0.37	7.38	0.28	0.05	0.002	0.008	0.08	0.18	0.10	0.59	1.39	0.90	1.01
ANTP89-2	**700**	**153**	**7398**	**0.40**	**6.70**	**0.28**	**0.07**	**0.002**	**0.01**	**0.06**	**0.16**	**0.10**	**0.55**	**1.22**	**0.84**	**0.91**
ANTP89-5-1	721	156	6448	0.26	7.39	0.22	0.05	0.000	0.006	0.15	0.23	0.14	0.77	1.40	0.96	1.08
ANTP89-5-2	715	156	6376	0.27	7.95	0.23	0.04	0.001	0.007	0.11	0.25	0.13	0.67	1.39	0.94	1.08
ANTP89-5-4	730	169	5478	0.29	7.14	0.18	0.07	0.002	0.003	0.12	0.20	0.12	0.75	1.35	0.93	1.08
ANTP89-5	**722**	**160**	**6101**	**0.27**	**7.49**	**0.21**	**0.05**	**0.001**	**0.005**	**0.13**	**0.23**	**0.13**	**0.73**	**1.38**	**0.95**	**1.08**
ANTP89-8_1	759	178	6207	0.29	7.15	0.27	0.06	0.003	0.008	0.15	0.24	0.13	0.80	1.38	0.96	0.98
ANTP89-8_3	733	178	7081	0.29	7.13	0.25	0.06	0.002	0.004	0.09	0.19	0.12	0.70	1.28	0.99	1.00
ANTP89-8	**746**	**178**	**6644**	**0.29**	**7.14**	**0.26**	**0.06**	**0.00**	**0.01**	**0.12**	**0.21**	**0.13**	**0.75**	**1.33**	**0.97**	**0.99**
ANTP89-15b_2-1	911	159	8150	0.63	6.54	0.86	0.05		0.008	0.19	0.25	0.12	0.64	1.13	0.76	0.80
ANTP89-15b_2-2	840	148	7756	0.78	6.73	0.84	0.12	0.0007	0.011	0.17	0.24	0.12	0.66	1.17	0.82	0.90
ANTP89-15b-1	984	171	8682	0.59	7.21	0.96	0.07	0.0018	0.006	0.17	0.15	0.13	0.79	1.43	1.08	0.96
ANTP89-15b-2	1150	174	8625	0.51	8.17	1.14	0.08	0.0019	0.008	0.15	0.22	0.14	0.74	1.29	1.04	1.00
ANTP89-15	**971**	**163**	**8303**	**0.63**	**7.16**	**0.95**	**0.08**	**0.001**	**0.01**	**0.17**	**0.21**	**0.13**	**0.71**	**1.26**	**0.93**	**0.92**
ANTP89-17-1	403	170	7851	0.29	4.36	0.11	0.04		0.001	0.011	0.05	0.03	0.25	0.58	0.60	0.72
ANTP89-17-2	355	160	7608	0.37	3.93	0.11		0.012	0.011	0.008	0.06	0.04	0.24	0.59	0.58	0.69
ANTP89-17-3	402	189	7739	0.34	4.19	0.15	0.05	0.017	0.022	0.017	0.07	0.04	0.23	0.68	0.51	0.73
ANTP89-17-4	414	190	8242	0.54	4.27	0.15	*0.33*	0.012	0.016	0.011	0.06	0.04	0.25	0.70	0.59	0.74
ANTP89-17	**393**	**177**	**7860**	**0.39**	**4.19**	**0.13**	**0.04**	**0.01**	**0.01**	**0.012**	**0.06**	**0.04**	**0.24**	**0.64**	**0.57**	**0.72**
31GTV-1	505	178	7966	0.38	3.63	0.18	0.06		0.006	0.05	0.06	0.04	0.29	0.66	0.51	0.65
31GTV-2	408	176	7431	0.39	3.18	0.15	0.11	0.002	0.003	0.02	0.05	0.02	0.17	0.55	0.35	0.51
31GTV	**457**	**177**	**7699**	**0.39**	**3.41**	**0.16**	**0.08**	**0.002**	**0.004**	**0.04**	**0.06**	**0.03**	**0.23**	**0.61**	**0.43**	**0.58**
60GTV	**478**	**166**	**6913**	**0.42**	**3.53**	**0.13**	**0.18**	**0.005**	**0.017**	**0.03**	**0.09**	**0.04**	**0.27**	**0.60**	**0.43**	**0.58**
74-31-3	402	168	7886	0.35	3.39	0.13	0.04	0.002	0.005	0.02	0.04	0.03	0.21	0.61	0.46	0.55
74GTV1	408	156	7356	0.22	2.73	0.10	0.01	0.000	0.002	0.02	0.06	0.03	0.22	0.32	0.33	0.43
74GTV2	449	168	7616	0.31	3.40	0.12	0.01		0.001	0.01	0.02	0.01	0.11	0.22	0.20	0.22
74GTV	**420**	**164**	**7620**	**0.29**	**3.17**	**0.12**	**0.02**	**0.0013**	**0.003**	**0.02**	**0.04**	**0.02**	**0.18**	**0.39**	**0.33**	**0.33**

Ba concentrations are used only to monitor alteration
Values in italics are not used to calculate avg

Table E2: WHOI trace element analyses

Sample	Ti	Sr	Y	Zr	Ce	Nd	Sm	Eu	Dy	Er	Yb
ANTP126-5-1					0.039	0.097	0.11	0.06	0.59	0.45	0.54
ANTP126-5-2					0.044	0.081	0.06	0.05	0.62	0.50	0.61
ANTP126-5					**0.041**	**0.089**	**0.09**	**0.05**	**0.61**	**0.47**	**0.57**
ANTP126-D5-1					0.020	0.093	0.16	0.08	0.80	0.54	0.61
ANTP126-D5-2					0.020	0.075	0.09	0.08	0.71	0.53	0.63
ANTP126-D5					**0.020**	**0.084**	**0.12**	**0.08**	**0.76**	**0.54**	**0.62**
ANTP134-3-2	704	1.1	6.2	1.1	0.012	0.248	0.25	0.11	0.89	0.63	0.59
ANTP134-3-3	633	1.6	5.7	0.9	0.019	0.246	0.24	0.13	0.83	0.60	0.54
ANTP134-3	**668**	**1.3**	**6.0**	**1.0**	**0.016**	**0.247**	**0.25**	**0.12**	**0.86**	**0.62**	**0.56**
ANTP134-4-1	633	1.2	5.9	1.0	0.037	0.221	0.24	0.11	0.79	0.52	0.47
ANTP134-4-2	657	1.2	5.6	1.2	0.041	0.404	0.36	0.13	0.74	0.64	0.59
ANTP134-4-3	594	0.8	5.9	0.9	0.026	0.317	0.29	0.12	0.80	0.48	0.64
ANTP134-4	**628**	**1.1**	**5.8**	**1.0**	**0.035**	**0.314**	**0.30**	**0.12**	**0.78**	**0.55**	**0.57**
ANTP134-7-1	853	0.7	6.0	1.3	0.038	0.271	0.28	0.11	0.84	0.61	0.54
ANTP134-7-2	849	1.3	6.9	1.8	0.023	0.297	0.25	0.12	0.88	0.69	0.61
ANTP134-7-3	913	1.8	6.9	1.9	0.013	0.273	0.22	0.12	0.86	0.51	0.54
ANTP134-7-4	816	1.4	6.1	1.6	0.025	0.296	0.25	0.11	0.81	0.57	0.55
ANTP134-7	**858**	**1.3**	**6.5**	**1.6**	**0.025**	**0.284**	**0.25**	**0.12**	**0.85**	**0.59**	**0.56**
ANTP134-8-1	611	0.9	5.9	0.9	0.038	0.246	0.20	0.15	0.74	0.47	0.50
ANTP134-8-2	589	1.0	6.0	1.2	0.028	0.329	0.27	0.13	0.92	0.60	0.58
ANTP134-8-3	723	1.0	6.5	1.4	0.033	0.291	0.30	0.14	0.96	0.61	0.77
ANTP134-8	**641**	**1.0**	**6.1**	**1.2**	**0.033**	**0.288**	**0.26**	**0.14**	**0.87**	**0.56**	**0.62**
CIRCE93-2-1	899	1.4	5.1	0.7	0.027	0.088	0.17	0.06	0.58	0.47	0.45
CIRCE93-2-2	752	1.8	4.6	0.8		0.152	0.11	0.07	0.71	0.54	0.53
CIRCE93-2	**825**	**1.6**	**4.8**	**0.8**	**0.027**	**0.120**	**0.14**	**0.07**	**0.64**	**0.51**	**0.49**
CIRCE93-4-1	436	0.9	4.4	0.4	0.018	0.130	0.13	0.07	0.83	0.63	0.56
CIRCE93-4-2	467	1.5	5.8	0.7	0.014	0.127	0.15	0.05	0.86	0.57	0.59
CIRCE93-4	**451**	**1.2**	**5.1**	**0.5**	**0.016**	**0.129**	**0.14**	**0.06**	**0.85**	**0.60**	**0.58**